DOT/FAA/TC-19/42

Federal Aviation Administration
William J. Hughes Technical Center
Aviation Research Division
Atlantic City International Airport
New Jersey 08405

Development of a Generalized Yield Surface for Isotropic, Pressure-Insensitive Metal Plasticity With Differing Tension, Compression, and Shear Yield Strengths

March 2020

Final Report

U.S. Department of Transportation
Federal Aviation Administration

NOTICE

Technical Report Documentation Page

1. Report No.	2. Government Accession No.	3. Recipient's Catalog No.
DOT/FAA/TC-19/42		

4. Title and Subtitle	5. Report Date
DEVELOPMENT OF A GENERALIZED YIELD SURFACE FOR ISOTROPIC, PRESSURE-INSENSITIVE METAL PLASTICITY WITH DIFFERING TENSION, COMPRESSION, AND SHEAR YIELD STRENGTHS	March 2020
	6. Performing Organization Code

7. Author(s)	8. Performing Organization Report No.
Kelly Carney[1], Paul Du Bois[1], Kivanc Sengoz[2], Leyu Wang[1], and Cing-Dao Kan[1]	

9. Performing Organization Name and Address	10. Work Unit No. (TRAIS)
[1]George Mason University Center for Collision Safety and Analysis 4087 University Drive, Fairfax, VA 22030 USA [2]The George Washington University FHWA/NHTSA National Crash Analysis Center 20101 Academic Way Ashburn, VA 20147	11. Contract or Grant No. 13-G-020

12. Sponsoring Agency Name and Address	13. Type of Report and Period Covered
U.S. Department of Transportation Federal Aviation Administration Air Traffic Organization Operations Planning Office of Aviation Research and Development Washington, DC 20591	Final Report
	14. Sponsoring Agency Code AIR-6A1

15. Supplementary Notes

The FAA Aviation William J. Hughes Technical Center Research Division COR was William Emmerling.

16. Abstract

Because of effects of twinning and texture evolution, the yield surface for hexagonal close-packed (HCP) metals display an asymmetry between the yield in tension and compression. A generalized isotropic yield surface model is presented that can describe both the yielding asymmetry and distortional hardening (stress-state-dependent hardening) on the pressure-independent plastic response of metals. The yielding is described mathematically by a newly developed macroscopic phenomenological function that accounts for the asymmetry. This yield criterion also provides flexibility for the yield stress in pure-shear compared to von Mises plasticity. Therefore, it can also be used to model face-centered cubic and body-centered cubic materials, and HCP materials.

The constitutive relationship models the plastic behavior of metals as a function of the state of stress, strain rate, and temperature. It uses a higher than quadratic order, isotropic, isochoric, generalized yield function with stress-state dependent hardening. The distortional hardening includes strain rate and thermal effects using tabulated input curves for yield-strain rate and yield-temperature dependency. The model also includes adiabatic heating due to the plastic work, and the resulting thermal softening.

This Generalized Yield Surface (GYS) model was implemented into the explicit finite element program LS-DYNA®. Characterized material test results are used to create the tabulated inputs to the GYS material model, and is demonstrated using a Ti-6Al-4V sample. Comparisons between predicted and measured force-displacement curves and macroscopic strain fields of this Ti-6Al-4V alloy show that GYS can accurately describe the yield strength differential effect and distortional hardening (stress-state dependent hardening), based on the uni-axial tension, uni-axial compression, and pure-shear stress-states.

17. Key Words	18. Distribution Statement
LS-DYNA, Tabulated Material Failure, Triaxiality, Lode, MAT_TABULATED_JOHNSON_COOK_GYS, MAT_224_GYS, Yield, Plasticity	This document is available to the U.S. public through the National Technical Information Service (NTIS), Springfield, Virginia 22161. This document is also available from the Federal Aviation Administration William J. Hughes Technical Center at actlibrary.tc.faa.gov.

19. Security Classif. (of this report)	20. Security Classif. (of this page)	21. No. of Pages	22. Price
Unclassified	Unclassified	141	

TABLE OF CONTENTS

LIST OF FIGURES

LIST OF TABLES

LIST OF ACRONYMS

BCC	Body-centered cubic
DIC	Digital image correlation
FCC	Face-centered cubic
FEA	Finite element analysis
GYS	Generalized yield surface
HCP	Hexagonal close-packed
SD	Strength differential

LIST OF SYMBOLS

ROMAN SYMBOLS

a_1, b_1, c_1	Material constants for the plasticity model of Gao [44]
$\boldsymbol{C}$	Fourth order positive definite isotropic stiffness tensor
$c_1,\ c_2,\ c_3$	GYS material coefficients or hardening parameters
C_{ijkl}	Elastic tensor in the component form
C_p	Specific heat
$\dot{\boldsymbol{e}}$	Deviatoric strain rates
$\dot{\boldsymbol{e}}_{\boldsymbol{p}}$	Plastic deviatoric strain rate
E	Modulus of elasticity
f	Yield function
G	Shear modulus
g	Plastic potential
H	Hessian matrix
I	Second-order unit tensor
$\mathbb{I}$	Fourth-order, symmetric unit tensor
I_1, I_2, I_3	Stress invariants
J_1, J_2, J_3	Deviatoric stress invariants
K	Bulk modulus
k	Order of the Karafillis yield function
L	Current length
L_0	Initial length, gauge length
m	Order of the Hosford yield function
M	Moment
M_1, M_2, M_3	Principal minors of Hessian matrix
N	Prandtl-Reuss normal outward flow vector
N_{pq}	Curvature tensor
n	Yield surface normal
n	Order of the Hosford yield function
p	Pressure
$\dot{p}$	Pressure rate
p^{n+1}	Updated pressure
p_e^{n+1}	Trial pressure
P	Load
$\dot{\mathbf{s}}$	Deviatoric stress rates
s_1, s_2, s_3	Deviatoric principal stresses
s_{ij}	Deviatoric stress tensor
$\dot{\boldsymbol{s}}_{\text{trial}}$	Deviatoric trial stress

$t, t_{n+1/2}, t_{n+1}$	Time increments
T	Temperature
T	Torque
T_{melt}	Melting temperature
T^*	Homologous temperature
T^n	Current temperature
T_{room}	Room temperature
tr	Trace of a tensor or matrix
W^p	Plastic work

GREEK SYMBOLS

β	Taylor–Quinney coefficient
γ	Engineering shear strain
δ_{ij}	Kronecker delta
t	Yield stress in pure-shear
$\Delta\boldsymbol{\varepsilon}_p$	Plastic strain increment tensor
$\boldsymbol{\varepsilon}$	Strain tensor
$\dot{\boldsymbol{\varepsilon}}$	Strain rate (rate-of-deformation) tensor
$\bar{\varepsilon}^p_{eff}$	Effective plastic strain
$\bar{\varepsilon}^p_n$	Effective plastic strain at the beginning of time step
$\dot{\boldsymbol{\varepsilon}}^e$	Elastic components of the rate of the strain tensor
$\dot{\boldsymbol{\varepsilon}}^p$	Plastic components of the rate of the strain tensor
$\dot{\varepsilon}^V$	Volumetric strain rate
$\dot{\varepsilon}^V_p$	Plastic volumetric strain rate
ε^p_t, ε^p_c, ε^p_s	True plastic strain in uni-axial tension, uni-axial compression, and pure-shear
$\bar{\varepsilon}_p$	Equivalent plastic strain
θ	Lode angle
θ_L	Lode-angle-parameter
λ	Plastic multiplier
$\dot{\lambda}$	Rate of plastic multiplier
μ	One of the Lamé constants ($\mu = G$)
ν	Poisson's ratio
π	The number Pi
ρ	Density
η	Eigenvalue
$\boldsymbol{\sigma}$	Cauchy stress tensor
σ_{eff}	Effective stress of GYS model
σ_{bez}	Equivalent stress in Vegter model

$\sigma_1, \sigma_2, \sigma_3$	Principal stresses
$\sigma_t, \sigma_c, \sigma_s,$	Yield stress in uni-axial tension, uni-axial compression and shear
σ_{ij}	Second-order stress tensor
σ_H	Hydrostatic stress
σ_{kk}	Trace of the stress tensor
σ_m	Mean stress
σ_{vm}	von Mises stress
σ_y	Yield, flow stress
σ_{vm}^{n}	Initial von Mises stress
σ_{vm}^{n+1}	Updated von Mises stress
σ_y^n	Initial yield stress
σ_y^{n+1}	Updated yield stress
$\sigma_{y,e}^{n+1}$	Trial yield stress
τ	Shear stress
ϕ	Twist angle and yield function in Karafillis-Boyce model
φ	Vegter yield function

SUBSCRIPT / SUPERSCRIPT

i, j, k, l, m, p	Indices
x, y, z	Cartesian coordinate indices
$1,2,3 \ldots, n$	Indices
$n, n+1$	Time increments
H	Hydrostatic
p	Plastic
vm	von Mises
trial	Trial prediction
y	Yield

EXECUTIVE SUMMARY

Because of effects of twinning and texture evolution, the yield surface for hexagonal close-packed (HCP) metals display an asymmetry between the yield in tension and compression. A generalized isotropic yield surface model is presented that can describe both the yielding asymmetry and distortional hardening (stress-state-dependent hardening) on the pressure-independent plastic response of metals. The yielding is described mathematically by a newly developed macroscopic phenomenological function that accounts for the asymmetry. This yield criterion also provides flexibility for the yield stress in pure-shear compared to von Mises plasticity. Therefore, it can also be used to model face-centered cubic and body-centered cubic materials, and HCP materials.

The constitutive relationship models the plastic behavior of metals as a function of the state of stress, strain rate, and temperature. It uses a higher than quadratic order, isotropic, isochoric, generalized yield function with stress-state dependent hardening. The distortional hardening includes strain rate and thermal effects using tabulated input curves for yield-strain rate and yield-temperature dependency. The model also includes adiabatic heating due to the plastic work, and the resulting thermal softening.

This Generalized Yield Surface (GYS) model was implemented into the explicit finite element program LS-DYNA®. Characterized material test results are used to create the tabulated inputs to the GYS material model, and is demonstrated using a Ti-6Al-4V sample. Comparisons between predicted and measured force-displacement curves and macroscopic strain fields of this Ti-6Al-4V alloy show that GYS can accurately describe the yield strength differential effect and distortional hardening (stress-state dependent hardening) based on the uni-axial tension, uni-axial compression, and pure-shear stress-states.

This research was conducted under FAA cooperative agreement 13-G-020 and sponsored by the Aircraft Catastrophic Failure Prevention Program.

1. INTRODUCTION

1.1 Introduction

Inelastic behavior of materials has challenged engineers and researchers over many decades. Sustained interest in this topic is based on its direct relevance in numerous engineering applications. It is difficult to accurately predict inelastic deformation when the material is subjected to complex mechanical loading, in which the material is subjected to a multi-axial state of stress, high strain rates, and variable temperature conditions. The accurate representation of stress, strain, and temperature fields within the structural components depends strongly on the mathematical representations or constitutive equations of the inelastic behavior of these materials.

It is vital to understand the dynamic plastic deformation characteristics of structures to design better-engineered products. Designing lighter and more cost-effective structures under impact loading without any compromise in structural performance, safety, and integrity has been one of the most important areas of research in mechanics for several decades. Dynamic plastic deformation and failure applications can be extended to aircraft safety, spacecraft shielding, high-speed machining, and armor penetration. Some specific applications of ductile dynamic deformation and failure are shown in figure 1 for automotive crashworthiness, uncontained engine debris protection in aerospace applications, fan blade containment during the fan blade-out event, and defense-armor penetration. The circumstances that are shown in figure 1 demonstrate the importance of successfully predicting the dynamic plastic deformation and subsequent failure for engineering practice, in which an unsuccessful prediction may put the engineering structure in jeopardy.

For computational modeling of impact loading on metallic materials, ductile failure occurs after a significant amount of plastic deformation followed by material instability that leads to necking or shear localization. Therefore, the correct representation of yielding and subsequent plastic flow is crucially important on the numerical simulation of impact problems. For some metals, yield stress and subsequent flow stress might be different in uni-axial compression than in tension. This phenomenon is known as the strength differential (SD) effect in yielding and is mostly seen with hexagonal close-packed (HCP) metals, such as magnesium and titanium alloys, which offer great potential to reduce weight, therefore replacing the most commonly used materials.

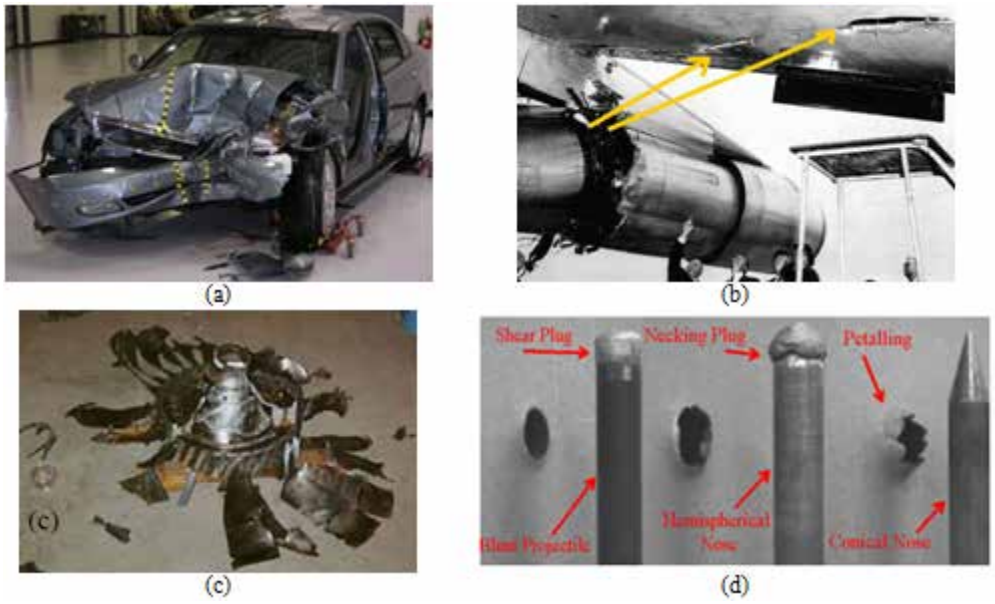

Figure 1. Applications of dynamic ductile deformation and subsequent failure for different structures: (a) offset frontal crash of a passenger car (http://www.iihs.org), (b) uncontained aircraft engine failure (http://www.ntsb.gov), (c) fan disk failure, and (d) different failure modes after ballistic impact of projectiles with different nose shapes, adapted from (Borvik, et al., 2002)

Currently, the use of HCP metals has not yet been optimized because of a lack of fundamental understanding of their complex flow behavior under a multi-axial stress state, and a lack of a representative rate- and temperature-dependent phenomenological Generalized Yield Surface (GYS) model for computational analysis.

Experimental results underscore another need for improved model representations of variations in yield stress. Pure-shear yield ratio of some metals relative to the uni-axial tension yield might differ from $1/\sqrt{3}$, which is a fixed ratio in classical J_2 (von Mises) plasticity. This situation can be observed in face-centered cubic (FCC), body-centered cubic (BCC), and HCP metals. Yielding in shear stress can be important during shear localization before ductile failure occurs.

The SD effect in yielding and deviations from a fixed ratio of pure-shear yield relative to uni-axial tension yield for metals establishes the need for material models with a generalized yield function to capture these effects in computational analysis. Because nonlinear explicit finite element analysis (FEA) is the most popular tool used for the computational analysis of impact problems, commonly used material models in these codes, such as Johnson-Cook MAT_15 or Piecewise Linear Plasticity MAT_24 in LS-DYNA®, use classical J_2 (von Mises) plasticity (Hallquist, 2009). Deviations from J_2 flow in metal plasticity cannot be captured within the capability of these material models.

To address this deficiency, this report presents a new viscoplastic material model with a GYS that incorporates state of stress, temperature, and strain rate effects to predict plastic response during ductile deformation. The new model is supported by an experimental program to characterize the

material properties for the model input. Results of a parallel experimental program are used to validate the accuracy and robustness of the model.

1.2 Background and Motivation

Uncontained turbine engine debris present risks to an aircraft, in which high-energy fragments impacting the aircraft need to be considered. Damage from an engine rotor burst can be catastrophic, compromising structural integrity, initiating a fire, endangering critical systems, or putting lives in danger (National Transportation Safety Board, 1990), (National Transportation Safety Board, 1998). Title 14 Code of Federal Regulations (CFR) requires that aircraft be designed to minimize and mitigate these risks. 14 CFR 25.903(d) (1) states: "Design precautions must be taken to minimize the hazards to the airplane in the event of an engine rotor failure." There is, therefore, significant interest in methods that can be applied to better understand events and improve aircraft designs. Following a catastrophic uncontained fan disk failure in commercial passenger service in 1989 (National Transportation Safety Board, 1990), the FAA initiated a research program called Uncontained Engine Debris Mitigation Program, part of the Aircraft Catastrophic Failure Prevention Program, to investigate methods for analyzing and compensating for uncontained engine debris mitigation. Different methods were suggested to minimize the hazards, although it was understood that absolute containment is unlikely and that, consequently, the minimization of fragment energies and developing of mitigation strategies in the aircraft were the reasonable methods of compliance (FAA, 1999).

Civil aviation authorities also require that turbine engines in civil service be designed to contain the release of any single fan, compressor, or turbine blade. To demonstrate compliance, 14 CFR 33.94 requires every new civil engine design be tested to prove that the highest energy blade will be contained (14 CFR part 33.94, 2009). After successful demonstration of the highest energy blade, the other stages in the engine are certified by analysis. Considering the cost, difficulty, and time demands of performing such tests, the engine manufacturers want to be sure that a new engine will pass the first time it is tested. Therefore, predictive numerical models and analyses of the containment structures are used during the design process to reduce the risk of having to repeat the blade containment test. Computational mechanics has evolved to a level that performance of structures under impact loading can efficiently and effectively be predicted by employing numerical techniques with high accuracy if accurate material models are used (Wilkins, 1978, Zukas, 1982, Zukas, 1994). There is a significant body of literature about the assessment of dynamic plastic deformation and failure on the impact performance evaluation of major aerospace materials, and their capacity to mitigate hazards from uncontained engine debris. The Johnson-Cook plasticity and fracture model is a phenomenological material model commonly used to simulate impact and penetration (Johnson & Cook, 1983, Johnson & Cook, 1985). This constitutive model defines the effective material flow stress as a function of strain rate, temperature, and effective plastic strain. However, there is no difference between yielding in uni-axial tension and yielding in uni-axial compression in this model, and the ratio of pure-shear yield to uni-axial tension yield is fixed at a value of $1/\sqrt{3}$ (0.577). This means that the material model uses classical J_2 (von Mises) plasticity, and cannot model yielding asymmetry or the SD effect in uni-axial tension, uni-axial compression, or pure-shear stress states. Therefore, a stress-state-dependent GYS is needed to capture the deviations from classical J_2 plasticity to make sure that the stress state dependency of initial yielding and subsequent plastic flow are adequately treated by the material model. All these models, whether phenomenological or physics-based, require

experimental data for calibration of parameters. Because results from numerical simulations are dependent on the material models, they are also dependent on the experimental data used to calibrate these models. To be considered an improvement over the Johnson-Cook plasticity and fracture model, the proposed material model should have three basic input curves for most common tests of plasticity (uni-axial tension, uni-axial compression, and torsion for shear behavior) to be able to cover SD in yielding. This capability will improve the parameter calibration process and will be helpful to overcome the shortcomings of a calibration procedure based on the classical J_2 plasticity model, which allows the use of only one test as an input for the parameter calibration process.

Common failure mechanisms under impact loading were summarized by Backman (Backman, 1976) and Backman and Goldsmith (Backman & Goldsmith, 1978), and illustrations of these failure modes are categorized by Zukas, as shown in figure 2 (Zukas, 1982). Accurate prediction of plastic deformation and subsequent failure modes by numerical simulations is achievable only if a material model is used that uses explicitly defined stress-state-dependent plastic deformation and failure characteristics, and also incorporates strain rate and temperature softening (Perzyna, 1966).

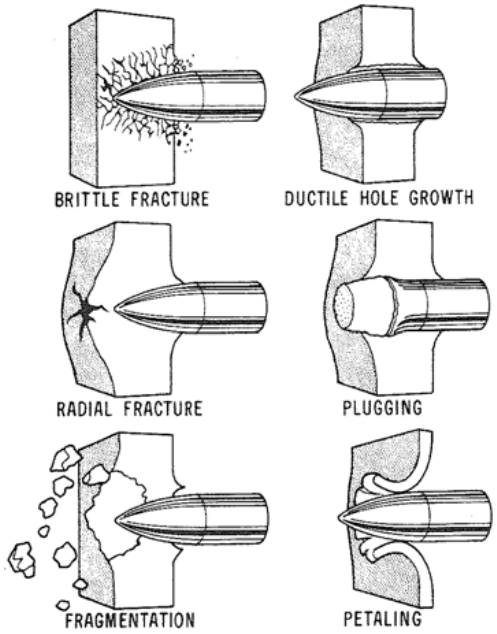

Figure 2. Failure modes in impacted plates, after (Zukas, 1982)

1.3 Research Objectives and Scope

As discussed in the motivation and background, a yield surface based solely on the second invariant of deviatoric stress tensor (J_2) is not able to correctly represent a material with a yield SD. The goal of the current work is to develop a GYS based on the second invariant of deviatoric stress tensor (J_2) and third invariant of deviatoric stress tensor (J_3) to account for the yield SD effect for uni-axial tension, uni-axial compression, and pure-shear stress states; and to develop a tabulated viscoplastic material model with a GYS that can incorporate high strain rate and temperature-softening effects.

Simulations of the deformation behavior of structures having length scales much larger than those of crystallographic grains cannot be performed effectively with crystal plasticity models. Such simulations require phenomenological constitutive equations for yielding and hardening under multi-axial stress states. The new material model described in this work has been developed using a phenomenological model approach at the macro level. Nano-scale or micro-scale concerns and phase transformation effects are not considered in this work.

A constitutive law of plastic deformation has been developed using small strain increment, rate-, and time-independent plasticity concepts. Transformation of the constitutive rate equation into an incremental equation has been done using a suitable semi-implicit integration procedure. The necessary rotations of stress and strain for large strain calculations are handled by LS-DYNA. The new material model is implemented into an explicit dynamics finite element code, LS-DYNA. This model is expected to be used as a generic tool to simulate plastic flow of any ductile metal under impact loading.

In the GYS model, the following assumptions have been made. Isotropic yielding and hardening are assumed. Anisotropic or orthotropic effects are not the subject of this work. Associated plastic flow is selected. Isochoric plasticity is assumed, so there is no volume change during plastic deformation. Dependence on stress triaxiality (pressure/von Mises) is excluded, so plastic flow is pressure insensitive. A multiplicative composition is assumed for the new proposed yield function in terms of J_2 and J_3 effects.

1.4 Original Contributions

The original contributions accomplished within the course of this research project can be summarized as:

A thermo-elastic/viscoplastic material model with a GYS in terms of the second and third stress deviator invariants was developed and implemented in LS-DYNA for isotropic materials exhibiting yield SD effect and pressure insensitivity. A new viscoplastic material model with higher order dependence on J_2 and J_3 is developed, which employs tabulated inputs of uni-axial tension, uni-axial compression, and pure-shear stress-strain curves to construct the flow surface as a function of state of stress, strain rate, and temperature. The convexity requirement is considered, and the constraints imposed on the material model are discussed.

This level of detail in the plasticity model is important for simulations involving ductile deformation, in which the failure is preceded by intense localization of plastic strain. In industrial applications, a new material model will provide independent yielding in uni-axial tension, uni-axial compression, and pure-shear while remaining isotropic for the nonlinear FEA of pressure insensitive metal plasticity. This provides greater flexibility to match experimental data in uni-axial tension, uni-axial compression, and pure-shear states at specimen level. Therefore, material characterization based on matching force-deflection curves at the specimen level will provide better-characterized data for the agreement between test and finite element simulations at the component level regarding ductile deformation and failure. The model has generic modular input for rate- and temperature-dependent stress-strain curves, so the flow surface is explicitly constructed through uni-axial tension, uni-axial compression, and pure-shear hardening curves at different strain rates and temperature.

The strain rate, temperature, strain dependent hardening law is updated at each time-step. This means that the yield surface is not limited to self-similar hardening as in previously existing models. The yield surface can both expand and deform. To include this distortional hardening, the effective stress is written not only as a function of the stress tensor, but also as a function of the plastic multiplier. In previous models, the yield function was typically written with the effective stress as only a function of the stress tensor.

The distortional hardening in the proposed model allows for the compression and tension plasticity to vary within a single simulation. For example, initially the tension may have a higher yield than the compression, but as the loading evolves, the compression may become greater than the tension yield stress. Modeling this type of behavior is important for accurate simulations of some alloys. The capability of modeling such behavior sets GYS apart from previously existing plasticity models.

It is successfully shown by the test programs that the state of stress has a significant role in the dynamic deformation and subsequent failure behavior of ductile materials under impact loading (Bai & Wierzbicki, 2008, Seidt, 2010, Lode von, 1926). Because the new material model shows successful prediction capability in stress-state-dependent plasticity, it has several advantages over previous models, particularly in predicting state dependent ductile failure; therefore, the new material model can also be used as a promising tool to evaluate the dynamic failure prediction. The model can be used for a wide range of applications including high-velocity impact analysis, vehicle crashworthiness, airworthiness, vulnerability, and survivability predictions.

1.5 Report Outline

This report consists of five interrelated sections.

Section 1 provides background information and motivation, defines objectives and scope, and presents an overview of the thesis.

Section 2 presents an overview of computational material models in structural metals. This chapter presents a review of the classical plasticity approaches currently used to model material plastic deformation. The general procedures used to implement these approaches are briefly described, and an assessment of the shortcomings associated with each approach is discussed. Deviations from classical J_2 plasticity are addressed, and the role of J_3 in material modeling of metal plasticity is discussed.

Section 3 provides a step-by-step explanation of the theoretical framework involved in developing a J_2- and J_3-dependent material model with GYS. Convexity of the proposed model has been discussed and details of the convexity region have been evaluated from a computational point of view.

Section 4 describes the numerical implementation of the new material model and describes single-element implementation testing. Numerical stability, accuracy, and robustness of the new model are assessed.

Section 5 presents an example of using the material model, in which mechanical property tests are simulated and compared with the test results of a Ti-6Al-4V titanium alloy. Force-deflection curves are used to compare test and numerical analysis using the GYS plasticity model.

Finally, Section 6 presents a summary of the main results.

2. LITERATURE REVIEW

2.1 Introduction to Yielding

The analysis of plastic deformation is important in many engineering applications, including crashworthiness, impact analysis, and manufacturing problems. When materials undergo plastic deformations, permanent strains develop when the load is removed. Many materials exhibit elastic-plastic behaviors (i.e., the materials exhibit elastic behavior up to a certain stress limit, called the yield strength, after which plastic deformation occurs).

For sufficiently small values of stress and strain, metals reassume their original shape on unloading. When loaded beyond this reversible (elastic) range, metals do not reassume their original shape on unloading, but exhibit a permanent (plastic) deformation. In the plastic range, the flow stress for metals typically increases monotonically with accumulated plastic strain. After a metal has been subjected to a stress exceeding the yield limit that separates the elastic and plastic ranges, the current stress becomes the new yield limit when the material is reloaded. For a multi-axial state of stress, a material's yield limit is mathematically described by a yield criterion.

Considering the general case of a three-dimensional stress state, for all combinations of three principal stresses, the locus of all stresses for which yielding occurs in principal stress space is called the yield surface. The yield surface is the three-dimensional analog of the two-dimensional yield curve and of the one-dimensional yield point. A state of stress inside the yield surface is elastic, a state of stress on the surface is plastic, and states of stress outside of the yield surface are not allowed, because the surface expands as the plastic state of stress evolves.

2.2 Isotropic Yield Criteria for Metals

At the continuum level, the initial material behavior is taken to be linearly elastic up to the yield point. The yield surface delineates the current elastic region in stress space. For an elastically isotropic metal, yielding depends on stress, temperature, strain rate, and internal state (described by hardening or internal state variables). Under isothermal conditions, initial yielding depends only on the stress state, which is often described by three stress invariants:

$$I_1 = \sigma_{ii} \tag{1}$$

$$J_2 = \frac{1}{2} s_{ij} s_{ij} \tag{2}$$

$$J_3 = \frac{1}{2}\, s_{ij} s_{jk} s_{ki} = s_1 s_2 s_3 \tag{3}$$

where I_1 is the first stress invariant, J_2 and J_3 are the second and third deviatoric stress invariants, respectively, and σ_{ij} and s_{ij} denote the Cauchy and deviatoric stress components, respectively. The yield function can be expressed as:

$$f(\sigma_{ij}) = f(I_1, J_2, J_3) \leq k^2 \tag{4}$$

Physically, I_1 represents the hydrostatic stress, and J_2 represents the distortional energy in the material. Though no definite physical quantity is attributed to J_3, it can be treated as a weighting parameter that induces asymmetry in yield and flow behavior between tension and compression. In this formulation, *k* is a constant.

Historically, the oldest isotropic yield criterion was proposed by Tresca in 1864 (Tresca, 1864). He experimented with plastic squeflow of metals under high pressure (extrusion of a metal through die). He concluded that yielding depends on maximum shear stresses so hydrostatic pressure is insignificant. According to Tresca's criterion, the material transitions to a plastic state when the maximum shear stress reaches a critical value. The Tresca criterion is given by:

$$Max\{|\sigma_1 - \sigma_2|, |\sigma_2 - \sigma_3|, |\sigma_3 - \sigma_1|\} = \sigma_y \tag{5}$$

where σ_1, σ_2, and σ_3 are the principal stresses, and σ_y is the yield stress in uni-axial tension.

Possibly the most widely used isotropic yield criterion is the one proposed independently by Huber (Huber, 1903) in 1904 and von Mises (von Mises, 1913) in 1913. This criterion is usually referred to as the von Mises criterion. The von Mises criterion is based on the observation that a hydrostatic pressure cannot cause yielding of the material. The plastic state corresponds to a critical value of the elastic energy of distortion:

$$J_2 = k^2 \tag{6}$$

where *k* is a constant, and J_2 is the second invariant of the Cauchy stress deviator given by:

$$J_2 = \frac{1}{6}[(\sigma_1 - \sigma_2)^2 + (\sigma_2 - \sigma_3)^2 + (\sigma_3 - \sigma_1)^2] \tag{7}$$

or, alternatively:

$$J_2 = \frac{1}{2}[(s_1)^2 + (s_2)^2 + (s_3)^2] \tag{8}$$

where s_1, s_2, and s_3 are the principal values of the Cauchy stress deviator, defined as:

$$s_{ij} = \left[\sigma_{ij} - \frac{1}{3}\sigma_{kk}\delta_{ij}\right] \tag{9}$$

The von Mises yield criterion is also known as the maximum distortional energy criterion, and yielding is presumed to occur when the distortional strain energy density at some point in a body with a multiaxial stress state is equal to the distortional strain energy density at yielding under uni-axial tension or compression.

$$\sigma_{vm} = \frac{1}{\sqrt{2}} \sqrt{(\sigma_1 - \sigma_2)^2 + (\sigma_2 - \sigma_3)^2 + (\sigma_3 - \sigma_1)^2} = \sqrt{3J_2} = \sigma_y \quad (10)$$

where σ_y is the uniaxial tensile yield strength and σ_{vm} is the equivalent von Mises stress. In this equation, stresses are deviatoric stresses because only the distortional part of the energy is considered. Because of its direct association with J_2, the von Mises yield criterion is also known as the J_2 criterion.

In principal stress space, it is possible to select a plane on which the hydrostatic stress on the plane is zero, namely the plane perpendicular to the $\sigma_1 = \sigma_2 = \sigma_3$ axis through the origin. This plane is called π-plane or stress deviator plane and it is perpendicular to hydrostatic stress axis. The projection of Tresca's yield surface on the π-plane (the plane that passes through the origin of principal stress axis and is perpendicular to the hydrostatic axis) is a hexagon centered on the origin whose size depends on the magnitude of yield stress in uniaxial tension. The projection of the von Mises yield locus on the π-plane is a circle that circumscribes the Tresca hexagon, as shown in figure 3. The implication of the Tresca criterion is that yielding takes place at or below the loads at which yielding takes place according to von Mises yield criterion. These two yield criteria are easier to compare on the π-plane three-dimensional principal stress space. The two criteria coincide under uni-axial tension and uni-axial compression. The largest difference between the two criteria occurs under pure-shear, as shown in figure 4. That difference is $\frac{\sqrt{3}}{2}\sigma_y - \frac{1}{\sqrt{2}}\sigma_y$ calculated using the geometry of a regular hexagon. Therefore, the von Mises criterion predicts yielding in pure-shear at a stress nearly 16% higher than the Tresca criterion.

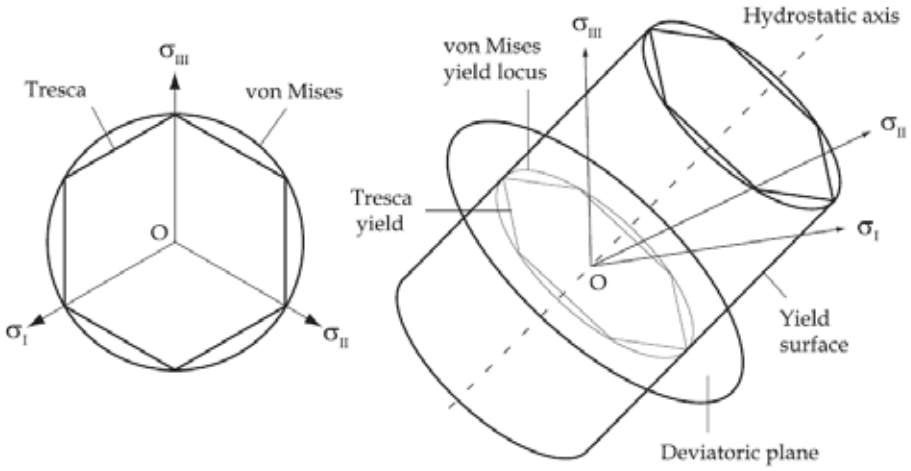

Figure 3. Tresca and von Mises yield criteria in the π-plane

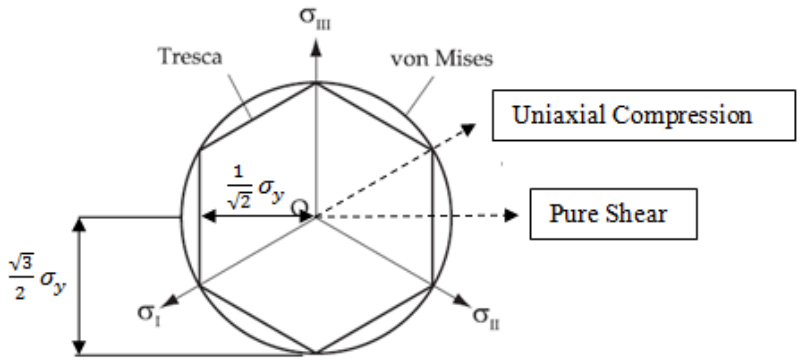

Figure 4. Difference of Tresca and von Mises yield criteria for pure-shear state in the π-plane

In separate studies, Lode (Lode von, 1926) and Taylor and Quinney (Taylor & Quinney, 1932) tested samples under combined loading and checked the yield surfaces of the materials of interest. Lode tested steel, copper, and nickel, whereas Taylor and Quinney tested copper, aluminum, and mild steel. The results of their findings are shown in figure 5 (a) for Lode and figure 5 (b) for Taylor and Quinney, in which it is shown that the materials of interest behave closer to the von Mises yield surface than to that from the Tresca theory.

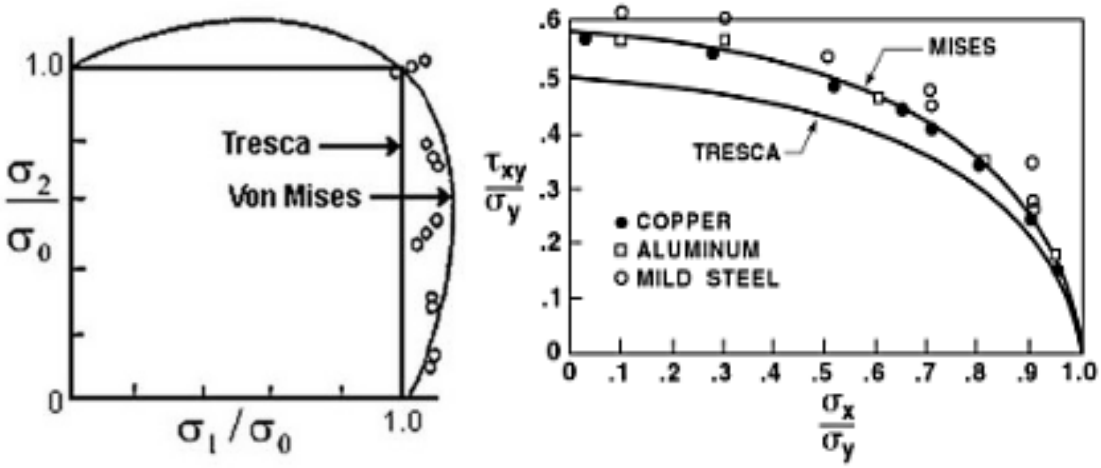

(a) (b)

Figure 5. Comparison of yield surfaces for different materials under combined loading: (a) after (Lode von, 1926), and (b) after (Taylor & Quinney, 1932)

2.3 Deviations from J_2 Plasticity and Higher-Order Yield Surfaces

A yield function is called quadratic if it is a function of the squares of the component of the stress tensor. The von Mises criterion (J_2 plasticity) is the most general quadratic yield function for isotropic materials and requires only one constant: the yield stress from either an uni-axial tension or compression test. The multi-axial response of the material is fully determined by the results of a uni-axial test. Therefore, yield strength in the pure-shear state relative to the tensile yield strength has a fixed ratio of 0.577 in J_2 (von Mises) plasticity. Additionally, the yield stress in uni-axial

tension is always identical to the yield stress in uni-axial compression. Mendelson has shown the existence of bounds in an isotropic yield surface of a material with a fixed yield stress in uni-axial tension (Mendelson, 1968). These bounds are derived after symmetry and convexity considerations. The lower bound coincides with the limiting maximum shear stress yield surface as described by Tresca (Tresca, 1864) in 1864, whereas the upper bound corresponds to a limiting value of the sum of the two greater diameters of Mohr's circles as mentioned by Hosford (Hosford, 1972) in 1972. Higher-order (higher than quadratic order) GYSs are needed to capture the family of yield surfaces, swapping stress space between lower and upper bounds rather than the quadratic yield surfaces (von Mises). As a result, J_2 (von Mises) plasticity cannot describe certain phenomena in isotropic metals, such as:

- Yield stress in pure-shear different than 0.577 times the tensile yield stress
- Characterization of the family of yield surfaces between lower bound (Tresca) and von Mises or between von Mises and upper bound
- Tensile-Compressive asymmetry in yielding

From the phenomenological viewpoint, higher-order nonquadratic yield functions were proposed for metallic materials to characterize the yield behavior under multiaxial loading conditions. For examples, see (Drucker, 1949, Hershey, 1954, Hosford, 1972, Karafillis & Boyce, 1993, Cazacu & Barlat, 2001, and Cazacu & Barlat, 2004). Higher-order terms of the stresses in these yield functions are needed to characterize the rounded vertices of the yield surface in the stress space.

Drucker (Drucker, 1949) in 1949 extended J_2 plasticity theory to account for deviations from classical plasticity. Drucker compared experimental data on aluminum alloy tubes to classical Tresca and von Mises yield criterion. Whereas neither the Tresca criterion nor the Mises criterion agreed well with the experimental data, a function of the form:

$$f(J_2, J_3) = J_2^3 - cJ_3^2 \tag{11}$$

was proposed, and a yield surface corresponding to a value of 2.25 for the parameter *c* gave an excellent correlation with the experimental data on 24S-T aluminum alloy (Drucker, 1949). This was one of the first yield functions to go beyond the J_2 representation of yield for metallic materials. In this model, the yield surface is located between those of Tresca and von Mises, as shown in figure 6.

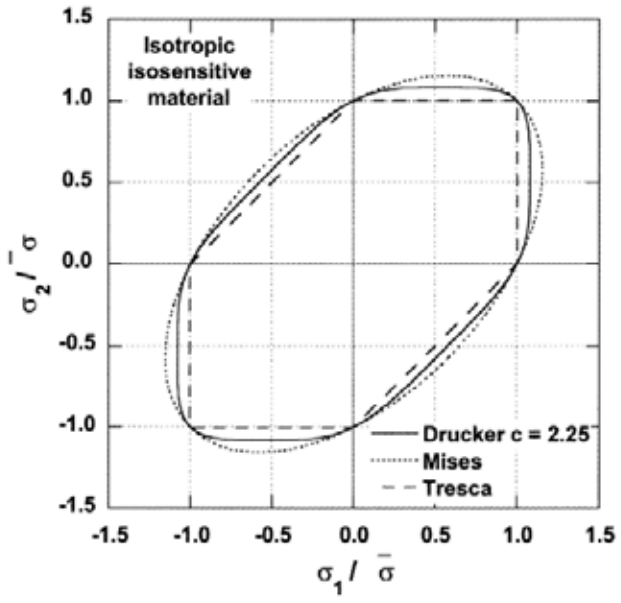

Figure 6. Plane stress yield loci for Drucker, Tresca, and von Mises (normalized by uniaxial tension) after Drucker (Drucker, 1949)

Based on self-consistent polycrystal calculations, Hershey (Hershey, 1954) introduced a higher-order criterion later used by Hosford. Hosford (Hosford, 1972) proposed a higher-order, generalized form of an isotropic yield criterion, which can be used to approximate experimental and theoretical results more closely than either the von Mises or Tresca yield functions. Hosford's yield function is expressed as:

$$\left[\frac{(\sigma_1-\sigma_2)^n+(\sigma_2-\sigma_3)^n+(\sigma_1-\sigma_3)^n}{2}\right]^{1/n} = \sigma_y \qquad (12)$$
$$\sigma_1 \geq \sigma_2 \geq \sigma_3 \text{ and } 1 \leq n \leq \infty$$

where σ_1, σ_2, and σ_3 are the principal stresses, σ_y is the yield stress from a uni-axial tension or compression, and the exponent *n* is a material-dependent exponent and need not be an integer. The Hosford yield function reduces to the von Mises and Tresca yield functions for $n = 2$ and for $n = 1$, respectively. For values of the exponent greater than 4, this criterion predicts yield loci between those of Tresca and von Mises, as shown in figure 7 (a). Theoretically derived loci for randomly oriented FCC and BCC materials suggest exponents $n = 6$ for BCC and $n = 8$ for FCC materials. These values fit experimental data well, as shown in figure 7 (b) (Hutchinson & Jun, 1964, Hill, 1950a). The ratio of yielding in pure-shear to yielding in uni-axial tension can be adjusted using the exponent *n* in the Hosford model.

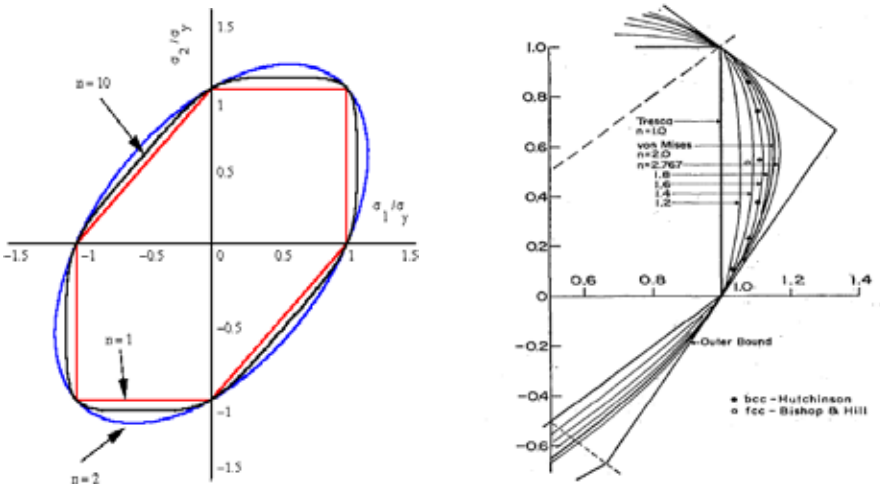

(a) (b)

Figure 7. Plane stress yield loci for Hosford, Tresca, von Mises: (a) *n* = 1, Tresca; *n* = 2, von Mises; and *n* = 10, Hosford; and (b) plane stress yield loci predictions for different *n* values between 1 and 2.767, as shown by (Hosford, 1972)

Hosford's formulation has been generalized by Karafillis and Boyce (Karafillis & Boyce, 1993) in the following form:

$$\emptyset = (1-c)\emptyset_1 + c\,\frac{3^{2k}}{2^{2k-1}+1}\emptyset_2 = 2\sigma_y^{2k} \tag{13}$$

where

$$\emptyset_1 = |s_1 - s_2|^{2k} + |s_2 - s_3|^{2k} + |s_1 - s_3|^{2k} = 2\sigma_y^{2k} \tag{14}$$

and

$$\emptyset_2 = |s_1|^{2k} + |s_2|^{2k} + |s_3|^{2k} = \frac{2^{2k}+2}{3^{2k}}\sigma_y^{2k} \tag{15}$$

Here, s_1, s_2, and s_3 are the principal deviatoric stresses, c is a weighting coefficient, and $2k$ is an exponent having the same significance as the exponent n in Hosford's criterion.

For k = 1, $\emptyset_1$ and $\emptyset_2$ take the form given by von Mises; however, for $k=\infty$, $\emptyset_1$ becomes the Tresca function, and $\emptyset_2$ gives an upper limit of the yield surface. Therefore, $\emptyset_1$ describes the yield surfaces between the lower bound (Tresca) and von Mises, and $\emptyset_2$ describes the yield surfaces between von Mises and the upper bound. In this work, k is an integer with values varying from +1 to $+\infty$. Therefore, the exponent in $\emptyset_1$ and $\emptyset_2$ is always an even integer, thereby ensuring identical tensile and compressive yield stress for the yield function $\emptyset$. The value of the coefficient c is in the range [0, 1] and determines the weight of the functions $\emptyset_1$ and $\emptyset_2$ in the yield function $\emptyset$. As a consequence, there are two parameters, k and c, that may be used to "adjust" the shape of the yield locus, whereas the Hosford criteria use only one parameter (exponent n) for this purpose. A generic isotropic yield surface should be able to describe all yield surfaces lying between the lower bound

(Tresca) and the upper bound yield surface. By varying the value of *k* and *c*, a family of yield surfaces swaps the space between lower bound and upper bound in the Karafillis-Boyce criterion, as shown in figures 8–9. However, the Hosford criterion swaps the space between lower bound and von Mises. Therefore, the Karafillis and Boyce criterion is more flexible than Hosford's model.

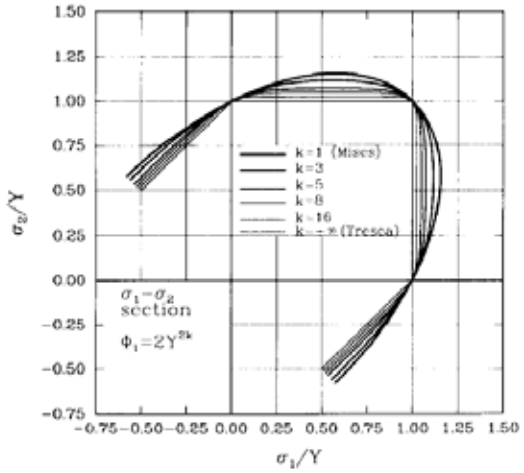

Figure 8. Different isotropic plane stress yield surfaces between the von Mises yield surface and the lower bound (Tresca) after (Karafillis & Boyce, 1993)

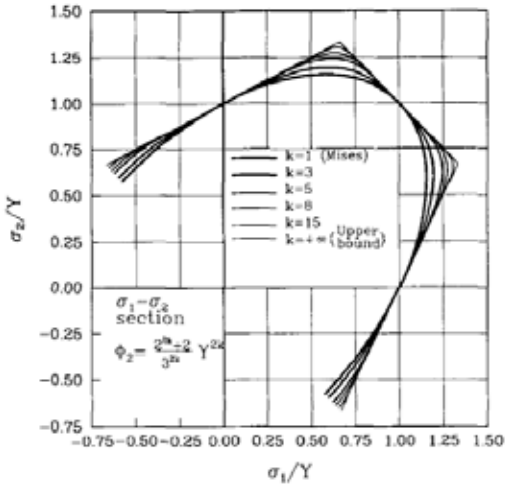

Figure 9. Different isotropic plane stress yield surfaces between the von Mises yield surface and the upper bound after (Karafillis & Boyce, 1993)

In 1995, Vegter (Vegter, et al., 1995) proposed an isotropic plane stress yield description, which directly uses the experimental results at multi-axial stress states as follows:

$$\varphi = \sigma_{bez} - \sigma_y \tag{16}$$

$$\sigma_{bez} = \frac{\sigma_1}{(1-\beta)^2 p_1^{r1} + \beta^2 p_1^{r2} + 2\beta(1-\beta) p_1^h} \tag{17}$$

where σ_{bez} is a kind of equivalent stress, σ_y is the yield stress, p_1^{r1} and p_1^{r2} are reference points, and p_1^h is the hinge point for second order Bezier interpolation.

In this model, a four-point interpolation method has been developed based on the pure-shear point, the uni-axial point, the plane strain point, and equi-biaxial point in principal stress space, as shown in figure 10. A yield surface is constructed using the four reference points and the gradient. Three Bezier splines using pure-shear, uniaxial tension, plane strain tension, and equi-biaxial tension are used to describe a quarter of the yield function. This yield function is a multifaceted yield function. The advantage of using Bezier interpolation is that the normal of the yield function is continuous in the reference points. The Vegter model assumes tensile-compressive symmetry in yield stress and is limited to plane stress case, which is useful for sheet metal applications only.

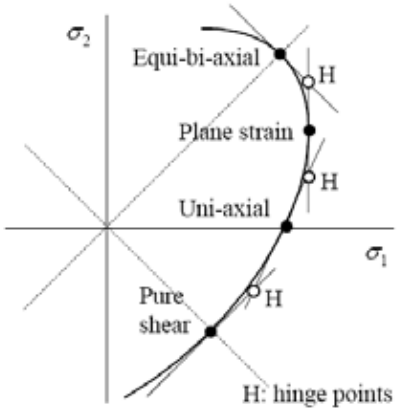

Figure 10. The four reference points to construct the Vegter yield function in plane stress after (Vegter, et al., 1995)

2.4 Role of Third Deviatoric Stress Invariant (J_3) in Modeling Asymmetry between Tensile and Compressive Yield

Higher-order yield surfaces mentioned in the previous section are able to handle deviations from J_2 plasticity regarding yield strength in pure-shear and characterization of the family of yield surfaces between the lower bound and the von Mises yield surface, or between the von Mises yield surface and the upper bound. However, these functions cannot handle tensile-compressive asymmetry in yielding. A proposed yield function should be an odd function of J_3, or an odd function of deviatoric principal stresses, to address the tension-compression asymmetry in yielding.

Starting from the mid-1960s, experimental results were published that show yield and subsequent flow stresses in tension and compression are different for some metals (Spitzig, et al., 1976, Rauch & Leslie, 1972, Chait, 1972, Spitzig & Richmond, 1984). This phenomenon, known as the SD effect in yielding, is observed for a wide range of temperatures and strain rates. The SD effect has been observed in many iron-based metals, such as plain carbon or low alloy steels, cast iron, high-strength steels, and in some metals, such as titanium, aluminum, magnesium, and nickel-based super alloys, such as Inconel.

The SD effect can be mathematically defined as (Spitzig, et al., 1976):

$$SD = \frac{(\sigma_c - \sigma_t)}{(\sigma_c + \sigma_t)} \tag{18}$$

where σ_c and σ_t are yield strengths in uni-axial compression and uni-axial tension, respectively. According to this expression, the higher the absolute value of SD, the stronger the SD effect. For an isotropic material exhibiting SD, a yield function that only depends on J_2, or an even function of J_3, will not give an accurate representation of the material behavior.

BCC and FCC materials tend to deform by slip because of the large number of available slip systems. However, HCP materials, in which the number of potential slip systems is limited, also tend to twin as an alternate mechanism to accommodate an imposed deformation (Hosford &

Allen, 1973, Hosford, 2005). Therefore, twinning and slipping both contribute to SD effect for HCP materials. Plastic deformation of polycrystalline metals occurs by either slip or twinning (see figures 11–12). Whether slipping or twinning is the dominant deformation mechanism depends on which mechanism requires the least stress to initiate and sustain plastic deformation. In low symmetry materials, such as HCP metals, which have too few slip systems to accommodate any shape change, twinning may become a dominant mechanism.

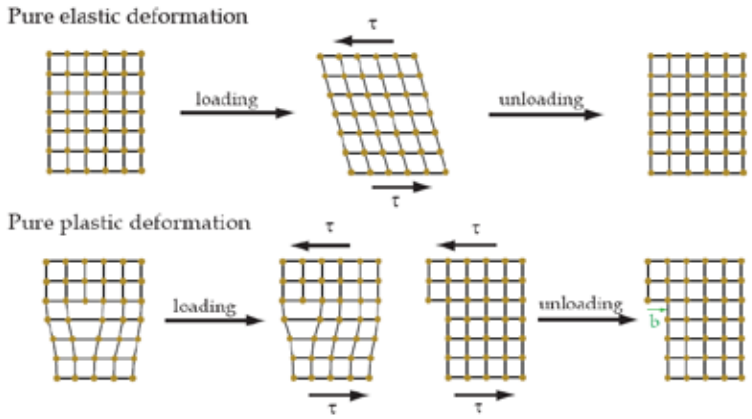

Figure 11. Elastic deformation corresponding to pure stretching of the crystal lattice (top) and plastic deformation through dislocation slip (bottom) (Hosford & Allen, 1973, Hosford, 2005)

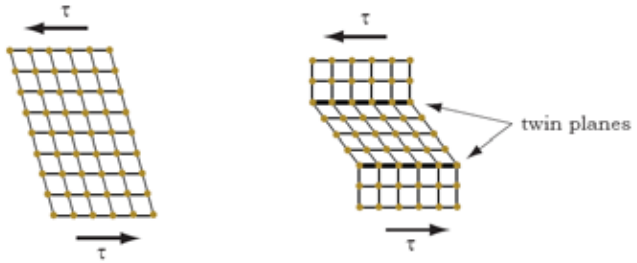

Figure 12. Crystal lattice reorientation due to mechanical twinning (Hosford & Allen, 1973, Hosford, 2005)

Twinning, unlike slip, is sensitive to the sign of the applied stress (i.e., if a particular twinning can be formed under a shear stress, it will not be formed by a shear stress of opposite sign). Because of the polar nature of twinning, HCP materials display a strong asymmetry between the yield in tension and compression. As HCP metals are pressure insensitive, the dependence of the yield condition on the first stress invariant should be neglected, and the effect of the third stress deviator invariant J_3 becomes important. Studies by Raniecki and Mroz, Iyer and Lissenden, and Cazacu and Barlat provide formulations of yield conditions and flow potentials for magnesium alloys and nickel base alloys, assuming dependence on the third stress deviator invariant (Raniecki, & Mro´z, 2008, Iyer & Lissenden, 2003, Mirone & Corallo, 2010).

Cazacu-Barlat (Cazacu & Barlat, 2004) introduced a yield function for pressure-insensitive metals exhibiting SD effect in the form of:

$$f(J_2,J_3) = J_2^{3/2} - cJ_3 = \tau_y^3 \tag{19}$$

where τ_y is the yield stress in pure-shear, and *c* is a material parameter. The constant *c* represents the SD effect in yielding in the form of:

$$c = \frac{3\sqrt{3}(\sigma_t^3 - \sigma_c^3)}{2(\sigma_t^3 + \sigma_c^3)} \tag{20}$$

where σ_c and σ_t are yield strengths in uni-axial compression and uni-axial tension, respectively. For equal yield stresses in tension and compression, the proposed criterion reduces to the von Mises yield criterion. The Cazacu-Barlat model was applied to magnesium and titanium. As shown in figure 13, the shape of the yield locus is no longer elliptic in the plane stress case when the SD effect is taken into account in this model, becoming more like a triangle with rounded corners when tensile-compressive asymmetry is present.

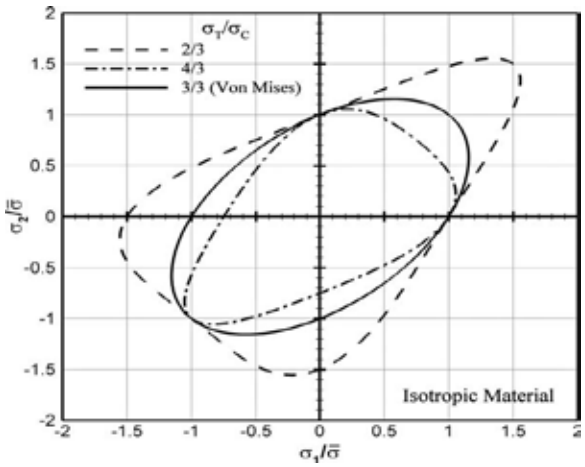

Figure 13. Plane stress yield loci corresponding to σ_t/σ_c =2/3, 3/3 (von Mises), 4/3 (Cazacu & Barlat, 2004)

According to many authors, the contribution of the effect of the third invariant is more severe than the contribution of pressure in the plastic flow (Bai & Wierzbicki, 2008, Mirone & Carollo, 2010, Gao, et al., 2009). In 2008, (Bai & Wierzbicki, 2008) discussed a pressure and Lode angle-dependent metal plasticity model and its application in failure analysis and proposed the following yield criterion:

$$\sigma_y = \bar{\sigma}(\varepsilon_p)\left[(1 - c_\eta)(\eta - \eta_0)\right]\left[(c_\theta^s)(c_\theta^{ax} - c_\theta^s)(\gamma - \frac{\gamma^{m+1}}{m+1})\right] \tag{21}$$

where $\bar{\sigma}(\varepsilon_p)$ is strain-hardening function, c_η is a material constant that needs to be calibrated and represents the effect of hydrostatic pressure on material plasticity, and η_0 is the reference value of stress tri-axiality from the reference test. The parameters γ and c_θ^{ax} are Lode angle-related parameters, where $c_\theta^{ax} = c_\theta^t$ for $\bar{\theta} \geq 0$ and $c_\theta^{ax} = c_\theta^c$ for $\bar{\theta} \leq 0$. The parameter *m* is a nonnegative integer. Four material constants, c_θ^s, c_θ^t, c_θ^c , and m, need to be calibrated. The values of c_θ^s, c_θ^t, and c_θ^c are relative, and at least one of them is equal to unity. This depends on which type of reference test is used for hardening $\bar{\sigma}(\varepsilon_p)$. For example, if a smooth round bar test is used, then c_θ^t=1; if a

torsion test is used, c_θ^s = 1; if a cylinder specimen test is used, c_θ^c = 1. Tensile-compressive asymmetry is introduced in the model when $c_\theta^t \neq c_\theta^c$. Bai and Wierzbicki worked on the experimental calibration based on the quasistatic test cases of Al2024-T351 material and concluded that percentage-wise, the correction for the hydrostatic pressure is small, and the magnitudes of correction due to the deviatoric state parameter (Lode angle parameter) is large, in some cases reaching 20%, as shown in figure 14.

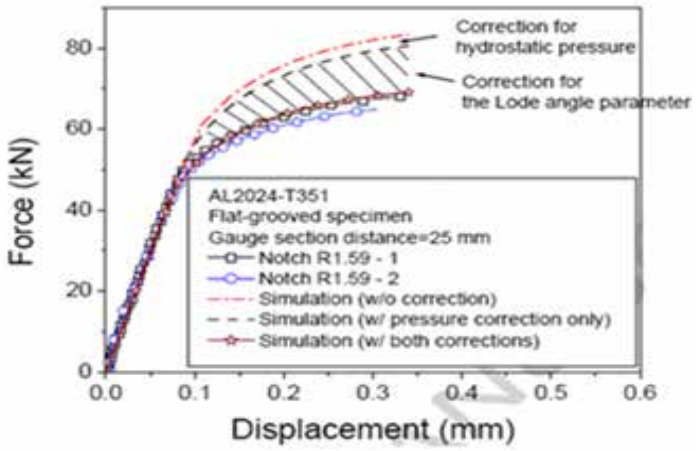

Figure 14. A comparison of force displacement curves between experimental results and simulation results for flat grooved specimen (Bai & Wierzbicki, 2008)

In 2009, Gao (Gao, et al., 2009) noticed the plastic response of a 5083 aluminum alloy is stress-state dependent. Mirone and Corallo (Mirone & Corallo, 2010) in 2010 found that, for the metals they tested, the hydrostatic stress plays a significant role in accelerating failure but has negligible effect on the stress-plastic strain relationship, whereas the Lode angle has a considerable effect in modifying the stress–strain curves. These findings agree with the findings by Gao (Gao, et al., 2009). Recently, in 2010, Gao (Gao, et al., 2010) proposed an elasto-plastic model, which is a function of hydrostatic stress and the second and third invariants of the stress deviator. A simple form of the yield function is given as follows:

$$f = c_1(a_1 I_1^6 + 27J_2^3 + b_1 J_3^2)^{1/6} \tag{22}$$

where $a_1, b_1,$ and c_1 are material constants. This yield function is a first-order homogeneous function of stress, and a_1 and b_1 can be found by manual calibration to have the best possible match compared to test data. The constant c_1 is dependent on a_1 and b_1. For $a_1 = b_1 = 0$, this plasticity model turns into J_3 flow. The calibrated model constants for the plasticity behavior of the 5083 aluminum alloy are found to be $a_1 = 0$ and $b_1 = -60.75$, which indicate no I_1 effect but significant J_3 effect on the plastic response of this material.

3. METHODOLOGY AND THEORETICAL FRAMEWORK

3.1 Fundamentals of Continuum Plasticity

A challenge in plasticity is to formulate a realistic mathematical model for describing the observed material behavior. The task is known as constitutive modeling, and the end product is a constitutive model or a set of constitutive equations. Various theories, using different approaches and points of view, have been proposed to formulate constitutive equations for metallic materials. Theories have also been formulated based on dislocation and slips. Currently, physically based polycrystal plasticity is emerging as a feasible method, and much effort is being devoted to bridging the gap between mechanics at the microscopic and continuum levels. In spite of the interest in plasticity at the micro level, the phenomenological (or continuum) approach is still the most practical computational mechanics method in industry.

In the continuum theory, the extension of one-dimensional plasticity into a multidimensional plasticity provides a great challenge, both experimentally and theoretically. In its early development, two major theories were developed: the deformation theory, and the flow theory. The deformation theory was proposed by Hencky in 1924 (Hencky, 1924). Deformation theory is also known as the total strain theory, because total strain is used. However, the flow theory uses the strain increment and is also known as the incremental theory. The deformation theory is convenient for use in solving problems with proportional loading because of its mathematical simplicity. The final state-of-strain is determined by the final state of stress. However, it is known that equations of deformation theory are not suitable for non-proportional loading conditions, and so use of the flow theory of plasticity is necessary.

The flow theory of plasticity describes the mechanical behavior of materials in the plastic range and includes energy dissipation, irreversible deformation, history- and path-dependent processes, the initial yield surface and its subsequent growth, the constitutive equation for plastic deformation, and criteria for loading and unloading.

According to flow theory, the constitutive equations of plasticity consist of a yield condition, a flow rule, a strain-hardening rule, and the loading-unloading conditions. The yield criterion determines the stress state (elastic or plastic state). The flow rule describes the increment of plastic strain when yielding occurs. The hardening rule describes how the material is strain-hardened as the plastic strain increases and determines the subsequent yield stress. The loading-unloading conditions specify the expression, which ensures no plastic strain occurs while unloading. These are the major concepts of the flow theory.

Any given stress tensor, $\boldsymbol{\sigma}$, may be divided into deviatoric and hydrostatic portions,

$$\boldsymbol{\sigma} = \boldsymbol{s} - p\boldsymbol{\delta} \tag{23}$$

where the components of the deviatoric stress tensor, $\boldsymbol{s}$, were previously defined in equation 9 as:

$$s_{ij} = \left[\sigma_{ij} - \frac{1}{3}\sigma_{kk}\delta_{ij}\right]$$

and the hydrostatic portion, or pressure, p, is defined as:

$$p = -\frac{1}{3}\left(\sigma_{xx} + \sigma_{yy} + \sigma_{zz}\right) = -\frac{1}{3}I_1 = -\frac{1}{3}trace(\boldsymbol{\sigma}) \tag{24}$$

The deviatoric stress tensor, $\boldsymbol{s}$, is associated with a change in shape, and the hydrostatic stress, or pressure, p, is associated with a change in volume.

The rate of the Cauchy stresses is also decomposed into deviatoric and hydrostatic parts by using deviatoric stress rates $\dot{\boldsymbol{s}}$ and pressure rate $\dot{\boldsymbol{p}} = -\frac{1}{3}trace(\dot{\boldsymbol{\sigma}})$ as:

$$\dot{\boldsymbol{\sigma}} = \dot{\boldsymbol{s}} - \dot{\boldsymbol{p}}\delta \tag{25}$$

As plastic deformations are nonlinear, and depend on the loading history, the constitutive equations are formulated in incremental form, in which strain rates are commonly split into elastic and plastic parts. This assumption is valid under small increments of plastic strain:

$$\begin{aligned} \dot{\varepsilon}_{ij} &= \dot{\varepsilon}_{ij}^{e} + \dot{\varepsilon}_{ij}^{p} \\ \dot{\boldsymbol{\varepsilon}} &= \dot{\boldsymbol{\varepsilon}}^{\boldsymbol{e}} + \dot{\boldsymbol{\varepsilon}}^{\boldsymbol{p}} \end{aligned} \tag{26}$$

Similarly, the strain rate tensor can be decomposed into deviatoric and volumetric parts by using deviatoric strain rate $\dot{\boldsymbol{e}}$, and volumetric strain rate, $\dot{\varepsilon}^{V} = trace(\dot{\boldsymbol{\varepsilon}})$**,** as:

$$\dot{\boldsymbol{\varepsilon}} = \dot{\boldsymbol{e}} + \frac{\dot{\varepsilon}^{V}}{3}\boldsymbol{\delta} \tag{27}$$

The plastic strain rate can be decomposed as:

$$\dot{\boldsymbol{\varepsilon}}_{\boldsymbol{p}} = \dot{\boldsymbol{e}}_{p} + \frac{\dot{\varepsilon}_{p}^{V}}{3}\boldsymbol{\delta} \tag{28}$$

where $\dot{\boldsymbol{e}}_{p}$ is the plastic deviatoric strain rate and $\dot{\varepsilon}_{p}^{V} = trace(\dot{\boldsymbol{\varepsilon}}_{\boldsymbol{p}})$ is the plastic volumetric strain rate. For metals, the plastic volumetric strain rate is zero, $\dot{\varepsilon}_{p}^{V} \equiv 0$.

The small-strain elasto-plastic isotropic material law can be written as:

$$\dot{\boldsymbol{\sigma}} = C_{ijkl}\left(\dot{\boldsymbol{\varepsilon}} - \dot{\boldsymbol{\varepsilon}}_{p}\right) \tag{29}$$

where C_{ijkl} is the fourth-order symmetric stiffness tensor. The material law can also be written with the deviatoric and hydrostatic parts separated:

$$\dot{\boldsymbol{\sigma}} = 2G\left(\dot{\boldsymbol{e}} - \dot{\boldsymbol{e}}_{p}\right) + K\left(\dot{\varepsilon}^{V} - \dot{\varepsilon}_{p}^{V}\right)\boldsymbol{\delta} \tag{30}$$

where $G = \frac{E}{2(1+\nu)}$ is the shear modulus, and $K = \frac{E}{3(1-2\nu)}$ is the bulk modulus. In equation 30, there are six equations with twelve unknowns: the six stress rates and the six plastic strain rates. Because the plastic volumetric strain rate is zero ($\dot{\varepsilon}_{p}^{V} \equiv 0$), and plastic strain rate is equal to its own derivative ($\dot{\boldsymbol{e}}_{p} = \dot{\boldsymbol{\varepsilon}}_{\boldsymbol{p}}$)**,** equation 30 may also be written as:

$$\dot{\boldsymbol{\sigma}} = \underbrace{2G\left(\dot{\boldsymbol{e}} - \dot{\boldsymbol{\varepsilon}}_{\boldsymbol{p}}\right)}_{\text{Deviatoric Part}} + K\dot{\varepsilon}^{V}\boldsymbol{\delta} \tag{31}$$

Therefore, the deviatoric stress rates can be written as:

$$\dot{\mathbf{s}} = 2G\left(\dot{\boldsymbol{e}} - \dot{\boldsymbol{\varepsilon}}_{\boldsymbol{p}}\right) \tag{32}$$

Let f be a yield function, then the yield criterion can be stated as:

$$f = \left(\sigma_{eff} - \sigma_{y}\right) < 0 \text{ : Elastic deformation} \tag{33}$$

$$f = \left(\sigma_{eff} - \sigma_{y}\right) = 0 \text{ : Plastic deformation} \tag{34}$$

The yield criterion shows that the initiation of plastic deformation occurs at the yield point. If loading continues, the plastic flow rule with a normality condition enables researchers to determine the direction of the plastic strain increment and its magnitude, which is determined by the plastic multiplier, λ. A flow rule obeying the normality condition is referred to as an associated flow rule. However, a flow rule in which the plastic strain increment is not normal to the yield surface is known as a non-associated flow rule. The non-associated flow rules have been used for geotechnical materials. For associated flow, the normality condition states that an increment in the plastic strain tensor is in a direction that is normal to the tangent to the yield surface at load point (i.e., the plastic flow potential coincides with the yield function). This can be written in terms of yield function f:

$$d\varepsilon_{ij}^{p} = d\lambda\frac{\partial f}{\partial \sigma_{ij}} \tag{35}$$

$$\dot{\boldsymbol{\varepsilon}}_{\boldsymbol{p}} = \dot{\lambda}\frac{\partial f}{\partial \boldsymbol{\sigma}} \tag{36}$$

where $\dot{\boldsymbol{\varepsilon}}_{p}$ is the plastic deviatoric strain rate, $\dot{\lambda}$ is the plastic multiplier rate, and $\boldsymbol{\sigma}$ is the Cauchy stress tensor.

In non-associated flow, the plastic potential is proposed as an equation:

$$g\left(\sigma_{ij}\right) = constant \tag{37}$$

which forms the surface of plastic potential in the stress space. Then the plastic strain increment is:

$$d\varepsilon_{ij}^{p} = d\lambda\frac{\partial g}{\partial \sigma_{ij}} \tag{38}$$

When the plastic potential is the same as the yield function, that is:

$$g\left(\sigma_{ij}\right) = f \tag{39}$$

which then reduces to equation 38. In this case, the plastic strain increment is normal to the yield surface. However, when the yield surface and the plastic potential are not equal, the plastic strain increment is normal to the surface of constant plastic potential but is not normal to the yield surface and, therefore, there is a non-associated flow rule.

There are three classes of materials: strain-hardening, perfectly-plastic, and strain-softening. Generally, metals are strain-hardening materials, and geotechnical materials may exhibit strain-softening under certain conditions. Several criteria have been proposed to classify materials. Generally, strain-hardening materials are regarded as stable materials by the well-known Drucker's postulate (Drucker, 1950).

In a multiaxial stress state, strain-hardening is considered in the form of hardening rules for subsequent yield surfaces. It has been experimentally observed that the yield surface, on application of a deformation history, may undergo expansion, distortion, translation, and rotation. In the literature, expansion of the initial yield surface is called isotropic hardening, and translation of the initial yield surface is called kinematic hardening. Whereas isotropic hardening assumes uniform expansion without translation of the yield surface in the stress space, kinematic hardening assumes translation without expansion of the yield surface in the stress space as plastic strain increases. In both strain-hardening models, the yield surface shape remains unchanged during strain-hardening, as shown in figure 15. Isotropic hardening is the most widely used strain-hardening concept, and kinematic hardening, either alone or in combination with isotropic hardening, is often introduced in material models where cyclic loadings are considered.

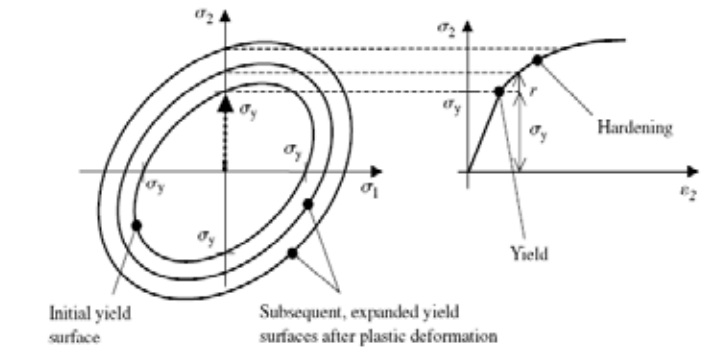

(a)

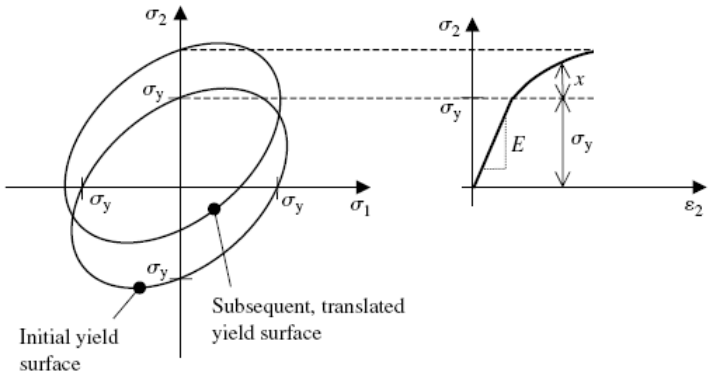

(b)

Figure 15. (a) Isotropic hardening, and (b) kinematic hardening in plane stress yield loci (Dunne & Petrinic, 2005)

Based on experimental observations of cyclical loading, subsequent yield surfaces may distort because of the stress state dependency in the hardening behavior of the material. This means that hardening curves regarding tension, compression, and shear stress states can be different (see figure 16).

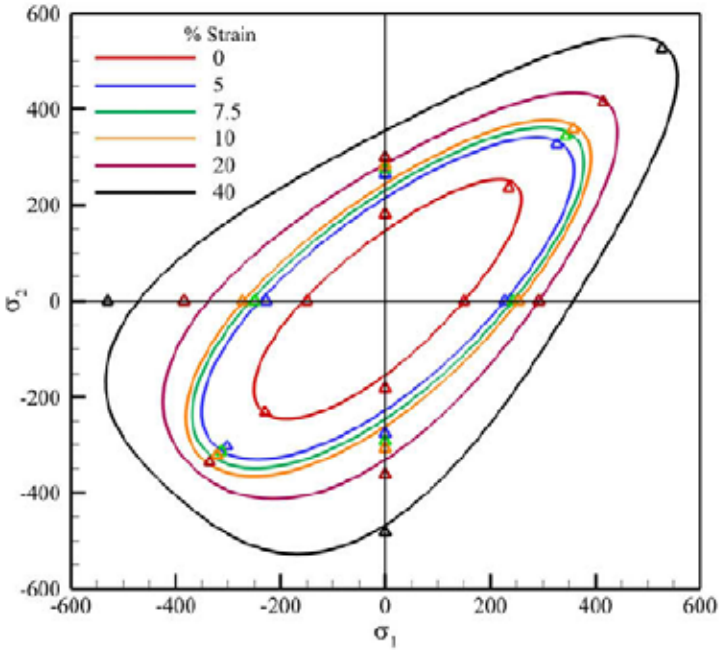

Figure 16. Hardening response of pure titanium according to theoretical yield surface and experimental data (symbols) corresponding to fixed values of the equivalent plastic strain after (Nixon, et al., 2010) (stresses are in MPa)

The loading-unloading conditions (also known as the Kuhn-Tucker (Kuhn & Tucker, 1951) conditions) are given as follows:

$$\dot{\lambda} \geq 0, f \leq 0, \dot{\lambda} f = 0 \tag{40}$$

where the first expression states that the plastic multiplier rate is always positive or zero, the second expression states that the stress is always on or within the yield surface, and the last expression states that the stresses remain on the yield surface during plastic loading (i.e., when $\dot{\lambda} > 0$). This last condition can also be stated as:

$$\dot{f} = 0 \tag{41}$$

Because f is equal to zero during the plastic flow, this equation is known as the consistency condition, and it enables researchers to determine the plastic multiplier. The yield function f is dependent on the components of the stress tensor and the yield stress of a material. When strain-hardening is considered, the yield stress of the material can increase as a function of equivalent plastic strain for subsequent loading. Therefore, the yield function can be written as:

$$f\left(\sigma_{ij}, \sigma_y\left(\bar{\varepsilon}_p\right)\right) \tag{42}$$

For an incremental change in the stress tensor (σ_{ij}) and equivalent plastic strain ($\bar{\varepsilon}_p$), the consistency condition results in:

$$\dot{f} = \frac{\partial f}{\partial \sigma_{ij}} : d\sigma_{ij} + \frac{\partial f}{\partial \bar{\varepsilon}_p} d\bar{\varepsilon}_p = 0 \tag{43}$$

$$d\sigma_{ij} = \boldsymbol{C} d\varepsilon_{ij}^{e} = \boldsymbol{C}\,(d\varepsilon_{ij} - d\varepsilon_{ij}^{p}) = \boldsymbol{C}\,(d\varepsilon_{ij} - d\lambda \frac{\partial f}{\partial \sigma_{ij}}) \tag{44}$$

$$\dot{f} = \frac{\partial f}{\partial \sigma_{ij}} : \boldsymbol{C}\,(d\varepsilon_{ij} - d\varepsilon_{ij}^{p}) + \frac{\partial f}{\partial \bar{\varepsilon}_p} d\bar{\varepsilon}_p = 0 \tag{45}$$

where $\boldsymbol{C}$ is the fourth-order symmetric stiffness tensor, previously referred to in tensor notation as C_{ijkl}.

3.2 Development of Proposed GYS Plasticity Model Using Stress Invariants $\boldsymbol{J_2}$ and $\boldsymbol{J_3}$

Material laws for the plastic behavior of isotropic materials can be formulated as a function of the three stress invariants (I_1, J_2, J_3): pressure ($p = -I_1/3$), von Mises stress (σ_{vm}), and the Lode parameter ($27J_3/2\sigma_{vm}^3$). Isotropic generalized plasticity models introduce J_3 dependency, in addition to J_2, to fully capture the plastic stress-strain fields. HCP metals, especially, show a strong SD effect (tension-compression asymmetry) in plastic flow, and the yield surface cannot be described by the von Mises plasticity. The main reason for the SD effect is the twinning deformation mechanism, which results in tensile-compressive asymmetry, and requires a yield surface with an odd power of J_3 to cover the SD effect.

Volumetric deformation of metals is elastic and linear in the normal engineering range (up to pressures of roughly 10 GPa). Material laws for metals are independent of the pressure, as the plastic deformation of metals occurs at constant volume (Hill, 1950b). Therefore, an assumption of a yield function depending on the von Mises stress and the Lode parameter, without dependence on pressure or the first invariant of the stress tensor, is valid when considering metals (Bridgman, 1952). A GYS can be obtained by multiplying the von Mises stress by a function of the Lode angle or Lode parameter:

$$\sigma_{eff} = \sigma_{vm}\, h(J_3, \sigma_{vm}) \leq \sigma_y \tag{46}$$

The von Mises stress, previously defined in equation 10, can also be written as:

$$\sigma_{vm} = \sqrt{3J_2}$$
$$\sigma_{vm} = \sqrt{\frac{3}{2}\boldsymbol{s}:\boldsymbol{s}} = \sqrt{\frac{3}{2}\left(s_{xx}^2 + s_{yy}^2 + s_{zz}^2 + 2s_{xy}^2 + 2s_{yz}^2 + 2s_{zx}^2\right)} \tag{47}$$

The Lode angle is defined as ϑ, and $cos3\vartheta$ is the Lode parameter, which is limited to an interval between -1 and 1:

$$cos3\vartheta = \frac{27J_3}{2\sigma_{vm}^3}$$
$$0 \leq \vartheta \leq \frac{\pi}{3} \rightarrow -1 \leq cos3\vartheta \leq +1 \quad (48)$$

The Lode angle is related to the third deviatoric stress invariant, J_3, using the Lode parameter. The third deviatoric stress invariant was previously defined in equation 3 as:

$$J_3 = \frac{1}{2} s_{ij}s_{jk}s_{ki} = s_1s_2s_30$$

Representation of the Lode angle (ϑ) and the corresponding Lode parameter for uni-axial tension, uni-axial compression, and pure-shear stress states are shown in the deviatoric plane in figure 17 (a). Comparison of Tresca, von Mises, and GYS yield surface models are presented in the deviatoric plane in figure 17 (b), and the effect of the tension-compression yielding asymmetry on GYS is shown in figure 17 (c). All stress states or loading conditions can be characterized by the Lode parameter $\left(cos3\vartheta = \frac{27J_3}{2\sigma_{vm}^3}\right)$ and the stress tri-axiality parameter $\left(\frac{p}{\sigma_{vm}}\right)$, which give the ratio of pressure to von Mises stress. Various stress states encountered in test specimens used for plasticity and fracture testing can be uniquely characterized by these two parameters.

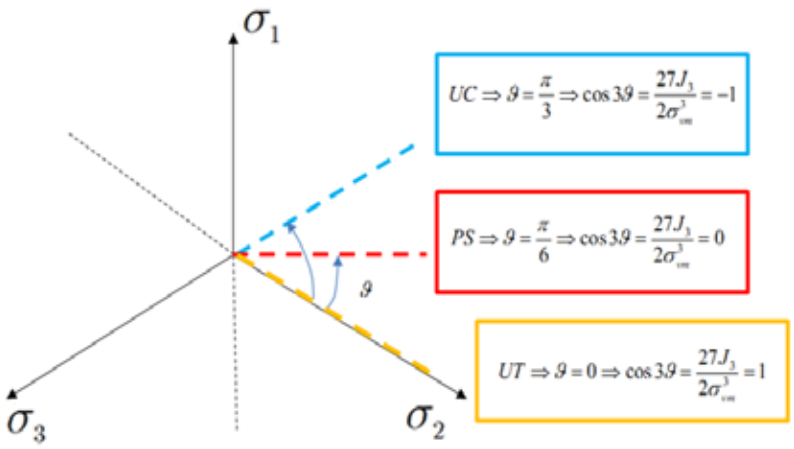

(a)

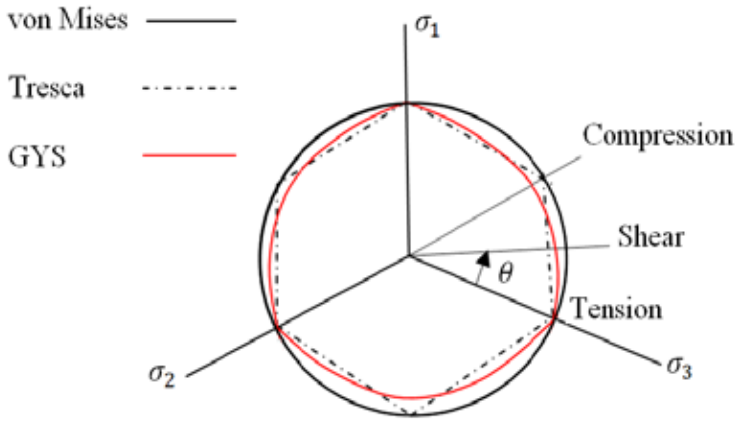

(b)

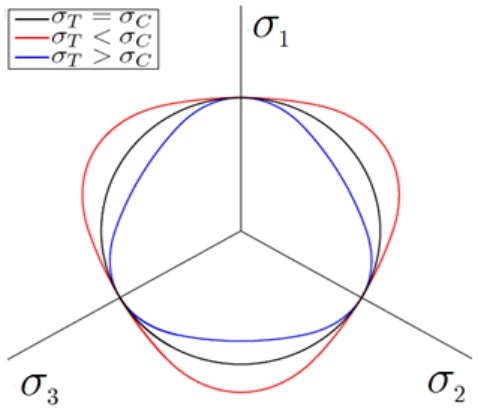

(c)

Figure 17. (a) Representation of Lode parameter and uniaxial tension, uniaxial compression, and pure-shear stress states; (b) comparison of yield surface models in deviatoric plane (π–plane); and (c) effect of tension (σ^T) vs compression (σ^C) yielding asymmetry on the GYS in deviatoric plane

A new GYS is proposed for pressure-insensitive metal plasticity using the following assumptions, conditions, and features:

- Yield stress, $\sigma_y(\bar{\varepsilon}^p_{eff}, \dot{\bar{\varepsilon}}^p_{eff}, T)$, is dependent on the effective plastic strain $\bar{\varepsilon}^p_{eff}$ (accumulated plastic strain), effective plastic strain rate $\dot{\bar{\varepsilon}}^p_{eff}$, and current temperature T.
- Only isotropic behavior is considered (no anisotropic effects). Isotropic hardening is assumed.
- Isochoric plasticity is assumed (constant volume during plastic deformation).
- Associated flow is assumed because it has been experimentally validated for metals. Therefore, the yield potential is equal to yield function.
- Unique flow (strain rate) for any given state of stress on the yield surface is assumed.
- The yield surface can describe yield surfaces lying between Tresca and von Mises yield surfaces.
- Tension-compression asymmetry is allowed.
- A multiplicative decomposition is assumed using the J_2 and J_3 invariants in the generalized yield function.

$$f(\sigma_{vm})g\left(\frac{p}{\sigma_{vm}}\right)h(cos3\vartheta, cos^2 3\vartheta) - \sigma_y \tag{49}$$

- Any dependency on pressure or first stress invariant is excluded; therefore, generalized yield function is in the form of:

$$f(\sigma_{vm})h(cos3\vartheta, cos^2 3\vartheta) - \sigma_y \tag{50}$$

  which represents pressure independent flow, considering that the $g\left(\frac{p}{\sigma_{vm}}\right)$ term is not included in the GYS yield function.

Considering the aforementioned assumptions, the following isotropic generalized yield function formulation is proposed:

$$f(\sigma_{eff}, \sigma_y(\bar{\varepsilon}^p_{eff}, \dot{\bar{\varepsilon}}^p_{eff}, T)) = \sigma_{vm}\left[c_1 + c_2\frac{27J_3}{2\sigma^3_{vm}} + c_3\frac{729J_3^2}{4\sigma^6_{vm}}\right] - \sigma_y(\bar{\varepsilon}^p_{eff}, \dot{\bar{\varepsilon}}^p_{eff}, T) \leq 0 \tag{51}$$

where σ_{eff} is the effective stress of the GYS model in terms of von Mises stress (equation 10) and J_3 (equation 3). The coefficients c_1, c_2, and c_3 are material dependent and vary with hardening. The effective stress, σ_{eff}, is defined as:

$$\sigma_{eff} = \sigma_{vm}\left[c_1 + c_2\frac{27J_3}{2\sigma^3_{vm}} + c_3\frac{729J_3^2}{4\sigma^6_{vm}}\right] \tag{52}$$

The matrix norm of the plastic strain rate, $\left\|\dot{\bar{\varepsilon}}_p\right\|$, is:

$$\left\|\dot{\bar{\varepsilon}}_p\right\|, = \sqrt{\frac{2}{3}\dot{\boldsymbol{\varepsilon}}_{\boldsymbol{p}} : \dot{\boldsymbol{\varepsilon}}_{\boldsymbol{p}}} = \dot{\lambda}\sqrt{\frac{2}{3}\frac{\partial \sigma_{eff}}{\partial \boldsymbol{\sigma}} : \frac{\partial \sigma_{eff}}{\partial \boldsymbol{\sigma}}}$$
$$\left\|\dot{\bar{\varepsilon}}_p\right\|, = \sqrt{\frac{2}{3}\left(\left(\dot{\varepsilon}^p_{xx}\right)^2 + \left(\dot{\varepsilon}^p_{yy}\right)^2 + \left(\dot{\varepsilon}^p_{zz}\right)^2 + 2\left(\dot{\varepsilon}^p_{xy}\right)^2 + 2\left(\dot{\varepsilon}^p_{yz}\right)^2 + 2\left(\dot{\varepsilon}^p_{zx}\right)^2\right)} \quad (53)$$

yield function in equation 51 is written differently than most existing plasticity models. In existing models, the yield function is typically written with the effective stress as a function of the stress tensor, and the yield stress as a function of the plastic multiplier. The effective stress defined in equation 52 is not only a function of the stress tensor, but also a function of the plastic multiplier.

The generalized yield function can also be written in terms of the von Mises stress parameter $f(\sigma_{vm})$ and Lode parameter, $cos3\vartheta$, as shown in equation 54:

$$f(\sigma_{eff}, \sigma_y(\bar{\varepsilon}^p_{eff}, \dot{\bar{\varepsilon}}^p_{eff}, T)) = \sigma_{vm}[c_1 + c_2 cos3\vartheta + c_3 cos^2 3\vartheta] - \sigma_y(\bar{\varepsilon}^p_{eff}, \dot{\bar{\varepsilon}}^p_{eff}, T) \leq 0 \quad (54)$$

where ϑ is the Lode angle, and the relation between the Lode angle and J_3 was given in equation 48. Then the definition of effective stress for the GYS model can also be written in terms of the Lode parameter:

$$\sigma_{eff} = \sigma_{vm}[c_1 + c_2 cos3\vartheta + c_3 cos^2 3\vartheta] \quad (55)$$

The four material coefficients, or hardening parameters, c_1, c_2, c_3 and σ_y, depend only on the plastic multiplier, λ. Equation 54 is rewritten to show only this dependency:

$$f = \sigma_{vm}[c_1(\lambda) + c_2(\lambda) cos3\vartheta + c_3(\lambda) cos^2 3\vartheta] - \sigma_y(\lambda) \leq 0 \quad (56)$$

The evolution laws for the material coefficients are:

$$\dot{c}_i = \dot{\bar{\varepsilon}}^p_{eff}\frac{\partial c_i}{\partial \bar{\varepsilon}^p_{eff}} = \dot{\lambda}\frac{\partial c_i}{\partial \lambda}\ i = 1,2,3\ \dot{\sigma}_y = \dot{\bar{\varepsilon}}^p_{eff}\frac{\partial \sigma_y}{\partial \bar{\varepsilon}^p_{eff}} = \dot{\lambda}\frac{\partial \sigma_y}{\partial \lambda} \quad (57)$$

An implication of allowing the hardening parameters to evolve is that the yield function cannot only expand; it can also deform. As a result, the hardening in GYS is distortional and not self-similar, as is common.

The condition $f(\sigma_{eff}, \sigma_y(\bar{\varepsilon}^p_{eff}, \dot{\bar{\varepsilon}}^p_{eff}, T)) = 0$ is the yield criterion in the multi-dimensional case. When the stress state is inside the surface ($f(\sigma_{eff}, \sigma_y(\bar{\varepsilon}^p_{eff}, \dot{\bar{\varepsilon}}^p_{eff}, T)) < 0$), then the current stress state is elastic, and the material deforms elastically. When the stress state is on the surface ($f(\sigma_{eff}, \sigma_y(\bar{\varepsilon}^p_{eff}, \dot{\bar{\varepsilon}}^p_{eff}, T)) = 0$), then the stress state becomes plastic and the material deforms plastically.

3.3 Associated Flow and the Hardening Rule in the GYS Plasticity Model

3.3.1 The Hardening Rule and the Plastic Multiplier

Associated flow is assumed in the GYS model, which is a common assumption in the modeling of metals. Associated flow can be interpreted as the direction of the increment in the plastic strain tensor being normal to the yield surface at the load point. As discussed in section 3.1, in associated flow, the flow potential (*g*) is equal to the yield function *(f*). Because the plastic strain rate tensor was previously defined in equation 27 as:

$$\dot{\boldsymbol{\varepsilon}}_{\boldsymbol{p}} = \dot{\lambda}\frac{\partial f}{\partial \boldsymbol{\sigma}}$$

then the plastic strain rate tensor is:

$$\dot{\boldsymbol{\varepsilon}}_{\boldsymbol{p}} = \dot{\lambda}\frac{\partial f}{\partial \boldsymbol{\sigma}} = \dot{\lambda}\frac{\partial \sigma_{eff}}{\partial \boldsymbol{\sigma}} \tag{58}$$

Rewriting equation 58 using the chain rule yields:

$$\dot{\boldsymbol{\varepsilon}}_{\boldsymbol{p}} = \dot{\lambda}\left[\frac{\partial \sigma_{eff}}{\partial \sigma_{vm}}\frac{\partial \sigma_{vm}}{\partial \boldsymbol{\sigma}} + \frac{\partial \sigma_{eff}}{\partial J_3}\frac{\partial J_3}{\partial \boldsymbol{\sigma}}\right] \tag{59}$$

and using the following relationships:

$$\frac{\partial \sigma_{vm}}{\partial \boldsymbol{\sigma}} = \frac{3\boldsymbol{s}}{2\sigma_{vm}} \tag{60}$$

$$\frac{\partial J_3}{\partial \boldsymbol{s}} = \frac{\partial det(\boldsymbol{s})}{\partial \boldsymbol{s}} = det(\boldsymbol{s})\boldsymbol{s}^{-T} = J_3\boldsymbol{s}^{-T} = J_3\boldsymbol{s}^{-1} \tag{61}$$

$$\frac{\partial J_3}{\partial \boldsymbol{\sigma}} = \frac{\partial J_3}{\partial \boldsymbol{s}} - \frac{1}{3}tr\left(\frac{\partial J_3}{\partial \boldsymbol{s}}\right)\boldsymbol{\delta} = J_3\boldsymbol{s}^{-1} - \frac{1}{3}tr\left(\frac{\partial J_3}{\partial \boldsymbol{s}}\right)\boldsymbol{\delta} \tag{62}$$

equation 59 becomes:

$$\dot{\boldsymbol{\varepsilon}}_{\boldsymbol{p}} = \dot{\lambda}\left[\frac{\partial \sigma_{eff}}{\partial \sigma_{vm}}\frac{3\boldsymbol{s}}{2\sigma_{vm}} + \frac{\partial \sigma_{eff}}{\partial J_3}\left(J_3\boldsymbol{s}^{-1} - J_3\frac{1}{3}tr(\boldsymbol{s}^{-1})\boldsymbol{\delta}\right)\right] \tag{63}$$

Taking derivatives of GYS effective stress, as previously given by equation 52:

$$\sigma_{eff} = \sigma_{vm}\left[c_1 + c_2\frac{27J_3}{2\sigma_{vm}^3} + c_3\frac{729J_3^2}{4\sigma_{vm}^6}\right]$$

results in:

$$\frac{\partial \sigma_{eff}}{\partial \sigma_{vm}} = \left[c_1 - 2c_2\frac{27J_3}{2\sigma_{vm}^3} - 5c_3\frac{729J_3^2}{4\sigma_{vm}^6}\right] \tag{64}$$

and:

$$\frac{\partial \sigma_{eff}}{\partial J_3} = \sigma_{vm}\left[c_2\frac{27}{2\sigma_{vm}^3} - 2c_3\frac{729J_3}{4\sigma_{vm}^6}\right] \tag{65}$$

The plastic strain rate tensor can then be written as:

$$\dot{\boldsymbol{\varepsilon}}_{\boldsymbol{p}} = \dot{\lambda}\left[\left(c_1 - 2c_2\frac{27J_3}{2\sigma_{vm}^3} - 5c_3\frac{729J_3^2}{4\sigma_{vm}^6}\right)\frac{3\boldsymbol{s}}{2\sigma_{vm}} + \sigma_{vm}\left(c_2\frac{27}{2\sigma_{vm}^3} + 2c_3\frac{729J_3}{4\sigma_{vm}^6}\right)\left(J_3\boldsymbol{s}^{-1} - J_3\frac{1}{3}tr(\boldsymbol{s}^{-1})\boldsymbol{\delta}\right)\right] \tag{66}$$

or rewriting slightly:

$$\dot{\boldsymbol{\varepsilon}}_{\boldsymbol{p}} = \dot{\lambda}\left[\left(c_1 - 2c_2\frac{27J_3}{2\sigma_{vm}^3} - 5c_3\frac{729J_3^2}{4\sigma_{vm}^6}\right)\frac{3\boldsymbol{s}}{2\sigma_{vm}} + \left(c_2\frac{27J_3}{2\sigma_{vm}^3} + 2c_3\frac{729J_3^2}{4\sigma_{vm}^6}\right)\sigma_{vm}\left(\boldsymbol{s}^{-1} - \frac{1}{3}tr(\boldsymbol{s}^{-1})\boldsymbol{\delta}\right)\right] \tag{67}$$

Combing equation (58) ($\dot{\boldsymbol{\varepsilon}}_{\boldsymbol{p}} = \dot{\lambda}\frac{\partial\sigma_{eff}}{\partial\boldsymbol{\sigma}}$) with equation 67 yields:

$$\frac{\partial\sigma_{eff}}{\partial\boldsymbol{\sigma}} = \left[\left(c_1 - 2c_2\frac{27J_3}{2\sigma_{vm}^3} - 5c_3\frac{729J_3^2}{4\sigma_{vm}^6}\right)\frac{3\boldsymbol{s}}{2\sigma_{vm}} + \left(c_2\frac{27J_3}{2\sigma_{vm}^3} + 2c_3\frac{729J_3^2}{4\sigma_{vm}^6}\right)\sigma_{vm}\left(\boldsymbol{s}^{-1} - \frac{1}{3}tr(\boldsymbol{s}^{-1})\boldsymbol{\delta}\right)\right] \tag{68}$$

The effective plastic strain rate is defined as the energy conjugate to the effective stress. Therefore, the plastic work rate can be written as:

$$\dot{W}_p = \dot{\boldsymbol{\varepsilon}}_{\boldsymbol{p}} : \boldsymbol{\sigma} = \dot{\boldsymbol{\varepsilon}}_{\boldsymbol{p}} : \boldsymbol{s} = \dot{\bar{\varepsilon}}_{eff}^{p}\sigma_{eff} = \dot{\lambda}\frac{\partial\sigma_{eff}}{\partial\boldsymbol{\sigma}} : \boldsymbol{\sigma} = \dot{\lambda}\frac{\partial\sigma_{eff}}{\partial\boldsymbol{\sigma}} : \boldsymbol{s} \tag{69}$$

as it follows from equation 68 that the derivative of the effective stress with respect to the stress tensor is deviatoric in nature. Then, the effective plastic strain rate is:

$$\dot{\bar{\varepsilon}}_{eff}^{p} = \frac{1}{\sigma_{eff}}\dot{\lambda}\frac{\partial\sigma_{eff}}{\partial\boldsymbol{\sigma}} : \boldsymbol{s} \tag{70}$$

By using equation 68, the effective plastic strain rate of equation 70 becomes:

$$\dot{\bar{\varepsilon}}_{eff}^{p} = \frac{1}{\sigma_{eff}}\dot{\lambda}\left[\left(c_1 - 2c_2\frac{27J_3}{2\sigma_{vm}^3} - 5c_3\frac{729J_3^2}{4\sigma_{vm}^6}\right)\frac{3\boldsymbol{s}}{2\sigma_{vm}} + \left(c_2\frac{27J_3}{2\sigma_{vm}^3} + 2c_3\frac{729J_3^2}{4\sigma_{vm}^6}\right)\sigma_{vm}\left(\boldsymbol{s}^{-1} - \frac{1}{3}tr(\boldsymbol{s}^{-1})\boldsymbol{\delta}\right)\right] : \boldsymbol{s} \tag{71}$$

And using the following relationships:

$$\boldsymbol{s} : \boldsymbol{s} = \frac{2\sigma_{vm}^2}{3} \tag{72}$$

$$\boldsymbol{s} : \boldsymbol{s}^{-1} = \boldsymbol{s}^{-1} : \boldsymbol{s} = tr(\boldsymbol{\delta}) = 3 \tag{73}$$

$$\boldsymbol{s} = \boldsymbol{\sigma} + p\boldsymbol{\delta}, \boldsymbol{\delta} : \boldsymbol{s} = \boldsymbol{0}\ (\boldsymbol{\delta}; kronecker\ delta), \tag{74}$$

The effective plastic strain rate, equation 71, can now be written as:

$$\dot{\bar{\varepsilon}}_{eff}^{p} = \dot{\lambda}\frac{\sigma_{vm}}{\sigma_{eff}}\left[\left(c_1 - 2c_2\frac{27J_3}{2\sigma_{vm}^3} - 5c_3\frac{729J_3^2}{4\sigma_{vm}^6}\right) + \left(3c_2\frac{27J_3}{2\sigma_{vm}^3} + 6c_3\frac{729J_3^2}{4\sigma_{vm}^6}\right)\right] \tag{75}$$

And simplifying further:

$$\dot{\bar{\varepsilon}}^p_{eff} = \dot{\lambda}\frac{\sigma_{vm}}{\sigma_{eff}}\left[\left(c_1 + c_2\frac{27J_3}{2\sigma^3_{vm}} + c_3\frac{729J_3^2}{4\sigma^6_{vm}}\right)\right] = \dot{\lambda}\frac{\sigma_{vm}}{\sigma_{eff}}\left[\frac{\sigma_{eff}}{\sigma_{vm}}\right] = \dot{\lambda} \tag{76}$$

This result shows that the effective plastic strain rate is equal to the rate of the plastic multiplier in the GYS model. The hardening rule of the GYS model can now be written as:

$$\dot{\sigma}_y = \dot{\lambda}\frac{\partial\sigma_y}{\partial\lambda} = \dot{\bar{\varepsilon}}^p_{eff}\frac{\partial\sigma_y}{\partial\bar{\varepsilon}^p_{eff}} \tag{77}$$

Rewriting equation 69, an increment in the effective plastic strain is equal to an increment in the plastic multiplier:

$$\dot{W}_p = \dot{\bar{\varepsilon}}^p_{eff}\sigma_{eff} = \dot{\lambda}\,\sigma_{eff} \Rightarrow \Delta W_p = \Delta\lambda\sigma_{eff} \tag{78}$$

Equation 78 shows that the increment in yield stress can be directly interpolated from a yield stress versus equivalent plastic strain input curve. This is a result of the plastic multiplier ($\Delta\lambda$) increment being equivalent to the GYS effective plastic strain increment.

Equation 78 can also be derived in a more general way by observing that the expression for the effective stress, equation 52, is a polynomial of order one. In this case, Euler's theorem can be used and written as:

$$\frac{\partial\sigma_{eff}}{\partial\boldsymbol{\sigma}} : \boldsymbol{\sigma} = \sigma_{eff} \tag{79}$$

Therefore:

$$\dot{W}_p = \dot{\boldsymbol{\varepsilon}}_{\boldsymbol{p}} : \boldsymbol{\sigma} = \dot{\lambda}\frac{\partial\sigma_{eff}}{\partial\boldsymbol{\sigma}} : \boldsymbol{\sigma} = \dot{\lambda}\sigma_{eff} \tag{80}$$

showing that the rate of the plastic multiplier is the energy conjugate to the plastic work and, consequently, by definition, equal to the equivalent plastic strain rate.

3.3.2 Plastic Incompressibility

It must be proven that plastic incompressibility is a feature of the GYS model. For plastic incompressibility to exist, the following must be true:

$$\frac{\partial f}{\partial\sigma_{xx}} + \frac{\partial f}{\partial\sigma_{yy}} + \frac{\partial f}{\partial\sigma_{zz}} \equiv 0 \tag{81}$$

The volumetric plastic strain rate, $\dot{\varepsilon}^p_{vol}$, is defined as the trace of the plastic strain rate tensor:

$$\dot{\varepsilon}^p_{vol} = trace(\dot{\boldsymbol{\varepsilon}}_{\boldsymbol{p}}) \tag{82}$$

Recalling that the plastic strain tensor is defined in equation 67 as:

$$\dot{\boldsymbol{\varepsilon}}_{\boldsymbol{p}} = \dot{\lambda}\left[\left(c_1 - 2c_2\frac{27J_3}{2\sigma_{vm}^3} - 5c_3\frac{729J_3^2}{4\sigma_{vm}^6}\right)\frac{3\boldsymbol{s}}{2\sigma_{vm}} + \left(c_2\frac{27J_3}{2\sigma_{vm}^3} + 2c_3\frac{729J_3^2}{4\sigma_{vm}^6}\right)\sigma_{vm}\left(\boldsymbol{s}^{-1} - \frac{1}{3}tr(\boldsymbol{s}^{-1})\boldsymbol{\delta}\right)\right]$$

Therefore, the volumetric plastic strain is:

$$\dot{\varepsilon}_{vol}^{p} = \dot{\lambda}\left[\left(c_1 - 2c_2\frac{27J_3}{2\sigma_{vm}^3} - 5c_3\frac{729J_3^2}{4\sigma_{vm}^6}\right)\frac{3tr(\boldsymbol{s})}{2\sigma_{vm}} + \left(c_2\frac{27J_3}{2\sigma_{vm}^3} + 2c_3\frac{729J_3^2}{4\sigma_{vm}^6}\right)\sigma_{vm}tr\left(\boldsymbol{s}^{-1} - \frac{1}{3}tr(\boldsymbol{s}^{-1})\boldsymbol{\delta}\right)\right] \quad (83)$$

The trace of the deviatoric stress tensor is zero:

$$tr(\boldsymbol{s}) \equiv 0 \quad (84)$$

and:

$$\boldsymbol{s}^{-1} - \frac{1}{3}tr(\boldsymbol{s}^{-1})\boldsymbol{\delta} = \frac{1}{3}\begin{pmatrix} 2s_{11}^{-1} - s_{22}^{-1} - s_{33}^{-1} & 3s_{21}^{-1} & 3s_{13}^{-1} \\ 3s_{12}^{-1} & -s_{11}^{-1} + 2s_{22}^{-1} - s_{33}^{-1} & 3s_{23}^{-1} \\ 3s_{31}^{-1} & 3s_{32}^{-1} & -s_{11}^{-1} - s_{22}^{-1} + 2s_{33}^{-1} \end{pmatrix} \quad (85)$$

Therefore, the trace of equation 85 is also zero:

$$tr\left(\boldsymbol{s}^{-1} - \frac{1}{3}tr(\boldsymbol{s}^{-1})\boldsymbol{\delta}\right) = 0 \quad (86)$$

Therefore, the trace of the plastic strain tensor is zero:

$$tr\left(\dot{\boldsymbol{\varepsilon}}_{\boldsymbol{p}}\right) = 0 \quad (87)$$

and the volumetric plastic strain produced by the GYS flow rule is exactly zero. Therefore, equation 81 is shown to be true, demonstrating plastic incompressibility and isochoric response.

3.4 The Material Coefficients and Examples of Specific Stress States

3.4.1 Uni-Axial Tension

Consider the case of uni-axial tension, in which by definition of equation 48, the Lode parameter, $cos3\vartheta = \frac{27J_3}{2\sigma_{vm}^3} = 1$, and therefore also, $cos^2 3\vartheta = \frac{729J_3^2}{4\sigma_{vm}^6} = 1$. In this case of uniaxial tension, the GYS function (equation 55) in the plastic state ($f(\sigma_{eff}, \sigma_y(\bar{\varepsilon}_{eff}^{p}, \dot{\bar{\varepsilon}}_{eff}^{p}, T)) = 0$) reduces to:

$$\sigma_{vm}[c_1 + c_2 + c_3] - \sigma_y = 0 \quad (88)$$

In uni-axial tension, the von Mises stress is equal to the longitudinal tensile stress ($\sigma_{vm} = \sigma_t$). In the GYS model, the choice has been made to set the yield parameter equal to the tensile stress ($\sigma_y = \sigma_t$). A normalization choice is required because, whereas there are four parameters in the yield function, there are only three degrees-of-freedom in the yield condition. Therefore, because $\sigma_y = \sigma_t$, the sum of coefficients c_1, c_2 and c_3 must be equal to 1:

$$\sigma_t(c_1 + c_2 + c_3) - \sigma_t = 0 \rightarrow c_1 + c_2 + c_3 = 1 \tag{89}$$

In uni-axial tension, because $cos3\vartheta = 1$, the GYS effective stress (equation 55) reduces to:

$$\sigma_{eff} = \sigma_{vm}[c_1 + c_2 + c_3] \tag{90}$$

Because in uni-axial tension $\sigma_{vm} = \sigma_t$, and because $c_1 + c_2 + c_3 = 1$, equation 90 becomes:

$$\sigma_{eff} = \sigma_t[c_1 + c_2 + c_3] = \sigma_t \tag{91}$$

Therefore, the GYS effective stress has been defined so that the effective stress is equal to the yield stress in uni-axial tension ($\sigma_{eff} = \sigma_t$). For consistency, the yield parameter must remain equal to yield stress in tension ($\sigma_y = \sigma_t$).

In uni-axial tension, σ_t is the stress in the tension load direction ($\sigma_{11} = \sigma_t$). Then the stress tensors are:

$$\boldsymbol{\sigma} = \begin{bmatrix} \sigma_t & 0 & 0 \\ 0 & 0 & 0 \\ 0 & 0 & 0 \end{bmatrix} \Rightarrow p = -\frac{\sigma_t}{3} \Rightarrow \boldsymbol{s} = \frac{\sigma_t}{3}\begin{bmatrix} 2 & 0 & 0 \\ 0 & -1 & 0 \\ 0 & 0 & -1 \end{bmatrix} \tag{92}$$

Then in uni-axial tension, the following relationships are also true:

$$\boldsymbol{s}^{-1} = \frac{3}{\sigma_t}\begin{bmatrix} 1/2 & 0 & 0 \\ 0 & -1 & 0 \\ 0 & 0 & -1 \end{bmatrix} \Rightarrow \frac{1}{3}tr(\boldsymbol{s}^{-1})\boldsymbol{\delta} = -\frac{3}{2\sigma_t}\begin{bmatrix} 1 & 0 & 0 \\ 0 & 1 & 0 \\ 0 & 0 & 1 \end{bmatrix} \tag{93}$$

$$\left(\frac{3\boldsymbol{s}}{2\sigma_{vm}}\right)_{11} = \frac{3}{2\sigma_t}\frac{2\sigma_t}{3} = 1, \; since \; \sigma_{vm} = \sigma_t \tag{94}$$

$$\sigma_{vm}\left(\boldsymbol{s}^{-1} - \left(\frac{1}{3}tr(\boldsymbol{s}^{-1})\boldsymbol{\delta}\right)\right)_{11} = \sigma_t\left(\frac{3}{2\sigma_t} + \frac{3}{2\sigma_t}\right) = 3 \tag{95}$$

Using equations 93, 94, and 95, equation 67 reduces to:

$$\dot{\varepsilon}_t^p = \dot{\lambda}\left[(c_1 - 2c_2 - 5c_3)\frac{\sigma_t}{\sigma_t} + (3c_2 + 6c_3)\frac{\sigma_t}{\sigma_t}\right] \tag{96}$$

Then the plastic strain rate in the tension load direction is $\dot{\varepsilon}_t^p$=$\dot{\varepsilon}_{11}^p$ and is given by:

$$\dot{\varepsilon}_t^p = \dot{\lambda}[(c_1 + c_2 + c_3)] = \dot{\lambda} \; since \; c_1 + c_2 + c_3 = 1 \tag{97}$$

The effective plastic strain rate is defined as the incremental energy conjugate to the effective stress, and using the results of equations 78 and 80, $\dot{W} = \dot{\bar{\varepsilon}}_{eff}^p\sigma_{eff} = \dot{\lambda}\sigma_{eff}$, and because $\dot{\lambda} = \dot{\varepsilon}_t^p$ the effective plastic strain rate, $\dot{\bar{\varepsilon}}_{eff}^p$, for uni-axial tension is:

$$\dot{W}_p = \dot{\boldsymbol{\varepsilon}}_{\boldsymbol{p}} : \boldsymbol{\sigma} = \dot{\bar{\varepsilon}}_{eff}^p\sigma_{eff} = \dot{\lambda}\sigma_t = \dot{\varepsilon}_t^p\sigma_t \rightarrow \dot{\bar{\varepsilon}}_{eff}^p = \dot{\varepsilon}_t^p \tag{98}$$

3.4.2 Uni-Axial Compression

Consider uni-axial compression in which the Lode parameter, $cos3\vartheta = \frac{27J_3}{2\sigma_{vm}^3} = -1$, and $cos^2 3\mathcal{J} = \frac{729J_3^2}{4\sigma_{vm}^6} = 1$. Then the GYS function (equation 53) takes the form:

$$\sigma_{vm}(c_1 - c_2 + c_3) = \sigma_y \rightarrow \sigma_c(c_1 - c_2 + c_3) = \sigma_t \rightarrow c_1 - c_2 + c_3 = \frac{\sigma_t}{\sigma_c} \tag{99}$$

because the von Mises stress is equal to the axial compressive stress ($\sigma_{vm} = \sigma_c$), and the yield parameter remains equal to the yield stress in tension ($\sigma_y = \sigma_t$). Equation 99 shows that tensile-compressive asymmetry determines c_2 or c_3 in the GYS function (in the next section, it will be shown that shear determines c_1). In uni-axial compression, because $cos3\vartheta = -1$, $cos^2 3\mathcal{J} = 1$, and $c_1 - c_2 + c_3 = \frac{\mathcal{S}_t}{\mathcal{S}_c}$, the effective stress (equation 55) is:

$$\sigma_{eff} = \sigma_{vm}[c_1 - c_2 + c_3] = \sigma_{vm}\frac{\sigma_t}{\sigma_c} \tag{100}$$

In the case of uni-axial compression, $-\sigma_C$ is the stress in the direction of the compression load ($\sigma_{33} = -\sigma_C$), and the stress tensor of the uni-axial compression case is:

$$\boldsymbol{\sigma} = \begin{bmatrix} 0 & 0 & 0 \\ 0 & 0 & 0 \\ 0 & 0 & -\sigma_c \end{bmatrix} \Rightarrow p = \frac{\sigma_c}{3} \Rightarrow \boldsymbol{s} = \frac{\sigma_c}{3}\begin{bmatrix} +1 & 0 & 0 \\ 0 & +1 & 0 \\ 0 & 0 & -2 \end{bmatrix} \tag{101}$$

Then in uni-axial compression, the following relationships are also true:

$$\boldsymbol{s}^{-1} = \frac{3}{\sigma_c}\begin{bmatrix} 1 & 0 & 0 \\ 0 & 1 & 0 \\ 0 & 0 & -1/2 \end{bmatrix} \Rightarrow \frac{1}{3}tr(\boldsymbol{s}^{-1})\boldsymbol{\delta} = \frac{3}{2\sigma_c}\begin{bmatrix} 1 & 0 & 0 \\ 0 & 1 & 0 \\ 0 & 0 & 1 \end{bmatrix} \tag{102}$$

$$\left(\frac{3\boldsymbol{s}}{2\sigma_{vm}}\right)_{33} = -\frac{3}{2\sigma_c}\frac{2\sigma_c}{3} = -1, \; since \; \sigma_{vm} = \sigma_c \tag{103}$$

$$\sigma_{vm}\left(\boldsymbol{s}^{-1} - \left(\frac{1}{3}tr(\boldsymbol{s}^{-1})\boldsymbol{\delta}\right)\right)_{33} = \sigma_c\left(-\frac{3}{2\sigma_c} - \frac{3}{2\sigma_c}\right) = -3 \tag{104}$$

Using the plastic strain rate tensor as defined in section 3.3.1 (equation 67), and equations 102, 103, and 104, the plastic strain rate in the direction of the compressive load is $\dot{\varepsilon}_c^p = -\dot{\varepsilon}_{33}^p$ and is given by:

$$\dot{\varepsilon}_{33}^p = -\dot{\varepsilon}_c^p = -\dot{\lambda}[(c_1 + 2c_2 - 5c_3)(-1) + (-c_2 + 2c_3)(-3)] \tag{105}$$

$$\dot{\varepsilon}_{33}^p = -\dot{\varepsilon}_c^p = -\dot{\lambda}[(-c_1 + c_2 - c_3)] \tag{106}$$

Therefore, using equation 99, the relation between the plastic consistency parameter increment and the compressive plastic strain increment can be written in rate form as:

$$\dot{\varepsilon}_c^p = \dot{\lambda}\frac{\sigma_t}{\sigma_c} \tag{107}$$

The effective plastic strain rate is defined as the incremental energy conjugate to the effective stress, and using the results of equations 78 and 80, $\dot{W} = \dot{\bar{\varepsilon}}_{eff}^p \sigma_{eff} = \dot{\lambda}\sigma_{eff}$, and because $\dot{\lambda} = \frac{\sigma_c}{\sigma_t}\dot{\varepsilon}_c^p$, the effective plastic strain rate, $\dot{\bar{\varepsilon}}_{eff}^p$, for uni-axial compression is:

$$\dot{W}_p = \dot{\boldsymbol{\varepsilon}}_{\boldsymbol{p}} : \boldsymbol{\sigma} = \dot{\bar{\varepsilon}}_{eff}^p \sigma_{eff} = \dot{\lambda}\sigma_c = \dot{\varepsilon}_c^p \sigma_c \rightarrow \dot{\bar{\varepsilon}}_{eff}^p = \dot{\varepsilon}_c^p \frac{\sigma_c}{\sigma_t} \tag{108}$$

3.4.3 Pure-Shear

Considering pure-shear in which the Lode parameter, $cos3\vartheta = \frac{27J_3}{2\sigma_{vm}^3} = 0$, the GYS function (equation 53) takes the form:

$$\sigma_{vm}c_1 - \sigma_y = 0 \rightarrow \sigma_s\sqrt{3}c_1 - \sigma_t = 0 \rightarrow c_1 = \frac{\sigma_t}{\sqrt{3}\sigma_s} \tag{109}$$

where $\sigma_{vm} = \sqrt{3}\sigma_s$ and $\sigma_y = \sigma_t$. Therefore, the yield in shear determines c_1, and it is independent of tensile-compressive asymmetry. (This is in contrast to the to the Cazacu-Barlat model, in which the shear yield relative to the tension yield is fixed by the tensile-compressive asymmetry.) Because in the case of pure-shear, $cos3\vartheta = 0$ and $\sigma_{vm} = \sqrt{3}\sigma_s$, the effective stress (equation 52) becomes:

$$\sigma_{eff} = \sigma_{vm}[c_1] = \sigma_{vm}\frac{\sigma_t}{\sqrt{3}\sigma_s} \tag{110}$$

In the case of pure-shear, $\sigma_{11} = -\sigma_{33} = \sigma_S$ where σ_S is plastic shear stress, then the pure-shear stress tensor is given by:

$$\boldsymbol{\sigma} = \begin{bmatrix} \sigma_s & 0 & 0 \\ 0 & 0 & 0 \\ 0 & 0 & -\sigma_s \end{bmatrix} \Rightarrow p = 0 \Rightarrow \boldsymbol{s} = \sigma_s \begin{bmatrix} +1 & 0 & 0 \\ 0 & 0 & 0 \\ 0 & 0 & -1 \end{bmatrix} \tag{111}$$

Because the J_3-related terms are zero in the plastic strain rate tensor, the plastic strain rate (equation 67) in pure-shear can be written as:

$$\dot{\varepsilon}_s^p = \dot{\lambda}c_1\frac{3\sigma_s}{2\sigma_{vm}} = \dot{\lambda}\, c_1\, \frac{3\sigma_s}{2\sigma_s\sqrt{3}} = \dot{\lambda}\, c_1\frac{\sqrt{3}}{2} \tag{112}$$

Considering the results of equation 109, $c_1 = \frac{\sigma_t}{\sqrt{3}\sigma_s}$, then the plastic shear strain rate is:

$$\dot{\varepsilon}_s^p = \dot{\lambda}\frac{\sigma_t}{\sigma_s\sqrt{3}}\frac{\sqrt{3}}{2} = \dot{\lambda}\, \frac{\sigma_t}{2\sigma_s} \tag{113}$$

Then the engineering plastic shear strain rate is given by:

$$\dot{\gamma}_s^p = 2\dot{\varepsilon}_s^p = \dot{\lambda}\frac{\sigma_t}{\sigma_s} \tag{114}$$

$$\dot{W}_p = \dot{\boldsymbol{\varepsilon}}_{\boldsymbol{p}} : \boldsymbol{\sigma} = \dot{\bar{\varepsilon}}_{eff}^p \sigma_{eff} = \dot{\lambda}\sigma_s = \dot{\gamma}_s^p \sigma_s \rightarrow \dot{\bar{\varepsilon}}_{eff}^p = \dot{\gamma}_s^p \frac{\sigma_s}{\sigma_t} \tag{115}$$

3.4.4 The Distortional Hardening Parameters

In summary, the four material coefficients and hardening parameters of the GYS yield function (equation 54), c_1, c_2, c_3, and σ_y, are as follows:

$$\begin{gathered} \sigma_{vm} = \sigma_y = \sigma_t \\ c_1 + c_2 + c_3 = 1, c_1 - c_2 + c_3 = \frac{\sigma_t}{\sigma_c},\ c_1 = \frac{\sigma_t}{\sqrt{3}\sigma_s} \end{gathered} \tag{116}$$

One of these four coefficients must be used to normalize the yield function, $f(\sigma_{eff}, \sigma_y(\bar{\varepsilon}_{eff}^p, \dot{\bar{\varepsilon}}_{eff}^p, T))$ (also referred to simply as f). Specifically, in GYS the choice has been made to make the yield stress coincide with the tensile yield stress $\sigma_y = \sigma_t$, as shown in equation 116.

Because of the normalization, three experiments—uni-axial tension, uni-axial compression, and torsion (pure-shear)—are necessary to determine the material coefficients, or hardening parameters, as shown in figure 18. The yield surface is derived from the material coefficients.

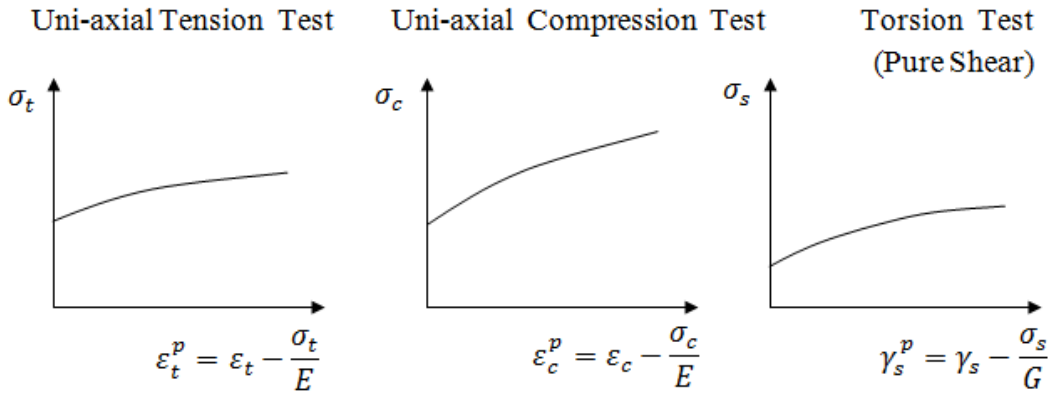

Figure 18. Uni-axial tension, uni-axial compression, and pure-shear (torsion) tests required by GYS to determine model coefficients c_1, c_2, c_3, and σ_y

Four curves are used to define the four material-dependent hardening coefficients in terms of the effective plastic strain parameter $\bar{\varepsilon}_{eff}^p$ of the GYS yield function, as shown in figure 19. Note that the increment in $\bar{\varepsilon}_{eff}^p$ is equivalent to the increment in plasticity multiplier, λ.

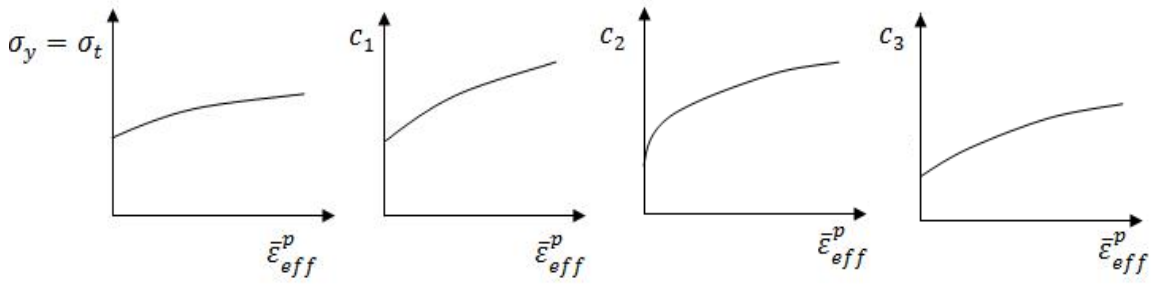

Figure 19. Four internal curves computed by GYS for initial yield and subsequent hardening and four equations for the determination of model coefficients c_1, c_2, c_3, and σ_y

The hardening rules for the material coefficients, c_1, c_2, c_3, were previously defined in equation 57:

$$\dot{c}_i = \dot{\bar{\varepsilon}}^p_{eff} \frac{\partial c_i}{\partial \bar{\varepsilon}^p_{eff}} = \dot{\lambda} \frac{\partial c_i}{\partial \lambda} \; i = 1,2,3 \; \dot{\sigma}_y = \dot{\bar{\varepsilon}}^p_{eff} \frac{\partial \sigma_y}{\partial \bar{\varepsilon}^p_{eff}} = \dot{\lambda} \frac{\partial \sigma_y}{\partial \lambda}$$

Because $\sigma_y = \sigma_t$, the hardening rule for uni-axial tension stress state can be written as:

$$\dot{\sigma}_t = \dot{\bar{\varepsilon}}^p_{eff} \frac{\partial \sigma_y}{\partial \bar{\varepsilon}^p_{eff}} = \dot{\varepsilon}^p_t \frac{\partial \sigma_t}{\partial \varepsilon^p_t} = \dot{\lambda} \frac{\partial \sigma_t}{\partial \lambda} \tag{117}$$

where ε^p_t is the true plastic strain in uni-axial tension. The hardening rule for uni-axial compression is:

$$\dot{\sigma}_c = \dot{\varepsilon}^p_c \frac{\partial \sigma_c}{\partial \varepsilon^p_c} \tag{118}$$

where ε^p_c is the true plastic strains in uni-axial compression. The hardening rule for the pure-shear stress state is:

$$\dot{\sigma}_s = \dot{\varepsilon}^p_s \frac{\partial \sigma_s}{\partial \varepsilon^p_s} \tag{119}$$

where ε^p_s is the true plastic strain in pure-shear.

3.4.5 The Special Case of Tension and Compression Symmetry in Yielding

If there is no tensile-compressive asymmetry in the yielding (i.e., the tension yield stress and the compression yield stress are identical), then the ratio of tension yield stress over compression yield stress is equal to one $\left(\frac{\sigma_t}{\sigma_c} = 1\right)$. Using the summary in equation 116 leads to:

$$\frac{\sigma_t}{\sigma_c} = 1 = c_1 - c_2 + c_3 \tag{120}$$

Because $c_1 + c_2 + c_3 = 1$ for this specific case, $c_2 = 0$. Therefore, if there is no tensile-compressive asymmetry, $c_2 = 0$, and using equation 106, the plastic strain rate in the direction of the compressive load is given by:

$$\dot{\varepsilon}_{33}^{p} = -\dot{\varepsilon}_{c}^{p} = \dot{\lambda}[(-c_1 - c_3)] \tag{121}$$

Because $c_1 + c_2 + c_3 = 1$, when the tension and compression yields are the same, and $c_2 = 0$, c_3 can be written in terms of c_1:

$$c_3 = 1 - c_1 \tag{122}$$

then the plastic strain rate in the direction of the compressive load is given by:

$$\dot{\varepsilon}_{33}^{p} = -\dot{\varepsilon}_{c}^{p} = \dot{\lambda}[(-c_1 - (1 - c_1)] = -\dot{\lambda} \tag{123}$$

3.4.6 Additional Examples, the Material Coefficients, and the Lode Parameter

As can be seen in the previous examples, the Lode parameter $\left(cos3\vartheta = \frac{27J_3}{2\sigma_{vm}^3}\right)$ is one of the variables that controls the shape of the yield surface in GYS. As a result, states of stress that have the same Lode parameters have similar yield surface characteristics.

As discussed in section 3.4.1 for uni-axial tension, the Lode parameter = 1. For equi-biaxial compression, the following relations hold:

$$\boldsymbol{\sigma} = \begin{bmatrix} 0 & 0 & 0 \\ 0 & -\sigma & 0 \\ 0 & 0 & -\sigma \end{bmatrix} \Rightarrow p = \frac{2\sigma}{3} \Rightarrow \boldsymbol{s} = \frac{\sigma}{3}\begin{bmatrix} 2 & 0 & 0 \\ 0 & -1 & 0 \\ 0 & 0 & -1 \end{bmatrix} \Rightarrow \begin{Bmatrix} \sigma_{vm} = \sigma \\ \frac{27J_3}{2\sigma_{vm}^3} = 1 \end{Bmatrix} \tag{124}$$

Comparing equation 124 to equation 92, it can be seen that the deviatoric stress tensors for uni-axial tension and bi-axial compression are identical. Similarly, for uni-axial compression, the Lode parameter = -1. Comparing equation 101 to equation 125, it can be seen that the deviatoric stress tensors for uni-axial compression and bi-axial tension are also identical. For bi-axial tension, the following relations hold:

$$\boldsymbol{\sigma} = \begin{bmatrix} \sigma & 0 & 0 \\ 0 & \sigma & 0 \\ 0 & 0 & 0 \end{bmatrix} \Rightarrow p = -\frac{2\sigma}{3} \Rightarrow \boldsymbol{s} = \frac{\sigma}{3}\begin{bmatrix} 1 & 0 & 0 \\ 0 & 1 & 0 \\ 0 & 0 & -2 \end{bmatrix} \Rightarrow \begin{Bmatrix} \sigma_{vm} = \sigma \\ \frac{27J_3}{2\sigma_{vm}^3} = -1 \end{Bmatrix} \tag{125}$$

The Lode parameter is zero for a pure-shear state. Comparing equation 109 to equation 126, the plane strain stress state produces the same deviatoric stress tensor as pure-shear.

$$\boldsymbol{\sigma} = \begin{bmatrix} \sigma & 0 & 0 \\ 0 & \sigma/2 & 0 \\ 0 & 0 & 0 \end{bmatrix} \Rightarrow p = -\frac{\sigma}{2} \Rightarrow \boldsymbol{s} = \frac{\sigma}{2}\begin{bmatrix} 1 & 0 & 0 \\ 0 & 0 & 0 \\ 0 & 0 & -1 \end{bmatrix} \Rightarrow \begin{Bmatrix} \sigma_{vm} = \sqrt{3}\sigma/2 \\ \frac{27J_3}{2\sigma_{vm}^3} = 0 \end{Bmatrix} \tag{126}$$

Therefore, the following stress states will have the same material coefficients in the GYS model, because they have same J_3 value:

- Uni-axial tension and bi-axial compression (Lode parameter = 1)
- Uni-axial compression and bi-axial tension (Lode parameter = -1)
- Pure-shear and plane strain (Lode parameter = 0)

Theoretically, either of the above choices could be made for tests to be used to generate the GYS material coefficients. For example, the GYS model would produce the same result whether input is generated from a uni-axial tension test or a biaxial compression test. In practice, the tests presented in the previous sections are typically chosen.

3.5 GYS Constitutive Relations and the Material Law

Assuming that the elastic response of the material is isotropic, Hooke's law relates the strain rate tensor to an objective rate of the Cauchy stress tensor. This material law was previously defined in section 3.1 as

$$\dot{\boldsymbol{\sigma}} = C_{ijkl}\left(\dot{\boldsymbol{\varepsilon}} - \dot{\boldsymbol{\varepsilon}}_p\right)$$

where C_{ijkl} is the fourth-order symmetric positive definite isotropic stiffness tensor and is defined as

$$C_{ijkl} = \lambda_c \delta_{ij}\delta_{kl} + \mu\left(\delta_{ik}\delta_{jl} + \delta_{il}\delta_{jk}\right) \tag{127}$$

In equation 127, λ_c and μ are the Lamé constants and are defined as $\lambda_c = K - \frac{2}{3G}$ and $\mu = G$ (note that the Lamé constant, λ_c, is not directly related to the plastic multiplier, λ). The bulk modulus is defined as $K = \frac{E}{3(1-2\nu)}$, and $G = \frac{E}{2(1+\nu)}$ is the shear modulus. The elastic modulus E and Poisson's ratio ν are assumed to remain unchanged through the plastic deformation. The plastic part of the deformation is treated by strain rate and temperature-dependent tabulated hardening curves.

During elastic deformation $f < 0$, by definition the plastic multiplier rate, $\dot{\lambda} = 0$ and $\dot{\boldsymbol{\varepsilon}}_p = \mathbf{0}$. Therefore, the material law for elastic deformation may be written as

$$\dot{\boldsymbol{\sigma}} = C_{ijkl}\dot{\boldsymbol{\varepsilon}} \tag{128}$$

Equation 128 has a total of six equations and six unknowns.

During plastic deformation $f = 0$, by definition $\dot{\lambda} > 0$, and the plastic strain rate tensor was defined in equation 36 as

$$\dot{\boldsymbol{\varepsilon}}_{\boldsymbol{p}} = \dot{\lambda}\frac{\partial f}{\partial \boldsymbol{\sigma}}$$

Therefore, the material law for plastic deformation may be written as

$$\dot{\boldsymbol{\sigma}} = C_{ijkl}\left(\dot{\boldsymbol{\varepsilon}} - \dot{\lambda}\frac{\partial f}{\partial \boldsymbol{\sigma}}\right) \tag{129}$$

Equation 129 has a total of seven equations and seven unknowns.

The elasto-plastic material law may be written in the Kuhn-Tucker (Kuhn & Tucker, 1951) form, in which the flow rule is written as

$$f\big(\boldsymbol{\sigma}, \boldsymbol{q}(\boldsymbol{\lambda})\big) \leq 0 \tag{130}$$

Then with plastic deformation, $\dot{\lambda} \geq 0$, and $f\dot{\lambda} = 0$, and

$$\dot{\boldsymbol{q}} = \dot{\boldsymbol{\lambda}} \frac{\partial \boldsymbol{q}}{\partial \boldsymbol{\lambda}} \tag{131}$$

where q is a vector containing the hardening parameters, σ_y, c_1, c_2, and c_3. In the plastic state, the seventh equation completing equation 129 is given by

$$f = 0 \tag{132}$$

3.6 Comparison of J_3 Dependent Yield Surfaces: GYS, Hosford, Drucker, Cazacu-Barlat

The von Mises, Drucker, Cazacu-Barlat, and Hosford yield surfaces, which were previously introduced in section 2 (von Mises, 1913, Drucker, 1949, Cazacu & Barlat, 2004, Hosford, 1972), can be recovered from the GYS model. The GYS yield function can produce the same behavior as the Hosford yield function, as long as the order *m* in the Hosford model is selected to be less than or equal to 6. Table 1 compares the features of these yield surfaces in terms of tension-compression asymmetry, ratio of yield in pure-shear to yield in tension, number of yielding parameters, and order of the yield surface.

Table 1. Comparison of properties of yield surfaces

	von Mises	Hosford	Drucker	Cazacu	GYS
Number of yielding input parameters	1	1	2	2	3
Order of yield surface	2	m	6	3	6
Tension-Compression asymmetry	no	no	no	yes	yes
Pure-shear yield / tension yield	fixed value	fixed to m (order of yield surface)	can be adjusted using parameter c	fixed to tension-compression asymmetry via c	can be adjusted using parameter c_1
Pure-shear yield / tension yield	0.577	$\frac{1}{(1+2^{m-1})^{1/m}}$	$\frac{1}{\sqrt{3}}\left[1-\frac{4c}{27}\right]^{1/6}$	$\left[\frac{1}{3\sqrt{3}}-\frac{2c}{27}\right]^{1/3}$	$\frac{1}{c_1\sqrt{3}}$

Consider the GYS yield function presented in equation 51, and simplifying slightly, the GYS yield surface is

$$f(\sigma_{eff}, \sigma_y) = \sigma_{vm}\left[c_1 + c_2\frac{27J_3}{2\sigma_{vm}^3} + c_3\frac{729J_3^2}{4\sigma_{vm}^6}\right] - \sigma_y \tag{133}$$

Recalling that σ_{vm} is defined in equation 10 as $\sigma_{vm} = \sqrt{3J_2}$ and rewriting equation 133 yields a form of the GYS surface that can be used in comparison to the other yield surface formulations:

$$f = \sqrt{J_2}\left[\sqrt{3}c_1 + \sqrt{3}c_2\frac{27J_3}{\sqrt{108J_2^3}} + \sqrt{3}c_3\frac{729J_3^2}{108J_2^3}\right] - \sigma_y \tag{134}$$

3.6.1 Comparison to Drucker

In the Drucker yield surface, there is no tension-compression asymmetry. Therefore, as shown in section 3.4.5, to emulate Drucker, c_2 must be zero. Setting $c_2 = 0$ in equation 134 yields

$$c_2 = 0 \Rightarrow f = \left[\frac{\sqrt{3J_2}c_1}{J_2^3}\left(J_2^3 + \frac{c_3}{c_1}\frac{27J_3^2}{4}\right)\right] - \sigma_y \tag{135}$$

As shown in table 1, shear yield relative to tension yield in the Drucker model is given by

$$\frac{\sigma_s}{\sigma_t} = \frac{1}{\sqrt{3}}\left[1 - \frac{4c}{27}\right]^{1/6} \tag{136}$$

If the ratio of yield in pure-shear to yield in tension is defined as equivalent to that of Drucker model (equation 136), using equation 116, the c_1 and c_3 material coefficients of the GYS model corresponding to the Drucker model are given by

$$c_1 = \frac{\sigma_t}{\sqrt{3}\sigma_s} = \frac{1}{\left[1-\frac{4c}{27}\right]^{1/6}} \quad c_3 = 1 - c_1 = 1 - \frac{1}{\left[1-\frac{4c}{27}\right]^{1/6}} \tag{137}$$

3.6.2 Comparison to Cazacu-Barlat

The Cazacu-Barlat formulation can be recovered from the GYS formulation; beginning by setting $c_3 = 0$ as shown:

$$c_3 = 0 \Rightarrow f = \left[\frac{\sqrt{3J_2}c_1}{\sqrt{J_2^3}}\left(J_2^{3/2} + \frac{c_2}{c_1}\sqrt{\frac{27}{4}}J_3\right)\right] - \sigma_y \tag{138}$$

In the Cazacu-Barlat model, the ratio of shear stress yield relative to the uni-axial tension yield stress is fixed by a material parameter *c*:

$$\frac{\sigma_s}{\sigma_t} = \left[\frac{1}{3\sqrt{3}} - \frac{2c}{27}\right]^{1/3} \tag{139}$$

where the material parameter *c* is determined by the tension-compression asymmetry and was previously presented in section 2.1.3:

$$c = \frac{3\sqrt{3}(\sigma_t^3 - \sigma_c^3)}{2(\sigma_t^3 + \sigma_c^3)}$$

For the GYS model to recover the Cazacu-Barlat model, the ratio of shear stress yield relative to the uni-axial tension yield stress must be set equivalent to that of the Cazacu-Barlat model. Therefore, using equation 116 and equation 139, the GYS material coefficients (with $c_3 = 0$) that make the GYS model's behavior the same as the Cazacu-Barlat model are given by

$$c_1 = \frac{\sigma_t}{\sqrt{3}\sigma_s} = \frac{1}{\sqrt{3}\left[\frac{1}{3\sqrt{3}} - \frac{2c}{27}\right]^{1/3}} \quad c_2 = 1 - c_1 = 1 - \frac{1}{\sqrt{3}\left[\frac{1}{3\sqrt{3}} - \frac{2c}{27}\right]^{1/3}} \tag{140}$$

The Cazacu-Barlat yield surfaces for different tension/compression yield ratios are shown in figure 20. The GYS yield surfaces using the same tension/compression yield ratios are also shown in figure 20. Comparison of the results from the GYS and Cazacu-Barlat models demonstrates that the GYS model is able to predict the same response as the Cazacu-Barlat model. Note that when the tension and the compression are equal, as specified for curves B and E in figure 20, a von Mises yield surface results.

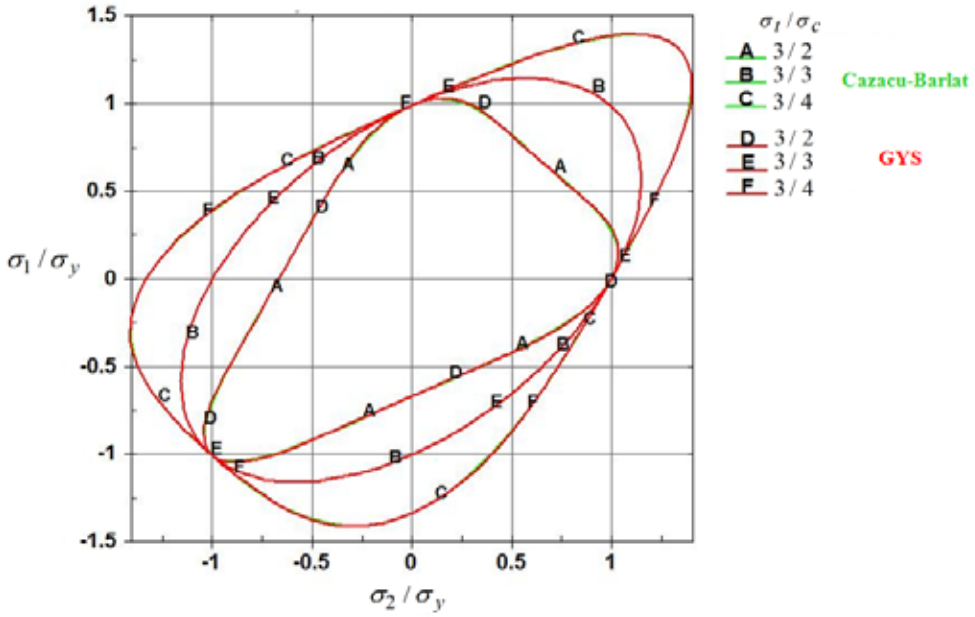

Figure 20. Comparison between the Cazacu-Barlat and GYS yield surface models in the plane stress space corresponding to uni-axial tension/uni-axial compression yield ratios of 3/2, 3/3, 3/4

3.6.3 Comparison to Hosford

As introduced in section 2.1.2, the Hosford yield surface in terms of deviatoric stress invariants is given by:

$$|s_1 - s_2|^m + |s_3 - s_1|^m + |s_2 - s_3|^m \leq 2\sigma_y^m \tag{141}$$

The relation between Lode angle and J_3 is given by the differences between the principal deviatoric stress components, which can be written as:

$$s_3 - s_1 = \frac{2}{3}\sigma_{vm}\left(cos\left(\vartheta + \frac{2\pi}{3}\right) - cos\vartheta\right) = \sigma_{vm}\left(-\frac{sin\vartheta}{\sqrt{3}} - cos\vartheta\right) \tag{142}$$

$$s_1 - s_2 = \frac{2}{3}\sigma_{vm}\left(cos\vartheta - cos\left(\vartheta - \frac{2\pi}{3}\right)\right) = \sigma_{vm}\left(cos\vartheta - \frac{sin\vartheta}{\sqrt{3}}\right) \tag{143}$$

$$s_2 - s_3 = \frac{2}{3}\sigma_{vm}\left(cos\left(\vartheta - \frac{2\pi}{3}\right) - cos\left(\vartheta + \frac{2\pi}{3}\right)\right) = \sigma_{vm}\left(\frac{2sin\vartheta}{\sqrt{3}}\right) \tag{144}$$

Using equations 142, 143, and 144 to rewrite equation 141 yields:

$$\sigma_{vm}^m\left(cos\vartheta + \frac{sin\vartheta}{\sqrt{3}}\right)^m + \sigma_{vm}^m\left(cos\vartheta - \frac{sin\vartheta}{\sqrt{3}}\right)^m + \sigma_{vm}^m\left(\frac{2sin\vartheta}{\sqrt{3}}\right)^m \leq 2\sigma_y^m \tag{145}$$

And the effective stress of the Hosford model, in terms of the von Mises stress and Lode angle, can then be written as:

$$\sigma_{eff} = \left[\frac{1}{2}\sigma_{vm}^m\left(\left(cos\vartheta + \frac{sin\vartheta}{\sqrt{3}}\right)^m + \left(cos\vartheta - \frac{sin\vartheta}{\sqrt{3}}\right)^m + \left(\frac{2sin\vartheta}{\sqrt{3}}\right)^m\right)\right]^{1/m} \tag{146}$$

Using the trigonometric relationship:

$$\frac{cos\left(\vartheta + \frac{\pi}{6}\right)}{cos\frac{\pi}{6}} = \frac{cos\vartheta cos\frac{\pi}{6} - sin\vartheta sin\frac{\pi}{6}}{cos\frac{\pi}{6}} = cos\vartheta - \frac{sin\vartheta}{\sqrt{3}} \tag{147}$$

the Hosford effective stress (equation 146) can be rewritten as the product of the von Mises stress, and a scale factor (in brackets), which is only a function of the Lode angle:

$$\sigma_{eff} = \sigma_{vm}\left\{\frac{2^{\frac{m-1}{m}}}{\sqrt{3}}\left[\left(\left(cos\left(\vartheta - \frac{\pi}{6}\right)\right)^m + \left(cos\left(\vartheta + \frac{\pi}{6}\right)\right)^m + (sin\vartheta)^m\right)\right]^{1/m}\right\} \tag{148}$$

Figure 21 shows the magnitude of the Lode angle-dependent scale factor using different orders (m) of the Hosford model for Lode angles in a range of $0 \leq \theta \leq \frac{\pi}{3}$ radians. The different orders correspond to the Tresca yield function (m = 1), the von Mises yield function (m = 2), BCC type materials (m = 3), and FCC type materials (m = 4).

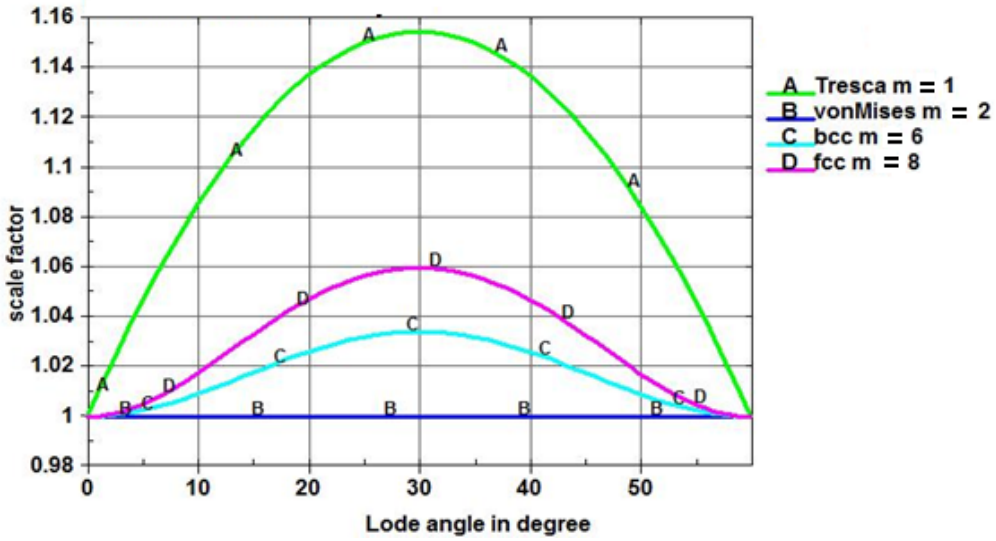

Figure 21. Magnitude of the scale factor relating von Mises stress to the effective stress as a function of Lode angle

To compare the Hosford yield surface to the GYS yield surface, the ratios of yield in uni-axial tension to yield in pure-shear for different orders (m) can be calculated using:

$$\frac{\sigma_t}{\sigma_s} = (1 + 2^{m-1})^{1/m} \tag{149}$$

and the results are:

$$\begin{gathered} \frac{\sigma_t}{\sigma_s} = 1.732 \Rightarrow m = 2\ (von\ Mises) \\ \frac{\sigma_t}{\sigma_s} = 1.792 \Rightarrow m = 6\ (BCC\ materials) \\ \frac{\sigma_t}{\sigma_s} = 1.835 \Rightarrow m = 8\ (FCC\ materials) \\ \frac{\sigma_t}{\sigma_s} = 2.000 \Rightarrow m = 1\ (Tresca) \end{gathered} \tag{150}$$

Using the ratios of $\frac{\sigma_t}{\sigma_s}$ from equation 150, the GYS model material coefficients c_1 and c_3 can be calculated:

$$c_1 = \frac{\sigma_t}{\sigma_s\sqrt{3}} = \frac{(1+2^{m-1})^{1/m}}{\sqrt{3}} \quad c_3 = 1 - c_1 = 1 - \frac{(1+2^{m-1})^{1/m}}{\sqrt{3}} \tag{151}$$

Because, as in the Drucker model, there is no tension-compression asymmetry in the Hosford model, again $c_2 = 0$.

Figure 22 compares the GYS and Hosford formulations in terms of the ratio of the von Mises stress to the Hosford effective stress for orders (m) of 2, 6, 8, and infinite. From figure 22, it can be seen

that there is an exact match at the orders of 2 and 6. Therefore, the GYS yield function can emulate the Hosford yield function, when that function is limited to order (m) 6 and below. The difference between two models at the order of 8 is small and becomes relatively large at infinity.

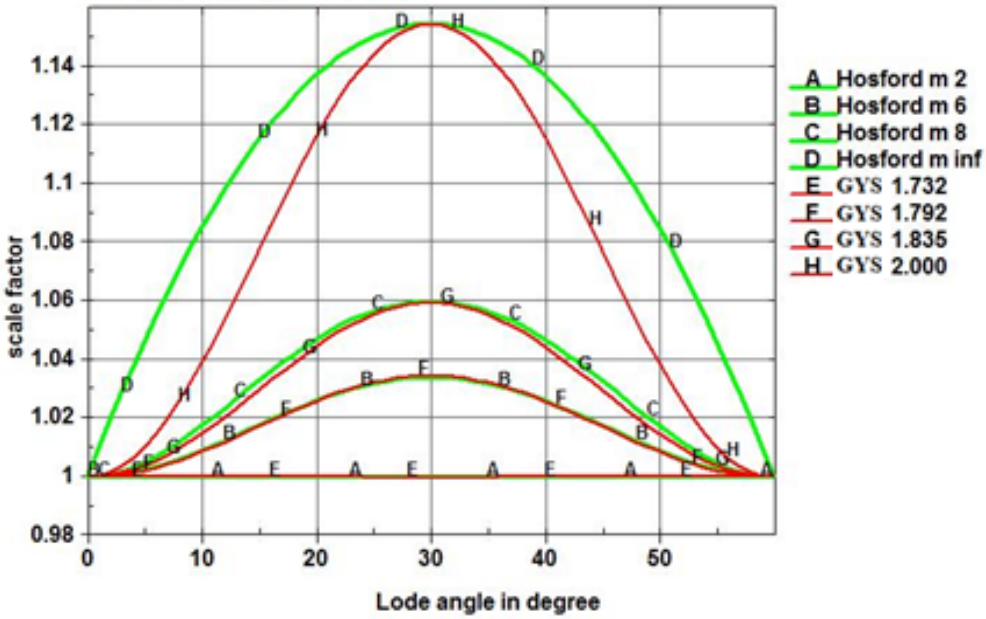

Figure 22. Magnitude of the scale factor relating von Mises stress to the effective stress as a function of Lode angle, Hosford model, and the GYS model

An example of the effect that tension-compression asymmetry may have on a yield surface is shown in figure 23. Using the specific case of $\frac{\sigma_t}{\sigma_s} = 1.792$ (m = 6), the ratio/scale factor was calculated with and without tension-compression asymmetry using the GYS model (remembering that tension-compression asymmetry can be included in GYS but not in Hosford). The Lode angle equals zero degrees is the uni-axial tension meridian, and the Lode angle equals sixty degrees is the uni-axial compression meridian. In uni-axial tension, the results of GYS and Hosford are the same. However, as the state of stress moves toward compression, the Hosford model cannot match a difference in compressive yield and is symmetric for uni-axial tension and compression. In the GYS model, scale factors for the uni-axial tension and uni-axial compression are different if there is tension-compression asymmetry, which is appropriate.

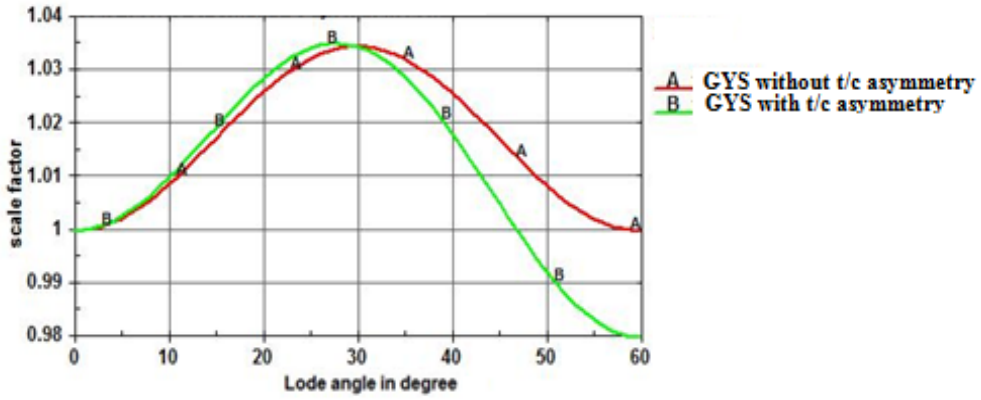

Figure 23. Magnitude of the scale factor relating von Mises stress to the effective stress, as a function of Lode angle, with and without tension-compression asymmetry corresponding to order *m* = 6

3.6.4 Uniqueness

Convexity and uniqueness are required for robust numerical calculations involving yield surfaces. If a yield function is convex and smooth, then a solution is unique for any given state of stress. Although the Hosford yield function is convex and smooth, the uniqueness is lost in practical numerical applications for $m > 10$ due to the very "flat" nature of the resulting yield surface. In figure 24, the first principal stress over the yield stress is plotted against the second yield principal stress over the yield stress. For orders $m = 10$ and $m = 50$, the multiple first principal stress over the yield stress solutions could result from the same second principal stress over yield stress, as implied by the flatness of these curves in figure 24.

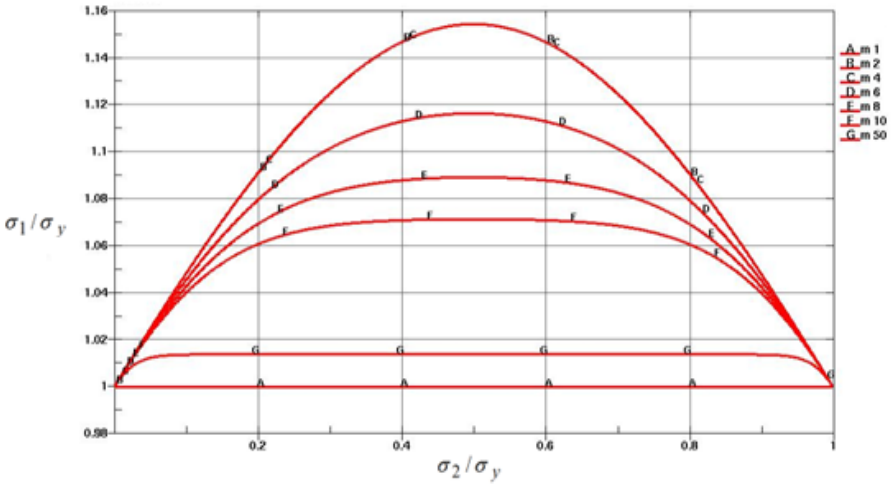

Figure 24. Principal stresses over yield stress demonstrating Hosford non-unique flow for higher orders

If the flow is not unique, then the corresponding state of stress is not uniquely determined, and there are multiple solutions to the same input conditions. Consider an example of a plane strain

state. Assuming that the elastic deformations are small compared to plastic deformations, then the plane strain state is:

$$\dot{\boldsymbol{\varepsilon}} = \begin{bmatrix} \dot{\varepsilon}_{11} & 0 & 0 \\ 0 & 0 & 0 \\ 0 & 0 & -\dot{\varepsilon}_{11} \end{bmatrix} \approx \dot{\boldsymbol{\varepsilon}}_{\boldsymbol{p}} = \dot{\boldsymbol{\varepsilon}}_{\boldsymbol{p}} = \dot{\lambda}\frac{\partial f}{\partial \boldsymbol{\sigma}} \; and \; \boldsymbol{\sigma} = \begin{bmatrix} \sigma_1 & 0 & 0 \\ 0 & a\sigma_1 & 0 \\ 0 & 0 & 0 \end{bmatrix} \tag{152}$$

where a = σ_2 / σ_1.

For von Mises plasticity, the plastic strain rate tensor takes a form:

$$\dot{\boldsymbol{\varepsilon}}_{\boldsymbol{p}} = \begin{bmatrix} \dot{\varepsilon}_{11} & 0 & 0 \\ 0 & 0 & 0 \\ 0 & 0 & -\dot{\varepsilon}_{11} \end{bmatrix} = \dot{\lambda}\boldsymbol{s} = \frac{\dot{\lambda}}{3}\begin{bmatrix} 2-a & 0 & 0 \\ 0 & 2a-1 & 0 \\ 0 & 0 & -1-a \end{bmatrix} \Rightarrow \; a = \frac{\sigma_2}{\sigma_1} = 0.5 \tag{153}$$

and $a = 0.5$ is the unique solution.

For the Hosford yield surface, plane strain deformation leads to $a = \sigma_2 / \sigma_1$ varying with *m* (order) as shown in figure 25. Consequently, values of $a = \sigma_2 / \sigma_1$ that will satisfy the condition for the plane strain deformation are not unique and deviate from 0.5 as the order of the Hosford yield function goes higher (i.e., the number of solutions increases as *m* is increased).

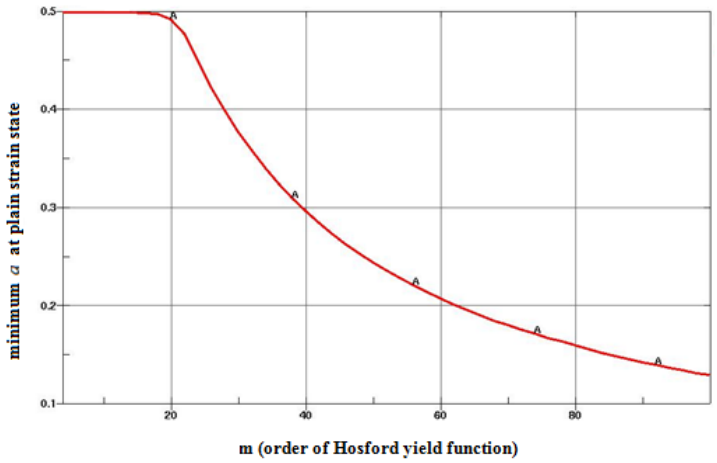

Figure 25. $a = \sigma_2 / \sigma_1$ value for the plane strain condition using the Hosford yield function

For the same plane strain case, the GYS model is used to emulate the Hosford model, as was done in the previous section, using multiple orders *m* and equation 151. With the GYS yield function, plane strain deformation leads to a unique solution of $a = \sigma_2 / \sigma_1 = 0.5$ for multiple orders (*m*), as shown in figure 26.

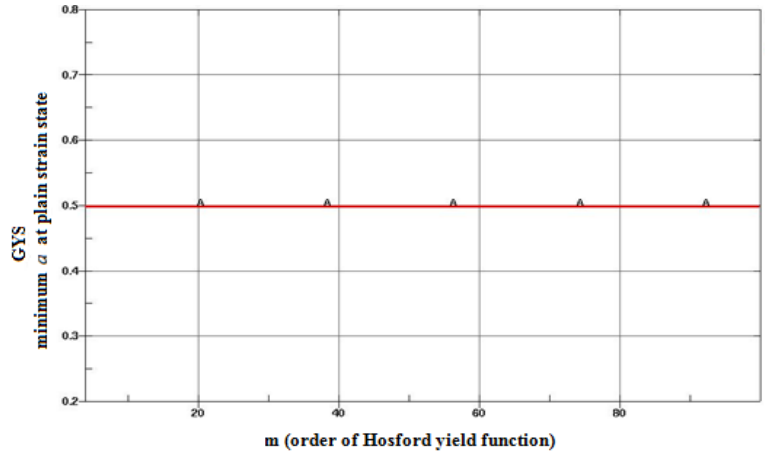

Figure 26. $a = \sigma_2 / \sigma_1$ value for the plane strain condition using the GYS model

Although the GYS function is smooth and unique, it does not guarantee convexity for all cases. In figure 27, the first principal stress over the yield stress is shown as a function of the second yield principal stress over the yield stress. As before, the GYS model was used to emulate the Hosford model, including no tension-compression asymmetry, for a range of orders. The dips in some of the curves indicate non-convexity of the yield surface. Therefore, specific convexity conditions need to be determined and applied in the GYS model to guarantee unique solutions. Convexity of the GYS model and a comparison between the GYS, Drucker, and Cazacu-Barlat convexity regions will be discussed in detail in the next section.

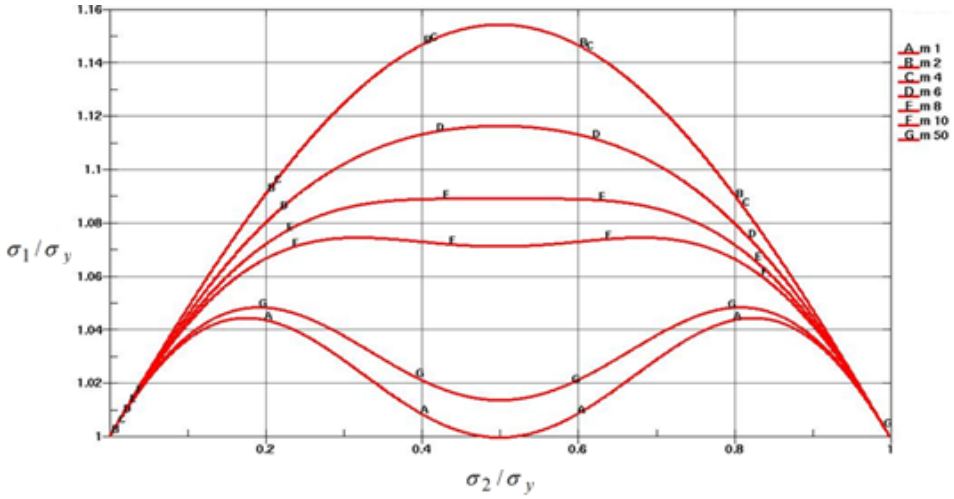

Figure 27. Principal stresses over yield stress demonstrating GYS non-convex flow

3.7 Convexity of the GYS Model and Comparison between the GYS, Drucker, and Cazacu-Barlat Convexity Regions

A yield surface must be convex for unique numerical solutions to the plasticity analysis to be guaranteed. The requirement for yield surface convexity was demonstrated by Drucker (Drucker, 1950). Drucker introduced the idea of a stable plastic material and stated that one of the conditions

for stability was that the yield surface must be convex. Furthermore, a material that is stable in this sense must satisfy the principle of maximum plastic resistance.

The principle of maximum plastic resistance is described by Bower (Bower, 2010). The principle can be written mathematically as the dot product of the stress and plastic strain rate vectors:

$$\left(\sigma_{ij} - \sigma_{ij}^{*}\right) \cdot \left(d\varepsilon_{ij}^{p}\right) \geq 0 \tag{154}$$

where σ_{ij}^{*} is a stress that just satisfies the yield criterion. Equation 154 expresses that the angle between the vectors formed by $(\sigma_{ij} - \sigma_{ij}^{*})$, and $d\varepsilon_{ij}^{p}$ is less than 90° for all stresses and strain rates. This is true only when the yield surface is convex and the plastic strain rate vector is normal to the yield surface.

It was shown in section 3.6.4, specifically in figure 27, that the GYS yield function is not always convex. This means that the values of the GYS coefficients c_1, c_2 , and c_3, as determined by the material properties, may lead to a non-convex yield surface. As a result, the range of coefficient values may need to be modified to satisfy the convexity requirement. The von Mises, Hosford, Drucker-Prager, and Cazacu-Barlat yield functions can also be assessed for their convexity range.

3.7.1 Convexity Conditions

A yield surface is convex if its curvature is non-negative everywhere on its surface. More formally stated, the curvature of the yield function in two mutually perpendicular directions in the tangent plane at any given point on the surface must be non-negative. Mathematically, this requires that the curvature tensor be positive definite.

The curvature in the tangent plane is given by:

$$N_{pq} = \boldsymbol{U}\boldsymbol{H}\boldsymbol{U}^{\boldsymbol{T}} \tag{155}$$

where:

$$\boldsymbol{U} = \begin{bmatrix} U_{11} & U_{12} & U_{13} \\ U_{21} & U_{22} & U_{33} \end{bmatrix} \; and \; \boldsymbol{H} = \begin{bmatrix} H_{11} & H_{12} & H_{13} \\ H_{21} & H_{22} & H_{23} \\ H_{31} & H_{32} & H_{33} \end{bmatrix} \tag{156}$$

and where H_{ij} is the Hessian of the yield function, f , and is given by:

$$H_{ij} = \frac{\partial^2 f}{\partial \sigma_i \sigma_j} \tag{157}$$

where σ_i is the principal stress vector. $\boldsymbol{U}$ consists of two basis vectors that lie in the plane, which is tangent to f in the principal stress space. After Rockafellar (Rockafellar, 1972), to ensure the convexity of a yield surface, the Hessian matrix of f must be positive semi-definite with respect to the principal stresses. The Hessian $\boldsymbol{H}$ of a function f (x_1, $x_{2,\ldots\ldots}$ x_n) with respect to x_1, $x_{2,\ldots}x_n$ is the Jacobian matrix of the derivatives f ($\frac{\partial f}{\partial x_1}, \frac{\partial f}{\partial x_1} \ldots \ldots \frac{\partial f}{\partial x_n}$).

A yield function is defined in stress space as:

$$f(\boldsymbol{\sigma}) = f(\sigma_{xx}, \sigma_{xy}, \sigma_{xz}, \sigma_{yy}, \sigma_{yz}, \sigma_{zz}) \leq 0 \tag{158}$$

The Hessian of the yield function in stress space has 36 components, which reduces to 21 components due to the symmetry of the stress tensor:

$$H_{ij} = \frac{\partial^2 f}{\partial \boldsymbol{\sigma}^2} = \begin{bmatrix} \frac{\partial f}{\partial \sigma_{xx}} \\ \frac{\partial f}{\partial \sigma_{xy}} \\ \frac{\partial f}{\partial \sigma_{xz}} \\ \frac{\partial f}{\partial \sigma_{yy}} \\ \frac{\partial f}{\partial \sigma_{yz}} \\ \frac{\partial f}{\partial \sigma_{zz}} \end{bmatrix} \begin{bmatrix} \frac{\partial}{\partial \sigma_{xx}} & \frac{\partial}{\partial \sigma_{xy}} & \frac{\partial}{\partial \sigma_{xz}} & \frac{\partial}{\partial \sigma_{yy}} & \frac{\partial}{\partial \sigma_{yz}} & \frac{\partial}{\partial \sigma_{zz}} \end{bmatrix} \tag{159}$$

The yield function is defined in principal stress space as:

$$f(\sigma_1, \sigma_2, \sigma_3) \leq 0 \tag{160}$$

Then the convexity in principal stress space can be described as:

$$\boldsymbol{H} = \frac{\partial^2 f}{\partial \boldsymbol{\sigma}^2} = \begin{bmatrix} \frac{\partial f}{\partial \sigma_1} \\ \frac{\partial f}{\partial \sigma_2} \\ \frac{\partial f}{\partial \sigma_3} \end{bmatrix} \begin{bmatrix} \frac{\partial f}{\partial \sigma_1} & \frac{\partial f}{\partial \sigma_2} & \frac{\partial f}{\partial \sigma_3} \end{bmatrix} = \begin{bmatrix} \frac{\partial^2 f}{\partial \sigma_1^2} & \frac{\partial^2 f}{\partial \sigma_1 \sigma_2} & \frac{\partial^2 f}{\partial \sigma_1 \sigma_3} \\ \cdots & \frac{\partial^2 f}{\partial \sigma_2^2} & \frac{\partial^2 f}{\partial \sigma_2 \sigma_3} \\ \cdots & \cdots & \frac{\partial^2 f}{\partial \sigma_3^2} \end{bmatrix} \tag{161}$$

Convexity in the principal stress space is a sufficient condition for convexity in the stress space. Therefore, a yield surface is convex if the Hessian matrix is positive semi-definite in principal stress space. In the principal stress space, the Hessian has nine components, which reduce to six components because of symmetry, as shown in equation 161. The eigenvalues of the Hessian matrix will be used to determine if it is positive semi-definite.

It was shown in section 3.3.2 that the GYS flow rule is isochoric, and so equation 81 is true:

$$\left[\frac{\partial f}{\partial \sigma_1} + \frac{\partial f}{\partial \sigma_2} + \frac{\partial f}{\partial \sigma_3}\right] \equiv 0$$

Therefore:

$$\frac{\partial}{\partial \sigma_1}\left[\frac{\partial f}{\partial \sigma_1} + \frac{\partial f}{\partial \sigma_2} + \frac{\partial f}{\partial \sigma_3}\right] \equiv 0$$

$$\frac{\partial}{\partial \sigma_2}\left[\frac{\partial f}{\partial \sigma_1}+\frac{\partial f}{\partial \sigma_2}+\frac{\partial f}{\partial \sigma_3}\right] \equiv 0 \tag{162}$$

$$\frac{\partial}{\partial \sigma_3}\left[\frac{\partial f}{\partial \sigma_1}+\frac{\partial f}{\partial \sigma_2}+\frac{\partial f}{\partial \sigma_3}\right] \equiv 0$$

Using equation 161 and the definition of the Hessian matrix in equation 157, equation 162 leads to:

$$\begin{aligned} H_{11} + H_{12} + H_{13} &= 0 \\ H_{21} + H_{22} + H_{23} &= 0 \\ H_{31} + H_{32} + H_{33} &= 0 \end{aligned} \tag{163}$$

Equation 163, the convexity conditions, can be assembled into a set of three vectors:

$$\begin{vmatrix} H_{31} \\ H_{21} \\ H_{31} \end{vmatrix} + \begin{vmatrix} H_{12} \\ H_{22} \\ H_{32} \end{vmatrix} + \begin{vmatrix} H_{13} \\ H_{23} \\ H_{33} \end{vmatrix} = \begin{vmatrix} 0 \\ 0 \\ 0 \end{vmatrix} \tag{164}$$

and each vector could be written as a linear combination of the other two. For example:

$$\begin{vmatrix} H_{31} \\ H_{21} \\ H_{31} \end{vmatrix} = -\begin{vmatrix} H_{12} \\ H_{22} \\ H_{32} \end{vmatrix} - \begin{vmatrix} H_{13} \\ H_{23} \\ H_{33} \end{vmatrix} \tag{165}$$

Therefore, by definition, the Hessian matrix of the GYS flow rule is singular, and $det(\boldsymbol{H}) = 0$.

All eigenvalues of a real symmetric matrix such as the Hessian matrix, $|H - \eta I| = 0$, are real. In this report, because the typical Greek symbol for eigenvalues, λ, represents the plastic multiplier, the Greek letter η will be used to represent eigenvalues, with η_i representing specific eigenvalues. Some properties of the eigenvalues of a matrix, such as the Hessian matrix (equation 156), are

$$\begin{aligned} \eta_1 + \eta_2 + \eta_3 &= tr(\boldsymbol{H}) = H_{11} + H_{22} + H_{33} \\ \eta_1 \eta_2 \eta_3 &= det(\boldsymbol{H}) \end{aligned} \tag{166}$$

The sum of the principal minors of the Hessian matrix is defined as M_{ii}. Therefore:

$$\begin{aligned} \eta_1 \eta_2 + \eta_1 \eta_3 + \eta_2 \eta_3 &= M_{11} + M_{22} + M_{33} \\ \eta_1 \eta_2 + \eta_1 \eta_3 + \eta_2 \eta_3 &= H_{11}H_{22} - H_{12}^2 + H_{11}H_{33} - H_{13}^2 + H_{33}H_{22} - H_{23}^2 \end{aligned} \tag{167}$$

The Hessian matrix is positive semi-definite if all of its eigenvalues are positive or zero. If the determinant of the matrix is zero, then to show that the eigenvalues are all positive or zero, it is sufficient to show that the trace and the sum of the principal minors are positive or zero.

Because equation 165 showed that $det(\boldsymbol{H}) = 0$, then one of the eigenvalues has to be zero. If the third eigenvalue is selected, then $\eta_3 = 0$, and it follows that:

$$\begin{aligned} \eta_1 + \eta_2 &= tr(\boldsymbol{H}) = H_{11} + H_{22} + H_{33} \\ \eta_1 \eta_2 &= H_{11}H_{22} - H_{12}^2 + H_{11}H_{33} - H_{13}^2 + H_{33}H_{22} - H_{23}^2 \end{aligned} \tag{168}$$

Then for all of its eigenvalues to be positive or zero, and the Hessian matrix to be positive semi-definite, the sum of the remaining two eigenvalues, $\eta_1 + \eta_2$, must be greater than zero. Using equation 168, and by definition of a trace, the trace of the Hessian must also be greater:

$$trace(\boldsymbol{H}) = H_{11} + H_{22} + H_{33} \geq 0 \tag{169}$$

which is the first condition for convexity. Likewise, the product of the remaining two eigenvalues, $\eta_1 \eta_2$, must also be greater than zero and:

$$\begin{aligned} H_{11}H_{22} - H_{12}^2 + H_{11}H_{33} - H_{13}^2 + H_{33}H_{22} - H_{23}^2 &\geq 0 \\ M_1 + M_2 + M_3 &\geq 0 \end{aligned} \tag{170}$$

and these two equivalent equations are the second condition for convexity.

Recalling that the GYS yield function, when written in terms of J_2 and J_3 (equation 134), is:

$$f = \sqrt{J_2}\left[\sqrt{3}c_1 + \sqrt{3}c_2 \frac{27J_3}{\sqrt{108J_2^3}} + \sqrt{3}c_3 \frac{729J_3^2}{108J_2^3}\right] - \sigma_y$$

Then the convexity conditions must also be derived in terms of J_2 and J_3. Beginning with the first convexity condition, the trace of a Hessian matrix (equation 161) can also be written as:

$$trace(\boldsymbol{H}) = \frac{\partial^2 f}{\partial \sigma_1^2} + \frac{\partial^2 f}{\partial \sigma_2^2} + \frac{\partial^2 f}{\partial \sigma_3^2} \tag{171}$$

Therefore, the second derivatives of the yield function, with the variables of J_2 and J_3 and with respect to σ_1, σ_2, and σ_3, must be obtained. Beginning with the first derivative of the yield function f, using the chain rule:

$$\frac{\partial f}{\partial \sigma_1} = \frac{\partial f}{\partial J_2}\frac{\partial J_2}{\partial \sigma_1} + \frac{\partial f}{\partial J_3}\frac{\partial J_3}{\partial \sigma_1}$$

$$\frac{\partial f}{\partial \sigma_2} = \frac{\partial f}{\partial J_2}\frac{\partial J_2}{\partial \sigma_2} + \frac{\partial f}{\partial J_3}\frac{\partial J_3}{\partial \sigma_2} \tag{172}$$

$$\frac{\partial f}{\partial \sigma_3} = \frac{\partial f}{\partial J_2}\frac{\partial J_2}{\partial \sigma_3} + \frac{\partial f}{\partial J_3}\frac{\partial J_3}{\partial \sigma_3}$$

The second derivatives of f with respect to σ_1, σ_2, and σ_3 are:

$$\frac{\partial^2 f}{\partial \sigma_1^2} = \frac{\partial f}{\partial J_2}\frac{\partial^2 J_2}{\partial \sigma_1^2} + \left(\frac{\partial^2 f}{\partial J_2^2}\frac{\partial J_2}{\partial \sigma_1} + \frac{\partial^2 f}{\partial J_3 J_2}\frac{\partial J_3}{\partial \sigma_1}\right)\frac{\partial J_2}{\partial \sigma_1} + \frac{\partial f}{\partial J_3}\frac{\partial^2 J_3}{\partial \sigma_1^2} + \left(\frac{\partial^2 f}{\partial J_2 J_3}\frac{\partial J_2}{\partial \sigma_1} + \frac{\partial^2 f}{\partial J_3^2}\frac{\partial J_3}{\partial \sigma_1}\right)\frac{\partial J_3}{\partial \sigma_1}$$

$$\frac{\partial^2 f}{\partial \sigma_2^2} = \frac{\partial f}{\partial J_2}\frac{\partial^2 J_2}{\partial \sigma_2^2} + \left(\frac{\partial^2 f}{\partial J_2^2}\frac{\partial J_2}{\partial \sigma_2} + \frac{\partial^2 f}{\partial J_3 J_2}\frac{\partial J_3}{\partial \sigma_2}\right)\frac{\partial J_2}{\partial \sigma_2} + \frac{\partial f}{\partial J_3}\frac{\partial^2 J_3}{\partial \sigma_2^2} + \left(\frac{\partial^2 f}{\partial J_2 J_3}\frac{\partial J_2}{\partial \sigma_2} + \frac{\partial^2 f}{\partial J_3^2}\frac{\partial J_3}{\partial \sigma_2}\right)\frac{\partial J_3}{\partial \sigma_2} \tag{173}$$

$$\frac{\partial^2 f}{\partial \sigma_3^2} = \frac{\partial f}{\partial J_2}\frac{\partial^2 J_2}{\partial \sigma_3^2} + \left(\frac{\partial^2 f}{\partial J_2^2}\frac{\partial J_2}{\partial \sigma_3} + \frac{\partial^2 f}{\partial J_3 J_2}\frac{\partial J_3}{\partial \sigma_3}\right)\frac{\partial J_2}{\partial \sigma_3} + \frac{\partial f}{\partial J_3}\frac{\partial^2 J_3}{\partial \sigma_3^2} + \left(\frac{\partial^2 f}{\partial J_2 J_3}\frac{\partial J_2}{\partial \sigma_3} + \frac{\partial^2 f}{\partial J_3^2}\frac{\partial J_3}{\partial \sigma_3}\right)\frac{\partial J_3}{\partial \sigma_3}$$

Therefore, the first and second derivatives of $J_2$with respect to the principal stresses are required to develop equation 173. Solving for J_2, equation 10 can be written as:

$$J_2 = \frac{1}{3}\sigma_{vm}^2 \tag{174}$$

Therefore:

$$\frac{\partial J_2}{\partial \sigma_1} = \frac{1}{3}\frac{\partial \sigma_{vm}^2}{\partial \sigma_1} = \frac{2}{3}\sigma_{vm}\frac{\partial \sigma_{vm}}{\partial \sigma_1}$$

$$\frac{\partial J_2}{\partial \sigma_2} = \frac{1}{3}\frac{\partial \sigma_{vm}^2}{\partial \sigma_2} = \frac{2}{3}\sigma_{vm}\frac{\partial \sigma_{vm}}{\partial \sigma_2} \tag{175}$$

$$\frac{\partial J_2}{\partial \sigma_1} = \frac{1}{3}\frac{\partial \sigma_{vm}^2}{\partial \sigma_3} = \frac{2}{3}\sigma_{vm}\frac{\partial \sigma_{vm}}{\partial \sigma_3}$$

The partial derivative of the von Mises stress with respect to the principal stresses is required to develop equation 175:

$$\frac{\partial \sigma_{vm}}{\partial \sigma_1} = \frac{\partial \sigma_{vm}}{\partial s_1}\frac{\partial s_1}{\partial \sigma_1} + \frac{\partial \sigma_{vm}}{\partial s_2}\frac{\partial s_2}{\partial \sigma_1} + \frac{\partial \sigma_{vm}}{\partial s_3}\frac{\partial s_3}{\partial \sigma_1}$$

$$\frac{\partial \sigma_{vm}}{\partial \sigma_2} = \frac{\partial \sigma_{vm}}{\partial s_1}\frac{\partial s_1}{\partial \sigma_2} + \frac{\partial \sigma_{vm}}{\partial s_2}\frac{\partial s_2}{\partial \sigma_2} + \frac{\partial \sigma_{vm}}{\partial s_3}\frac{\partial s_3}{\partial \sigma_2} \tag{176}$$

$$\frac{\partial \sigma_{vm}}{\partial \sigma_3} = \frac{\partial \sigma_{vm}}{\partial s_1}\frac{\partial s_1}{\partial \sigma_3} + \frac{\partial \sigma_{vm}}{\partial s_2}\frac{\partial s_2}{\partial \sigma_3} + \frac{\partial \sigma_{vm}}{\partial s_3}\frac{\partial s_3}{\partial \sigma_3}$$

Next, the partial derivatives of the von Mises stress with respect to the principal deviatoric stresses is required. Writing equation 10, $\sigma_{vm} = \sqrt{\frac{3}{2}\boldsymbol{s}:\boldsymbol{s}}$, for principal stresses, yields:

$$\sigma_{vm} = \sqrt{\frac{3}{2}(s_1^2 + s_2^2 + s_3^2)} = \left[\frac{3}{2}(s_1^2 + s_2^2 + s_3^2)\right]^{\frac{1}{2}} \tag{177}$$

Therefore:

$$\begin{aligned}
\frac{\partial \sigma_{vm}}{\partial s_1} &= \frac{1}{2}\left[\frac{3}{2}(s_1^2 + s_2^2 + s_3^2)\right]^{-\frac{1}{2}} \frac{(3)(2)s_1}{2} = \frac{3s_1}{2\sigma_{vm}} \\
\frac{\partial \sigma_{vm}}{\partial s_2} &= \frac{1}{2}\left[\frac{3}{2}(s_1^2 + s_2^2 + s_3^2)\right]^{-\frac{1}{2}} \frac{(3)(2)s_2}{2} = \frac{3s_2}{2\sigma_{vm}} \\
\frac{\partial \sigma_{vm}}{\partial s_3} &= \frac{1}{2}\left[\frac{3}{2}(s_1^2 + s_2^2 + s_3^2)\right]^{-\frac{1}{2}} \frac{(3)(2)s_2}{2} = \frac{3s_3}{2\sigma_{vm}}
\end{aligned} \tag{178}$$

which can be used in equation 176. For equation 176, the partial derivatives of the principal deviatoric stresses with respect to the principal stresses are also required. Recalling equation 23:

$$\boldsymbol{\sigma} = \boldsymbol{s} - p\boldsymbol{\delta}$$

which may be written for principal stresses as:

$$\begin{bmatrix} s_1 & 0 & 0 \\ 0 & s_2 & 0 \\ 0 & 0 & s_3 \end{bmatrix} = \begin{bmatrix} \sigma_1 & 0 & 0 \\ 0 & \sigma_2 & 0 \\ 0 & 0 & \sigma_3 \end{bmatrix} + p \begin{bmatrix} 1 & 0 & 0 \\ 0 & 1 & 0 \\ 0 & 0 & 1 \end{bmatrix} \tag{179}$$

where (from equation 24):

$$p = -\frac{1}{3}(\sigma_1 + \sigma_2 + \sigma_3) \tag{180}$$

Therefore:

$$\begin{aligned}
&\frac{\partial s_1}{\partial \sigma_1} = 1 - \frac{1}{3} = \frac{2}{3} \qquad \frac{\partial s_2}{\partial \sigma_1} = -\frac{1}{3} \qquad \frac{\partial s_3}{\partial \sigma_1} = -\frac{1}{3} \\
&\frac{\partial s_1}{\partial \sigma_2} = -\frac{1}{3} \qquad \frac{\partial s_2}{\partial \sigma_2} = 1 - \frac{1}{3} = \frac{2}{3} \qquad \frac{\partial s_3}{\partial \sigma_2} = -\frac{1}{3} \\
&\frac{\partial s_1}{\partial \sigma_3} = -\frac{1}{3} \qquad \frac{\partial s_2}{\partial \sigma_3} = -\frac{1}{3} \qquad \frac{\partial s_3}{\partial \sigma_3} = 1 - \frac{1}{3} = \frac{2}{3}
\end{aligned} \tag{181}$$

Now, using the results from equation 178 and equation 181, equation 176 may be written as:

$$\frac{\partial \sigma_{vm}}{\partial \sigma_1} = \frac{3s_1}{2\sigma_{vm}}\frac{2}{3} - \frac{3s_2}{2\sigma_{vm}}\frac{1}{3} - \frac{3s_3}{2\sigma_{vm}}\frac{1}{3}$$

$$\frac{\partial \sigma_{vm}}{\partial \sigma_2} = -\frac{3s_1}{2\sigma_{vm}}\frac{1}{3} + \frac{3s_2}{2\sigma_{vm}}\frac{2}{3} - \frac{3s_3}{2\sigma_{vm}}\frac{1}{3} \tag{182}$$

$$\frac{\partial \sigma_{vm}}{\partial \sigma_3} = -\frac{3s_1}{2\sigma_{vm}}\frac{1}{3} - \frac{3s_2}{2\sigma_{vm}}\frac{1}{3} + \frac{3s_3}{2\sigma_{vm}}\frac{2}{3}$$

and because:

$$s_1 + s_2 + s_3 = 0 \tag{183}$$

equation 182 may be written as:

$$\frac{\partial \sigma_{vm}}{\partial \sigma_1} = \frac{s_1}{\sigma_{vm}} - \frac{(-s_1 - s_3)}{2\sigma_{vm}} - \frac{s_3}{2\sigma_{vm}} = \frac{3s_1}{2\sigma_{vm}}$$

$$\frac{\partial \sigma_{vm}}{\partial \sigma_2} = -\frac{(-s_2 - s_3)}{2\sigma_{vm}} + \frac{s_2}{\sigma_{vm}} - \frac{s_3}{2\sigma_{vm}} = \frac{3s_2}{2\sigma_{vm}} \tag{184}$$

$$\frac{\partial \sigma_{vm}}{\partial \sigma_3} = -\frac{(-s_2 - s_3)}{2\sigma_{vm}} - \frac{s_2}{2\sigma_{vm}} + \frac{s_3}{\sigma_{vm}} = \frac{3s_3}{2\sigma_{vm}}$$

Finally, the first derivatives of J_2, from equation 175 may be written as:

$$\frac{\partial J_2}{\partial \sigma_1} = \frac{2}{3}\sigma_{vm}\frac{\partial \sigma_{vm}}{\partial \sigma_1} = \frac{2}{3}\sigma_{vm}\frac{3s_1}{2\sigma_{vm}} = s_1$$

$$\frac{\partial J_2}{\partial \sigma_2} = \frac{2}{3}\sigma_{vm}\frac{\partial \sigma_{vm}}{\partial \sigma_2} = \frac{2}{3}\sigma_{vm}\frac{3s_2}{2\sigma_{vm}} = s_2 \tag{185}$$

$$\frac{\partial J_2}{\partial \sigma_1} = \frac{2}{3}\sigma_{vm}\frac{\partial \sigma_{vm}}{\partial \sigma_3} = \frac{2}{3}\sigma_{vm}\frac{3s_3}{2\sigma_{vm}} = s_3$$

Taking the second derivatives of equation 185, and using equation 181, the second derivatives of J_2 are:

$$\frac{\partial^2 J_2}{\partial \sigma_1^2} = \frac{\partial s_1}{\partial \sigma_1} = \frac{2}{3}$$

$$\frac{\partial^2 J_2}{\partial \sigma_2^2} = \frac{\partial s_2}{\partial \sigma_2} = \frac{2}{3} \tag{186}$$

$$\frac{\partial^2 J_2}{\partial \sigma_3^2} = \frac{\partial s_3}{\partial \sigma_3} = \frac{2}{3}$$

The first and second derivatives of J_3 with respect to the principal stresses are also required to develop equation 173. Recalling that, by definition:

$$J_3 = s_1 s_2 s_3 \tag{3}$$

Then:

$$\frac{\partial J_3}{\partial \sigma_1} = \frac{\partial s_1 s_2 s_3}{\partial s_1}\frac{\partial s_1}{\partial \sigma_1} + \frac{\partial s_1 s_2 s_3}{\partial s_2}\frac{\partial s_2}{\partial \sigma_1} + \frac{\partial s_1 s_2 s_3}{\partial s_3}\frac{\partial s_3}{\partial \sigma_1}$$

$$\frac{\partial J_3}{\partial \sigma_2} = \frac{\partial s_1 s_2 s_3}{\partial s_1}\frac{\partial s_1}{\partial \sigma_2} + \frac{\partial s_1 s_2 s_3}{\partial s_2}\frac{\partial s_2}{\partial \sigma_2} + \frac{\partial s_1 s_2 s_3}{\partial s_3}\frac{\partial s_3}{\partial \sigma_2} \tag{187}$$

$$\frac{\partial J_3}{\partial \sigma_3} = \frac{\partial s_1 s_2 s_3}{\partial s_1}\frac{\partial s_1}{\partial \sigma_3} + \frac{\partial s_1 s_2 s_3}{\partial s_2}\frac{\partial s_2}{\partial \sigma_3} + \frac{\partial s_1 s_2 s_3}{\partial s_3}\frac{\partial s_3}{\partial \sigma_3}$$

Additionally, because the values of the partial derivatives of the principal deviatoric stresses with respect to the principal stresses were previously determined in equation 181, equation 187 can be written as:

$$\frac{\partial J_3}{\partial \sigma_1} = s_2 s_3 \frac{2}{3} - s_1 s_3 \frac{1}{3} - s_1 s_2 \frac{1}{3} = s_2 s_3 - \frac{1}{3}(s_2 s_3 + s_1 s_3 + s_1 s_2)$$

$$\frac{\partial J_3}{\partial \sigma_1} = -s_2 s_3 \frac{1}{3} + s_1 s_3 \frac{2}{3} - s_1 s_2 \frac{1}{3} = s_1 s_3 - \frac{1}{3}(s_2 s_3 + s_1 s_3 + s_1 s_2) \tag{188}$$

$$\frac{\partial J_3}{\partial \sigma_1} = -s_2 s_3 \frac{1}{3} - s_1 s_3 \frac{1}{3} + s_1 s_2 \frac{2}{3} = s_1 s_2 - \frac{1}{3}(s_2 s_3 + s_1 s_3 + s_1 s_2)$$

Because:

$$-J_2 = s_2 s_3 + s_1 s_3 + s_1 s_2 \tag{189}$$

Then the first derivatives of J_3 may be written, using equation 188, as:

$$\frac{\partial J_3}{\partial \sigma_1} = s_2 s_3 + \frac{J_2}{3}$$

$$\frac{\partial J_3}{\partial \sigma_2} = s_1 s_3 + \frac{J_2}{3} \tag{190}$$

$$\frac{\partial J_3}{\partial \sigma_3} = s_1 s_2 + \frac{J_2}{3}$$

The second derivatives of J_3 are:

$$\frac{\partial^2 J_2}{\partial \sigma_1^2} = \frac{\partial s_2}{\partial \sigma_1} s_3 + s_2 \frac{\partial s_3}{\partial \sigma_1} + \frac{1}{3}\frac{\partial J_2}{\partial \sigma_1}$$

$$\frac{\partial^2 J_2}{\partial \sigma_2^2} = \frac{\partial s_1}{\partial \sigma_2} s_3 + s_1 \frac{\partial s_3}{\partial \sigma_2} + \frac{1}{3}\frac{\partial J_2}{\partial \sigma_2} \tag{191}$$

$$\frac{\partial^2 J_2}{\partial \sigma_3^2} = \frac{\partial s_1}{\partial \sigma_3} s_2 + s_1 \frac{\partial s_2}{\partial \sigma_3} + \frac{1}{3}\frac{\partial J_2}{\partial \sigma_3}$$

Again using the equation 181, and the first derivatives of J_2 from equation 185, the second derivatives of J_3 are:

$$\frac{\partial^2 J_2}{\partial \sigma_1^2} = \frac{1}{3}\left[- s_3 - s_2 + s_1\right]$$

$$\frac{\partial^2 J_2}{\partial \sigma_2^2} = \frac{1}{3}\left[- s_3 - s_1 + s_2\right] \tag{192}$$

$$\frac{\partial^2 J_2}{\partial \sigma_3^2} = \frac{1}{3}\left[- s_2 - s_1 + s_3\right]$$

Using equation 183 leads to:

$$\frac{\partial^2 J_2}{\partial \sigma_1^2} = \frac{1}{3}\left[-(- s_2 - s_1) - s_2 + s_1\right] = \frac{2}{3} s_1$$

$$\frac{\partial^2 J_2}{\partial \sigma_2^2} = \frac{1}{3}\left[-(- s_2 - s_1) - s_1 + s_2\right] = \frac{2}{3} s_2 \tag{193}$$

$$\frac{\partial^2 J_2}{\partial \sigma_3^2} = \frac{1}{3}\left[-(- s_3 - s_1) - s_1 + s_3\right] = \frac{2}{3} s_3$$

The second derivatives of f with respect to σ_1, σ_2, and σ_3 from equation 173 may now be written, substituting for the first and second derivatives of J_2 and second derivative of J_3, which are given by equations 185, 186, and 193:

$$\frac{\partial^2 f}{\partial \sigma_1^2} = \frac{\partial f}{\partial J_2}\frac{2}{3} + \left(\frac{\partial^2 f}{\partial J_2^2} s_1 + \frac{\partial^2 f}{\partial J_3 J_2}\frac{\partial J_3}{\partial \sigma_1}\right) s_1 + \frac{\partial f}{\partial J_3}\frac{2 s_1}{3} + \left(\frac{\partial^2 f}{\partial J_2 J_3} s_1 + \frac{\partial^2 f}{\partial J_3^2}\frac{\partial J_3}{\partial \sigma_1}\right)\frac{\partial J_3}{\partial \sigma_1}$$

$$\frac{\partial^2 f}{\partial \sigma_2^2} = \frac{\partial f}{\partial J_2}\frac{2}{3} + \left(\frac{\partial^2 f}{\partial J_2^2} s_2 + \frac{\partial^2 f}{\partial J_3 J_2}\frac{\partial J_3}{\partial \sigma_2}\right) s_2 + \frac{\partial f}{\partial J_3}\frac{2 s_2}{3} + \left(\frac{\partial^2 f}{\partial J_2 J_3} s_2 + \frac{\partial^2 f}{\partial J_3^2}\frac{\partial J_3}{\partial \sigma_2}\right)\frac{\partial J_3}{\partial \sigma_2} \tag{194}$$

$$\frac{\partial^2 f}{\partial \sigma_3^2} = \frac{\partial f}{\partial J_2}\frac{2}{3} + \left(\frac{\partial^2 f}{\partial J_2^2} s_3 + \frac{\partial^2 f}{\partial J_3 J_2}\frac{\partial J_3}{\partial \sigma_3}\right) s_3 + \frac{\partial f}{\partial J_3}\frac{2 s_3}{3} + \left(\frac{\partial^2 f}{\partial J_2 J_3} s_3 + \frac{\partial^2 f}{\partial J_3^2}\frac{\partial J_3}{\partial \sigma_3}\right)\frac{\partial J_3}{\partial \sigma_3}$$

The trace of the Hessian matrix, equation 171, is the sum of the three terms of equation 194:

$$trace(\boldsymbol{H}) = \frac{\partial^2 f}{\partial \sigma_1^2} + \frac{\partial^2 f}{\partial \sigma_2^2} + \frac{\partial^2 f}{\partial \sigma_3^2} = 2\frac{\partial f}{\partial J_2} + \frac{\partial^2 f}{\partial J_2^2}(s_1^2 + s_2^2 + s_3^2) + 2\frac{\partial^2 f}{\partial J_3 J_2}\left(\frac{\partial J_3}{\partial \sigma_1} s_1 + \frac{\partial J_3}{\partial \sigma_2} s_2 + \frac{\partial J_3}{\partial \sigma_3} s_3\right) +$$
$$2\frac{\partial f}{\partial J_3}(s_1 + s_2 + s_3) + \frac{\partial^2 f}{\partial J_3^2}\left(\left(\frac{\partial J_3}{\partial \sigma_1}\right)^2 + \left(\frac{\partial J_3}{\partial \sigma_2}\right)^2 + \left(\frac{\partial J_3}{\partial \sigma_3}\right)^2\right) \tag{195}$$

Note that using equation 8, the second term on the right side of the above equation 195 is:

$$\frac{\partial^2 f}{\partial J_2^2}(s_1^2 + s_2^2 + s_3^2) = \frac{\partial^2 f}{\partial J_2^2}(2 J_2) \tag{196}$$

Consider the third term on the right side of equation 195. Using equation 190 for the first derivatives of J_3 with respect to the principal stresses, the third term may be written as:

$$\left(\frac{\partial J_3}{\partial \sigma_1}s_1 + \frac{\partial J_3}{\partial \sigma_2}s_2 + \frac{\partial J_3}{\partial \sigma_3}s_3\right) = \left(s_2s_3 + \frac{J_2}{3}\right)s_1 + \left(s_1s_3 + \frac{J_2}{3}\right)s_2 + \left(s_1s_2 + \frac{J_2}{3}\right)s_3 \quad (197)$$

Regrouping equation 197 leads to:

$$\left(s_2s_3 + \frac{J_2}{3}\right)s_1 + \left(s_1s_3 + \frac{J_2}{3}\right)s_2 + \left(s_1s_2 + \frac{J_2}{3}\right)s_3 = 3(s_1s_2s_3) + \frac{J_2}{3}(s_1 + s_2 + s_3) \quad (198)$$

Recalling equation 3, by definition, $J_3 = s_1s_2s_3$ and that $s_1 + s_2 + s_3 = 0$ (equation 183), leads to:

$$\left(\frac{\partial J_3}{\partial \sigma_1}s_1 + \frac{\partial J_3}{\partial \sigma_2}s_2 + \frac{\partial J_3}{\partial \sigma_3}s_3\right) = 3(s_1s_2s_3) + \frac{J_2}{3}(s_1 + s_2 + s_3) = 3J_3 \quad (199)$$

Note that by equation 183, the fourth term on the right side of equation 195 is zero. Considering the fifth term on the right side of equation 195 and equation 190:

$$\left(\left(\frac{\partial J_3}{\partial \sigma_1}\right)^2 + \left(\frac{\partial J_3}{\partial \sigma_2}\right)^2 + \left(\frac{\partial J_3}{\partial \sigma_3}\right)^2\right) = \left(s_2s_3 + \frac{J_2}{3}\right)^2 + \left(s_1s_3 + \frac{J_2}{3}\right)^2 + \left(s_1s_2 + \frac{J_2}{3}\right)^2 = s_2^2s_3^2 + s_1^2s_3^2 + s_1^2s_2^2 + 2\left(\frac{J_2}{3}\right)(s_2s_3 + s_1s_3 + s_1s_2) + 3\left(\frac{J_2}{3}\right)^2 \quad (200)$$

Using equation 189, $-J_2 = s_2s_3 + s_1s_3 + s_1s_2$, and:

$$s_2^2s_3^2 + s_1^2s_3^2 + s_1^2s_2^2 = J_2^2 \quad (201)$$

Equation 200 may be written as:

$$\left(\left(\frac{\partial J_3}{\partial \sigma_1}\right)^2 + \left(\frac{\partial J_3}{\partial \sigma_2}\right)^2 + \left(\frac{\partial J_3}{\partial \sigma_3}\right)^2\right) = J_2^2 + 2\left(\frac{J_2}{3}\right)(-J_2) + \frac{{J_2}^2}{3} = \frac{2{J_2}^2}{3} \quad (202)$$

Equation 195 may now be rewritten, using equations 196, 199, and 202 as:

$$trace(\boldsymbol{H}) = \frac{\partial^2 f}{\partial \sigma_1^2} + \frac{\partial^2 f}{\partial \sigma_2^2} + \frac{\partial^2 f}{\partial \sigma_3^2} = 2\frac{\partial f}{\partial J_2} + \frac{\partial^2 f}{\partial J_2^2}(2J_2) + 2\frac{\partial^2 f}{\partial J_3 J_2}(3J_3) + \frac{\partial^2 f}{\partial J_3^2}\left(\frac{2{J_2}^2}{3}\right) \quad (203)$$

Now, considering the specific yield function of the GYS model, equation 134 can be written as:

$$f = c_1\sqrt{3}J_2^{1/2} + c_2\frac{9J_3}{2J_2} + c_3\frac{27\sqrt{3}J_3^2}{4J_2^{5/2}} - \sigma_y \quad (204)$$

The required derivatives of the GYS yield function to solve equation 203 are $\frac{\partial f}{\partial J_2}$, $\frac{\partial^2 f}{\partial J_2^2}$, $\frac{\partial^2 f}{\partial J_2 J_3}$, and $\frac{\partial^2 f}{\partial J_3^2}$; they are given in the following equations. Beginning by differentiating equation 204 with respect to J_2:

$$\frac{\partial f}{\partial J_2} = c_1\frac{\sqrt{3}}{2J_2^{1/2}} - c_2\frac{9J_3}{2J_2^2} - c_3\frac{5}{2}\frac{27\sqrt{3}J_3^2}{4J_2^{7/2}} \quad (205)$$

and then differentiating again with respect to J_2:

$$\frac{\partial^2 f}{\partial J_2^2} = -c_1 \frac{\sqrt{3}}{4J_2^{3/2}} + 2c_2 \frac{9J_3}{2J_2^3} + 35c_3 \frac{27\sqrt{3}J_3^2}{16J_2^{9/2}} \tag{206}$$

This specific term is not in equation 203, but it required determining the second derivative with respect to J_3:

$$\frac{\partial f}{\partial J_3} = c_2 \frac{9}{2J_2} + c_3 \frac{27\sqrt{3}J_3}{2J_2^{5/2}} \tag{207}$$

and then differentiating again with respect to J_3,

$$\frac{\partial^2 f}{\partial J_3^2} = c_3 \frac{27\sqrt{3}}{2J_2^{5/2}} \tag{208}$$

Finally, differentiating equation 205 with respect to J_3:

$$\frac{\partial^2 f}{\partial J_2 J_3} = -c_2 \frac{9}{2J_2^2} - c_3 \frac{5}{2} \frac{27\sqrt{3}J_3}{2J_2^{7/2}} \tag{209}$$

Making the summation of equation 203:

$$\frac{\partial^2 f}{\partial \sigma_1^2} + \frac{\partial^2 f}{\partial \sigma_2^2} + \frac{\partial^2 f}{\partial \sigma_3^2} = 2\left(c_1 \frac{\sqrt{3}}{2J_2^{1/2}} - c_2 \frac{9J_3}{2J_2^2} - c_3 \frac{5}{2} \frac{27\sqrt{3}J_3^2}{4J_2^{7/2}}\right) + \left(-c_1 \frac{\sqrt{3}}{4J_2^{3/2}} + 2c_2 \frac{9J_3}{2J_2^3} + 35c_3 \frac{27\sqrt{3}J_3^2}{16J_2^{9/2}}\right)(2J_2) + 2\left(-c_2 \frac{9}{2J_2^2} - c_3 \frac{5}{2} \frac{27\sqrt{3}J_3}{2J_2^{7/2}}\right)(3J_3) + \left(c_3 \frac{27\sqrt{3}}{2J_2^{5/2}}\right)\left(\frac{2{J_2}^2}{3}\right) \tag{210}$$

Simplifying and grouping the material coefficients and terms, which may be substituted for by the Lode Parameter, $cos3\vartheta = \frac{27J_3}{2\sigma_{vm}^3} = \frac{27J_3}{(2)(3\sqrt{3})J_2^{3/2}} = \frac{3\sqrt{3}J_3}{2J_2^{3/2}}$,

$$\frac{\partial^2 f}{\partial \sigma_1^2} + \frac{\partial^2 f}{\partial \sigma_2^2} + \frac{\partial^2 f}{\partial \sigma_3^2} = \frac{c_1\sqrt{3}}{2\sqrt{J_2}} + \frac{c_3 9\sqrt{3}}{\sqrt{J_2}} - \frac{c_2 4\sqrt{3}}{\sqrt{J_2}}\left(\frac{3\sqrt{3}J_3}{2J_2^{3/2}}\right) - \frac{c_3 35\sqrt{3}}{2\sqrt{J_2}}\left(\frac{3\sqrt{3}J_3}{2J_2^{3/2}}\right)^2 \tag{211}$$

The first convexity condition of the Hessian matrix trace being positive or zero, in terms of the Lode parameter may now be written:

$$trace(\boldsymbol{H}) = \frac{\partial^2 f}{\partial \sigma_1^2} + \frac{\partial^2 f}{\partial \sigma_2^2} + \frac{\partial^2 f}{\partial \sigma_3^2} \geq 0 \longrightarrow$$
$$\frac{c_1\sqrt{3}}{2\sqrt{J_2}} + \frac{c_3(2)9\sqrt{3}}{2\sqrt{J_2}} - \frac{c_2(2)4\sqrt{3}}{2\sqrt{J_2}} cos3\vartheta - \frac{c_3 35\sqrt{3}}{2\sqrt{J_2}}(cos3\vartheta)^2 \geq 0 \tag{212}$$

Equation 212 may be simplified further by noting that a common term of $\frac{\sqrt{3}}{2\sqrt{J_2}}$ exists in each of its terms, and that $\frac{\sqrt{3}}{2\sqrt{J_2}} \geq 0$:

$$c_1 + 18c_3 - 8c_2(cos3\vartheta) - 35c_3(cos3\vartheta)^2 \geq 0 \tag{213}$$

The second convexity condition is that sum of principal minors of Hessian matrix is positive or zero:

$$M_1 + M_2 + M_3 \geq 0 \tag{214}$$

The derivation of the second convexity condition is more complex than that of the first convexity condition, which has been shown in equations 171–213. The derivation of the second convexity condition was performed using MATHEMATICA v8 symbolic calculation toolbox, and it is summarized in appendix A (the first convexity condition derivation was also confirmed using MATHEMATICA). The results of second convexity condition derivation, as shown in appendix A, was that $M_1 + M_2 + M_3$ is always equal to zero with the GYS yield function:

$$M_1 + M_2 + M_3 = 0 \tag{A.29}$$

Therefore, the condition $M_1 + M_2 + M_3 \geq 0$ is always satisfied, and the only convexity condition that requires checking in the GYS model is the first convexity condition.

3.7.2 Regions of Convexity in the GYS Model

Recall that for there to be a unique solution in the plasticity analysis, convexity of the yield surface is a requirement. In the previous section, a condition which, if satisfied, ensures convexity was derived. This convexity condition, equation 213, the first convexity condition, was written in terms of the GYS material coefficients (hardening parameters) c_1, c_2, and c_3, and the Lode parameter $cos3\vartheta$. Recall that the GYS material coefficients c_1, c_2 and c_3 were summarized in equation 116:

$$\sigma_{vm} = \sigma_y = \sigma_t$$
$$c_1 + c_2 + c_3 = 1, c_1 - c_2 + c_3 = \frac{\sigma_t}{\sigma_c},\ c_1 = \frac{\sigma_t}{\sqrt{3}\sigma_s}$$

For the yield function to be convex, these parameters will need to be limited to a given numerical range. For convenience in visualization, the GYS material coefficients c_1, c_2, and c_3 can also be expressed in terms of pure-shear yield stress relative to uni-axial tension yield stress $\left(\frac{\sigma_s}{\sigma_t}\right)$ and uni-axial compression yield stress relative to uni-axial tension yield stress $\left(\frac{\sigma_c}{\sigma_t}\right)$:

$$c_1 = \frac{1}{\frac{\sigma_s}{\sigma_t}\sqrt{3}},\ c_2 = \frac{1}{2}\left(1 - \frac{1}{\frac{\sigma_c}{\sigma_t}}\right),\ c_3 = 1 - c_1 - c_2$$
$$c_3 = 1 - \frac{1}{\frac{\sigma_s}{\sigma_t}\sqrt{3}} - \frac{1}{2}\left(1 - \frac{1}{\frac{\sigma_c}{\sigma_t}}\right) = \frac{1}{2} - \frac{1}{\frac{\sigma_s}{\sigma_t}\sqrt{3}} + \frac{1}{\frac{\sigma_c}{\sigma_t}} \tag{215}$$

The first convexity condition, equation 213, may then be written in terms of three parameters: uni-axial compression yield relative to uni-axial tension yield $\left(\frac{\sigma_c}{\sigma_t}\right)$, pure-shear yield relative to uni-axial tension yield $\left(\frac{\sigma_s}{\sigma_t}\right)$, and the Lode parameter $cos3\vartheta$:

$$\left(\frac{1}{\frac{\sigma_S}{\sigma_t}\sqrt{3}}\right) + 18\left(\frac{1}{2} - \frac{1}{\frac{\sigma_S}{\sigma_t}\sqrt{3}} + \frac{1}{\frac{\sigma_C}{\sigma_t}}\right) - 4\left(1 - \frac{1}{\frac{\sigma_C}{\sigma_t}}\right)(cos3\vartheta) - 35\left(\frac{1}{2} - \frac{1}{\frac{\sigma_S}{\sigma_t}\sqrt{3}} + \frac{1}{\frac{\sigma_C}{\sigma_t}}\right)(cos3\vartheta)^2 \geq 0 \tag{216}$$

To further aid in visualization, the yield stress in tension is set equal to unity to normalize the stress ratios. Then:

$$\sigma_{vm} = \sigma_t = 1 \longrightarrow J_2 = \frac{\sigma_t^2}{3} = \frac{1}{3} \tag{217}$$

Note that the Lode parameter represents the state of stress and is always limited to between -1 and 1. For a solution to be guaranteed for all states of stress, the convexity condition should be fulfilled for all Lode parameters. Using the normalized tension yield stress shown in equation 217, equation 216 was plotted along three axes, the variables being the Lode parameter, the ratio of the yield in pure-shear to the yield in uni-axial tension, and the ratio of the yield in uni-axial compression to the yield in uni-axial tension. The range of convexity of the GYS model was obtained and is shown in figures 28 and 29. The region of convexity is shown as a solid color in these figures.

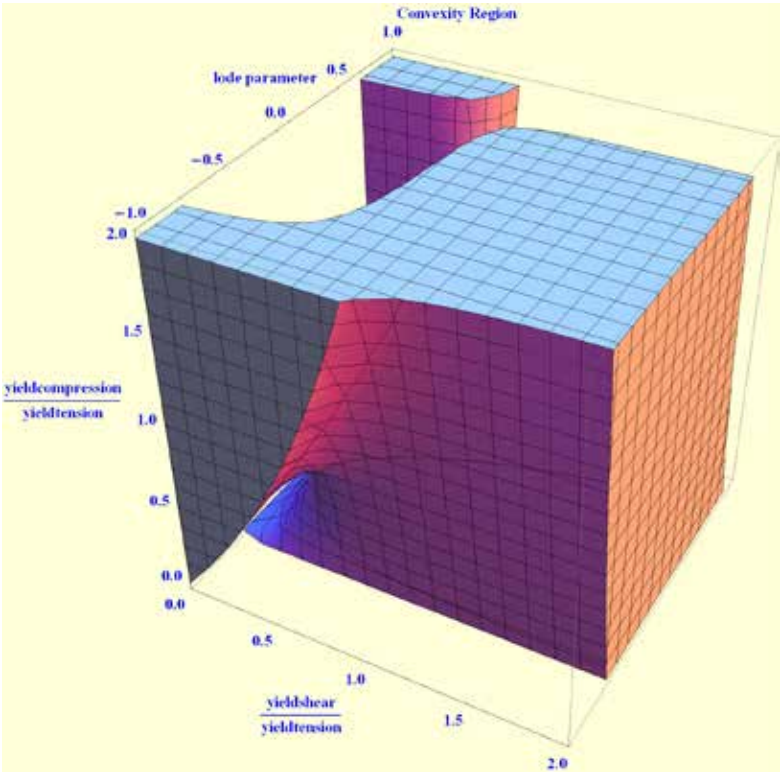

Figure 28. Convexity region of the GYS model in terms of the ratios of uni-axial compression to tension and pure-shear to uni-axial tension, and Lode parameter

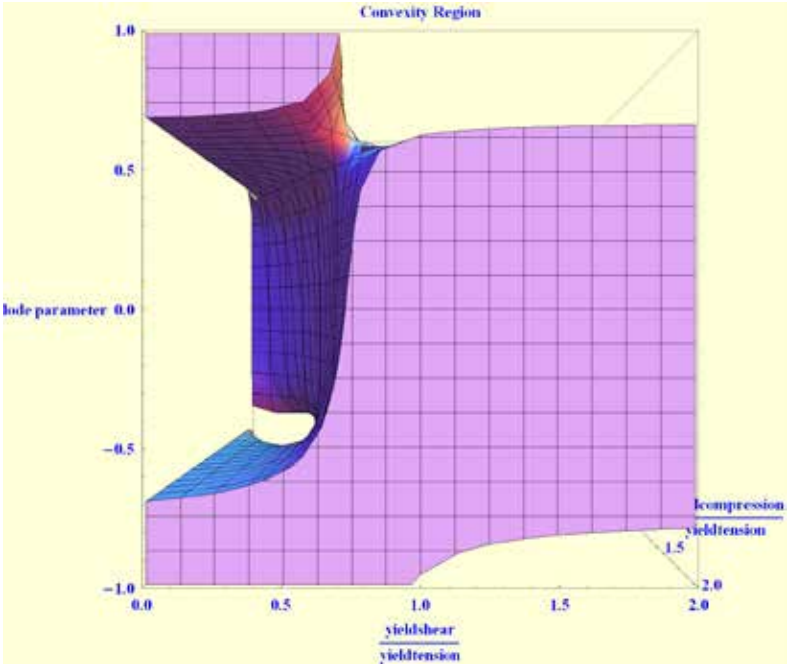

Figure 29. Convexity region of the GYS model in terms of the ratios of uni-axial compression to tension and pure-shear to uni-axial tension, and Lode parameter

To better demonstrate the specific ranges of convexity, the regions of convexity for specific uni-axial compression to tension yield stress ratios are shown in figures 30–40. These plots are cross sections of three-dimensional convexity region shown in figures 28–29. Figure 30 shows convexity for a uni-axial compression to tension yield ratio equal to 1. Figure 30 also shows that convexity only occurs for all Lode parameters when the pure-shear to uni-axial tension yield ratio is between 0.545 and 0.611 (dashed lines in the figure).

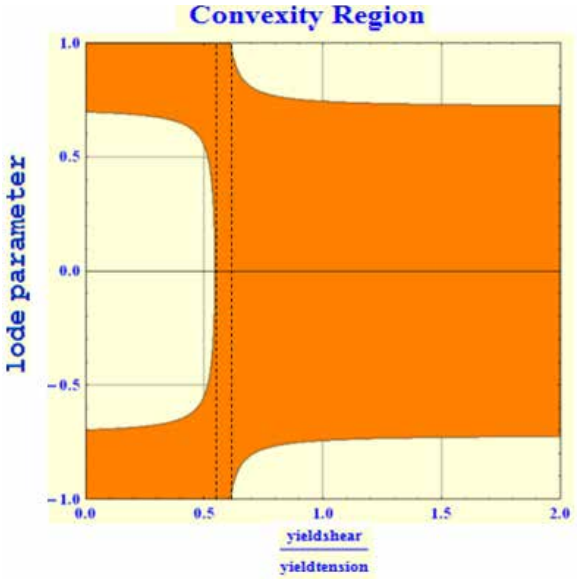

Figure 30. Convexity region of GYS model with yield ratio uni-axial compression/uni-axial tension = 1 with dashed lines showing pure-shear yield to uni-axial tension yield ratios of 0.545 and 0.611

In the von Mises plasticity, the uni-axial compression to tension yield ratio is 1, and the pure-shear to uni-axial tension yield ratio is fixed to a value 0.577. Therefore, the GYS model can represent cases of pure-shear yield to uni-axial tension ratios for all Lode parameters for approximately ± 5% more than the fixed pure-shear yield ratio of the von Mises plasticity.

Figures 31–33 present cases in which the uni-axial compression yield is less than the uni-axial tension yield. In figure 31, in which the uni-axial compression to uni-axial tension yield ratio equals 0.95, convexity for all Lode parameters is guaranteed only when the pure-shear to uni-axial tension yield ratio is between 0.531 and 0.588.

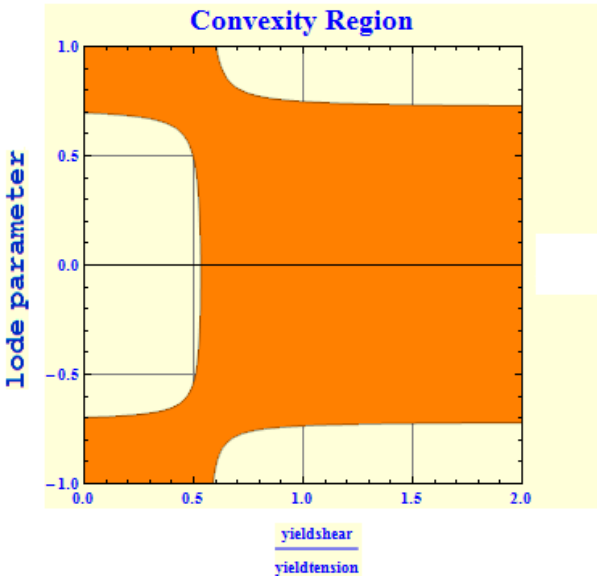

Figure 31. Convexity region of GYS model with yield ratio compression/tension = 0.95

In figure 32, in which the uni-axial compression to uni-axial tension yield ratio equals 0.75, convexity for all Lode parameters is guaranteed only when the pure-shear to uni-axial tension yield ratio is between 0.467 and 0.490.

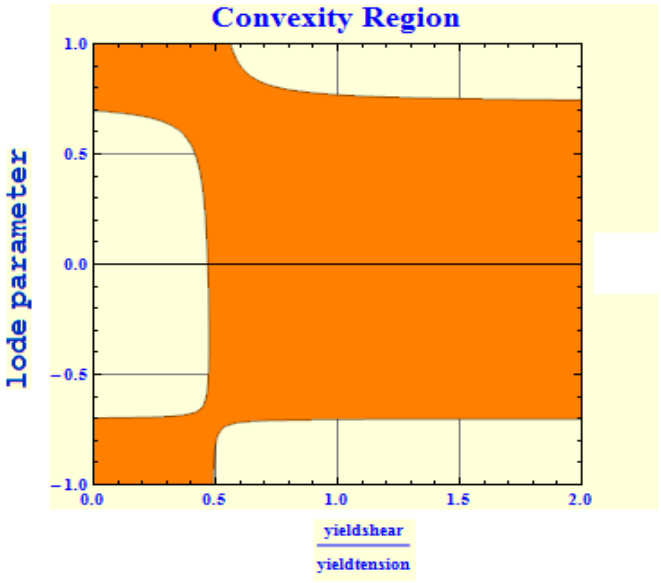

Figure 32. Convexity region of GYS model with yield ratio compression/tension = 0.75

The minimum value for which there is a convexity region for all Lode parameters is a uni-axial compression to uni-axial tension yield ratio equal to 0.590. For this compression to tension ratio, the only convex pure-shear to uni-axial tension yield ratio is 0.405. Consider the case in which the uni-axial compression to uni-axial tension yield ratio equals 0.5. This is lower than the minimum ratio of 0.590 in which convexity is guaranteed for all states-of-stress. As shown in figure 33, there is no region that is convex for all Lode parameters. In the GYS implementation, when uni-axial

compression to uni-axial tension yield ratios lower than 0.590 occur, the compression yield (and therefore the yield ratio) is projected to the minimum guaranteed convexity ratio of 0.590.

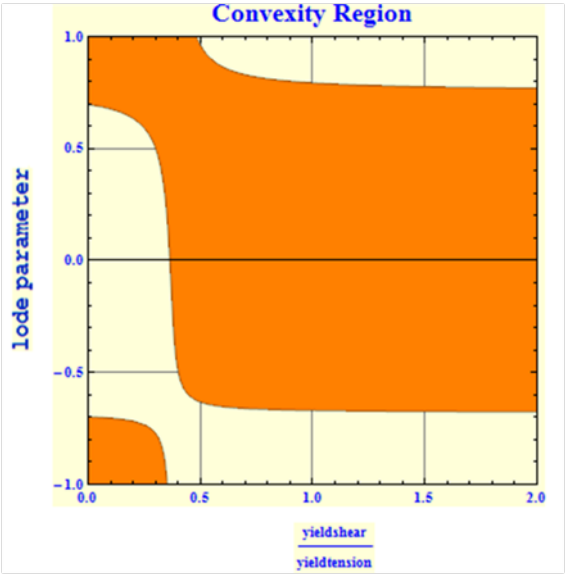

Figure 33. Convexity region of GYS model with yield ratio uni-axial compression/tension = 0.50

Figures 34–36 present cases in which the uni-axial compression yield is greater than the uni-axial tension yield. In figure 34, in which the uni-axial compression to uni-axial tension yield ratio equals 1.1, convexity for all Lode parameters is guaranteed only when the pure-shear to uni-axial tension yield ratio is between 0.571 and 0.626.

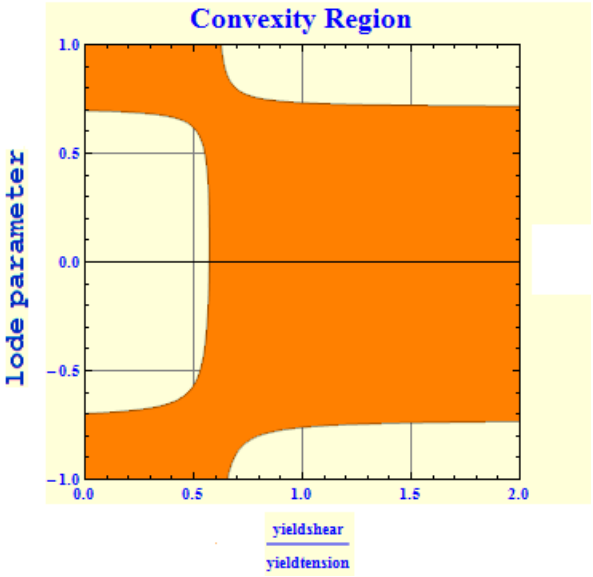

Figure 34. Convexity region of GYS model with yield ratio compression/tension = 1.1

In figure 35, in which the uni-axial compression to uni-axial tension yield ratio equals 1.25, convexity for all Lode parameters is guaranteed only when the pure-shear to uni-axial tension yield ratio is between 0.605 and 0.645.

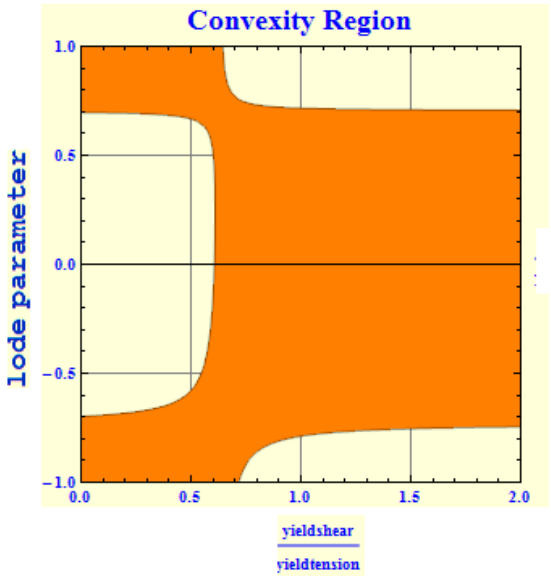

Figure 35. Convexity region of GYS model with yield ratio compression/tension = 1.25

The maximum value for which there is a convexity region for all Lode parameters is a uni-axial compression to uni-axial tension yield ratio equal to 1.693. For this compression to tension ratio, the only convex pure-shear to uni-axial tension yield ratio is 0.685. Consider the case in which the uni-axial compression to uni-axial tension yield ratio equals 2.0. This is higher than the maximum ratio of 1.693, in which convexity is guaranteed for all states of stress. As shown in figure 36, there is no region that is convex for all Lode parameters. In the GYS implementation, when uni-axial compression to uni-axial tension yield ratios higher than 1.693 occur, the compression yield (and therefore the yield ratio) is projected to the maximum guaranteed convexity ratio of 1.693.

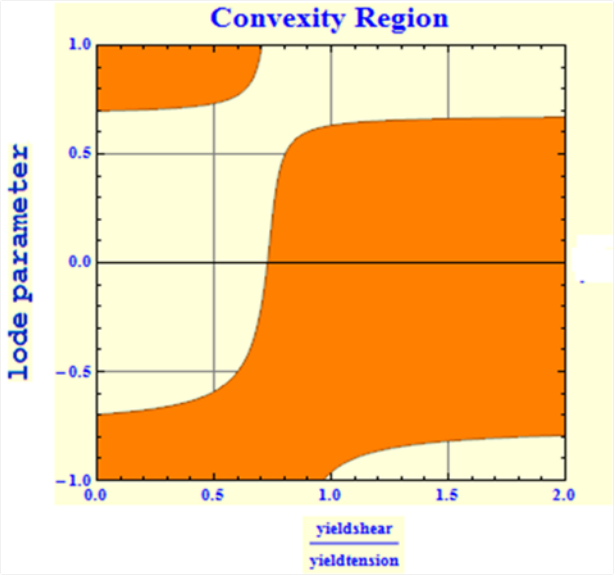

Figure 36. Convexity region of GYS model with yield ratio uni-axial compression/tension = 2.00

3.7.3 Comparisons to the Convexity of Other Models

The programmed equations of the first and second convexity conditions, which were derived in the previous section, were verified by comparing results to previously published yield models. The von Mises, Drucker, and Cazacu-Barlat yield functions have known convexity conditions, as shown in table 2. The recovered yield functions were generated in the GYS model using the method presented in section 3.6. The programmed GYS output has reproduced the convexity conditions of these yield functions.

Table 2. Comparison of convexity ranges of von Mises, Cazacu-Barlat, and Drucker models

Yield Criterion	Yield Function	Convexity Range
von Mises	$J_2^{1/2} = \tau$	No condition (convex at all points)
Cazacu-Barlat	$J_2^{3/2} - cJ_3 = \tau^3$	$\frac{-3\sqrt{3}}{4} < c < \frac{3\sqrt{3}}{4}$
Drucker	$J_2^3 - cJ_3^2 = \tau^6$	$\frac{-27}{8} < c < \frac{9}{4}$

(τ: yield stress in pure-shear)

In figure 37, the convexity region of the GYS yield surface is shown with $\sqrt{3}$ times the ratio of the pure-shear yield stress to the uni-axial tension yield stress as the abscissa (the $\sqrt{3}$ factor is used on the shear to tension ratio so that the von Mises ratio of shear yield stress to tension yield stress is plotted as 1). The ratio of the uni-axial compression yield stress to the uni-axial tension yield stress is the ordinate. Three curves of Lode parameters 1, 0, and -1 are shown, with the region of convexity being the region inside of all three curves. In addition, the possible stress ratios and convexity regions of von Mises, Drucker, and Cazacu-Barlat yield functions are shown.

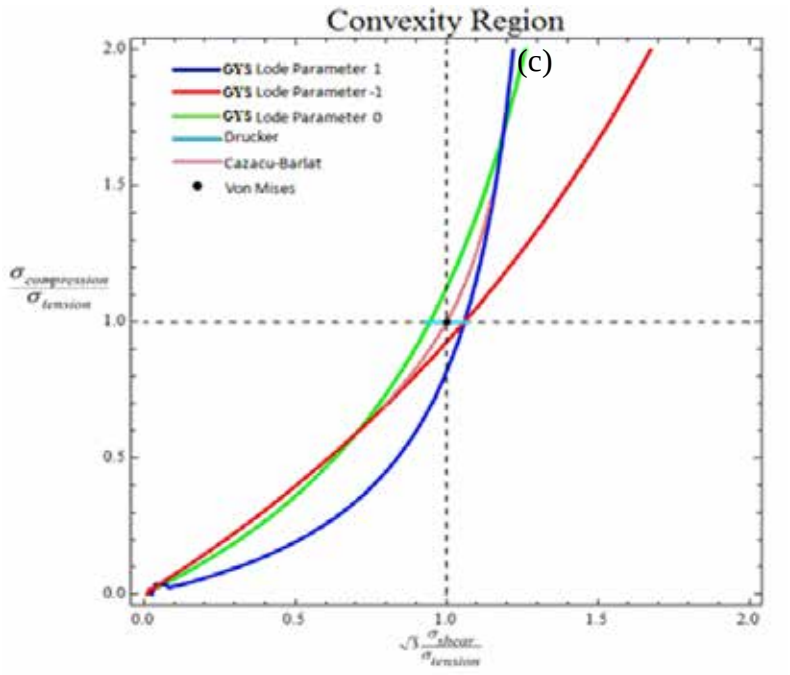

Figure 37. Intersection of the Lode angle parameter (θ) curves corresponding to 0, 1, -1 for the GYS model

Figure 38 shows the same information as figure 37, except that the region inside of the three Lode parameters curves from the GYS model is emphasized by truncating the curves at the intersection of their limits. Numerical values of the minimum and maximum limits of the GYS convexity region are also shown in figure 38. In addition, the minimum and maximum limit values of convexity of the ratio of pure-shear to uni-axial tension yield, with the ratio of uni-axial compression to uni-axial tension of 1 $\left(\frac{\sigma_c}{\sigma_t} = 1\right)$ shown. Again, note that the abscissa is $\sqrt{3}$ times the ratio of the pure-shear yield stress to the uni-axial tension yield stress.

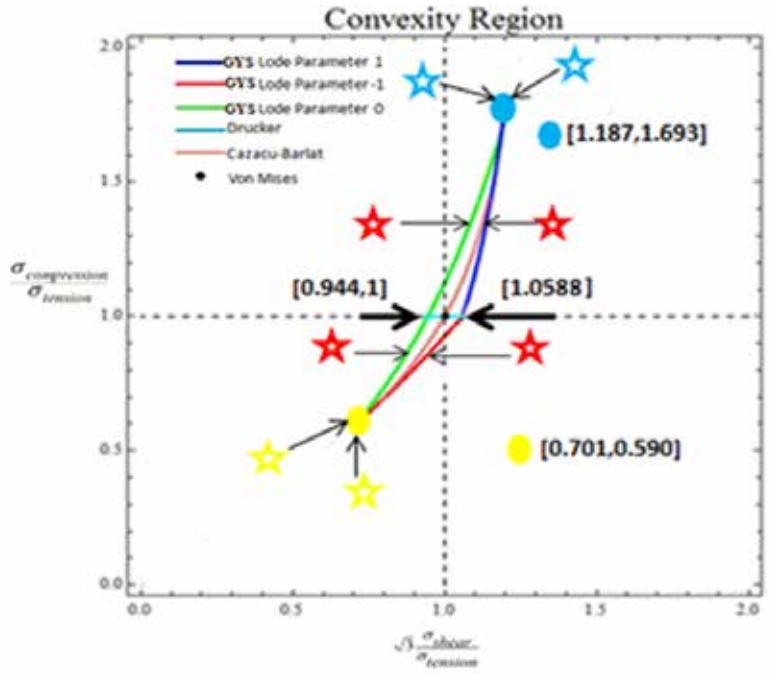

Figure 38. Comparison of the convexity regions of the GYS model and von Mises, Drucker, and Cazacu-Barlat models, including limits of the convexity region of the GYS model

In figure 38, the von Mises convexity region is a single point. This is because the von Mises model is limited to only these single yield stress ratio values. The Drucker convexity region is a single curve along the $\frac{\sigma_c}{\sigma_t} = 1$ line. This is also due to the limitations of possible yield stresses in the Drucker model. The Cazacu-Barlat convexity region is a single curve that runs through the GYS model minimum and maximum compression to tension convexity ratios. Note that the GYS convexity region is an area, and so provides more flexibility to match experimental data than the other models. A summary of the equations describing the convexity conditions of the Cazacu-Barlat, von Mises, and Drucker models is given in appendix A2.

3.8 Development of Convexity Algorithm for the GYS Model

In the previous section, the convexity region of the GYS model was presented as a function of the ratio of uni-axial compression yield stress to uni-axial tension yield stress $\left(\frac{\sigma_c}{\sigma_t}\right)$, and $\sqrt{3}$ times the ratio of pure-shear yield stress to uni-axial tension yield stress $\left(\frac{\sigma_s}{\sigma_t}\right)$. As presented in section 3.4, the yield stresses are based on experimental data. In the plasticity analysis, as the yield surface expands, the ratios are recomputed at each time step. If the ratio value is outside of the convexity region, a projection is made onto a convexity boundary. Then, one or both of the ratios are modified internally to satisfy the convexity requirement. As a result, the results from the GYS yield algorithm may not precisely match the experimental data.

The first step in convexity projection and modification algorithm is that the locations of the ratios are classified by comparison to minimum and maximum convexity of the uni-axial compression to uni-axial tension yield stress ratio $\left(\frac{\sigma_c}{\sigma_t}\right)$. If a ratio is greater than the compression to tension maximum convexity ratio, it is projected onto the maximum ratio (see light blue star in figure 38). If a ratio is less than the compression to tension maximum convexity ratio, then it is projected onto the minimum ratio (see yellow star in figure 38). If a ratio is between the compression to tension yield ratio minimum and maximum ratios but still outside the convexity region, it is projected along the shear to tension ratio axis onto the convexity region boundary (see red stars in figure 39).

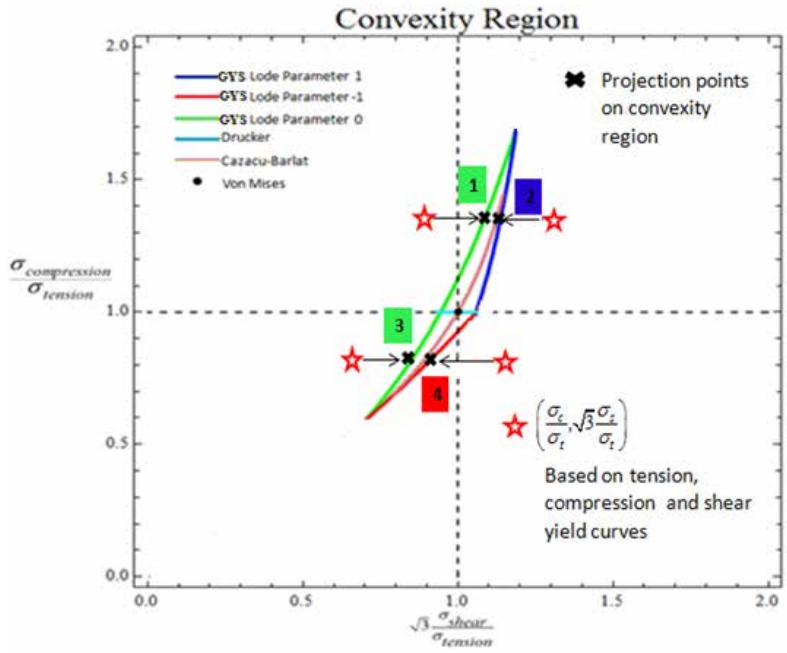

Figure 39. Projection operation of convexity algorithm of GYS model

A summary of the convexity algorithm is presented in section 3.8.1. The following variables are used in the algorithm summary:

$\frac{\sigma_c}{\sigma_t}$: Uni-axial compression to uni-axial tension yield ratio calculated at each time step.

$\frac{\sigma_s}{\sigma_t}$: Pure-shear to uni-axial tension yield ratio calculated at each time step.

$\frac{\sigma_c}{\sigma_t}(\boldsymbol{max})=\mathbf{1.693}$: Uni-axial compression to uni-axial tension yield ratio, maximum ratio of the convexity region.

$\frac{\sigma_c}{\sigma_t}(\boldsymbol{min})=\mathbf{0.590}$: Uni-axial compression to uni-axial tension yield ratio, minimum ratio of the convexity region.

$\sqrt{3}\frac{\sigma_s}{\sigma_t}(1)$, $\sqrt{3}\frac{\sigma_s}{\sigma_t}(2)$: Projection points on the convexity boundary when $\frac{\sigma_c}{\sigma_t}$ is between $\frac{\sigma_c}{\sigma_t}(\boldsymbol{min})$ and $\frac{\sigma_c}{\sigma_t}(\boldsymbol{max})$ and $\frac{\sigma_c}{\sigma_t} \geq 1$ (see figure 39), and where (1) signifies that the shear to tension ratio is less than the convexity ratio limit, and (2) signifies that the shear to tension ratio is greater than the convexity boundary ratio limit.

Note the special case when $\frac{\sigma_c}{\sigma_t} = 1$, that $\sqrt{3}\frac{\sigma_s}{\sigma_t}(1) = 0.944$ and $\sqrt{3}\frac{\sigma_s}{\sigma_t}(2) = 1.0588$ (see figure 38).

$\sqrt{3}\frac{\sigma_s}{\sigma_t}(3)$, $\sqrt{3}\frac{\sigma_s}{\sigma_t}(4)$: Projection points on the convexity boundary when $\frac{\sigma_c}{\sigma_t}$ is between $\frac{\sigma_c}{\sigma_t}(\boldsymbol{min})$ and $\frac{\sigma_c}{\sigma_t}(\boldsymbol{max})$ and $\frac{\sigma_c}{\sigma_t} < 1$ (see figure 39), and where (3) signifies that the shear to tension ratio is less than the convexity ratio limit, and (4) signifies that the shear to tension ratio is greater than the convexity boundary ratio limit.

The convexity algorithm of the GYS model based on the variables given above is presented in section 3.8.1.

3.8.1 Convexity Algorithm of the GYS Model

(i)) *If $\frac{\sigma_c}{\sigma_t}$ is larger than $\frac{\sigma_c}{\sigma_t}(\boldsymbol{max})$ then it is projected to $\frac{\sigma_c}{\sigma_t}(\boldsymbol{max})$*

$\boldsymbol{IF}\frac{\sigma_c}{\sigma_t} \geq \frac{\sigma_c}{\sigma_t}(\boldsymbol{max})$ $\boldsymbol{THEN}\frac{\sigma_c}{\sigma_t} \rightarrow \frac{\sigma_c}{\sigma_t}(\boldsymbol{max})$(ii) *If $\frac{\sigma_c}{\sigma_t}$ is less than $\frac{\sigma_c}{\sigma_t}(\boldsymbol{min})$ then it is projected to $\frac{\sigma_c}{\sigma_t}(\boldsymbol{min})$*

$\boldsymbol{IF}\frac{\sigma_c}{\sigma_t} \leq \frac{\sigma_c}{\sigma_t}(\boldsymbol{min})$ $\boldsymbol{THEN}\frac{\sigma_c}{\sigma_t} \rightarrow \frac{\sigma_c}{\sigma_t}(\boldsymbol{min})$

(iii) *If $\frac{\sigma_c}{\sigma_t}$ is between $\frac{\sigma_c}{\sigma_t}(\boldsymbol{min})$* and $\frac{\sigma_c}{\sigma_t}(\boldsymbol{max})$ *and $\frac{\sigma_c}{\sigma_t} \geq 1$ then compute $\sqrt{3}\frac{\sigma_s}{\sigma_t}(1)$ at point 1 and $\sqrt{3}\frac{\sigma_s}{\sigma_t}(2)$ at point 2 (see figure 39)*

$\boldsymbol{IF}\frac{\sigma_c}{\sigma_t}(\boldsymbol{min}) < \frac{\sigma_c}{\sigma_t} < \frac{\sigma_c}{\sigma_t}(\boldsymbol{max})$ $\boldsymbol{AND}\frac{\sigma_c}{\sigma_t} \geq 1$

$\boldsymbol{COMPUTE}\sqrt{3}\frac{\sigma_s}{\sigma_t}(1), \sqrt{3}\frac{\sigma_s}{\sigma_t}(2)$

(iii-a) *If $\sqrt{3}\frac{\sigma_s}{\sigma_t}$ is less than $\sqrt{3}\frac{\sigma_s}{\sigma_t}(1)$ then it is projected to $\sqrt{3}\frac{\sigma_s}{\sigma_t}(1)$*

IF $\sqrt{3}\frac{\sigma_s}{\sigma_t} \leq \sqrt{3}\frac{\sigma_s}{\sigma_t}(1)$ ***THEN*** $\sqrt{3}\frac{\sigma_s}{\sigma_t} \rightarrow \sqrt{3}\frac{\sigma_s}{\sigma_t}(1)$(iii-b) *If* $\sqrt{3}\frac{\sigma_s}{\sigma_t}$ *is greater than* $\sqrt{3}\frac{\sigma_s}{\sigma_t}(2)$ *then it is projected to* $\sqrt{3}\frac{\sigma_s}{\sigma_t}(2)$

IF $\sqrt{3}\frac{\sigma_s}{\sigma_t} \geq \sqrt{3}\frac{\sigma_s}{\sigma_t}(2)$ ***THEN*** $\sqrt{3}\frac{\sigma_s}{\sigma_t} \rightarrow \sqrt{3}\frac{\sigma_s}{\sigma_t}(2)$

(iii-c) *If* $\sqrt{3}\frac{\sigma_s}{\sigma_t}$ *is between* $\sqrt{3}\frac{\sigma_s}{\sigma_t}(1)$ *and* $\sqrt{3}\frac{\sigma_s}{\sigma_t}(2)$ *then it is inside the convexity region and no projection is made.*

IF $\sqrt{3}\frac{\sigma_s}{\sigma_t}(1) < \sqrt{3}\frac{\sigma_s}{\sigma_t} < \sqrt{3}\frac{\sigma_s}{\sigma_t}(2)$ ***THEN*** $\sqrt{3}\frac{\sigma_s}{\sigma_t} \rightarrow \sqrt{3}\frac{\sigma_s}{\sigma_t}$

(iv) *If* $\frac{\sigma_c}{\sigma_t}$ *is between* $\frac{\sigma_c}{\sigma_t}$ $(\boldsymbol{min})$ and $\frac{\sigma_c}{\sigma_t}$ $(\boldsymbol{max})$ *and* $\frac{\sigma_c}{\sigma_t} < 1$ *then compute* $\sqrt{3}\frac{\sigma_s}{\sigma_t}(3)$ *at point 3 and* $\sqrt{3}\frac{\sigma_s}{\sigma_t}(4)$ *at point 4 (see figure 39)*

IF $\frac{\sigma_c}{\sigma_t}$ $(\boldsymbol{min}) < \frac{\sigma_c}{\sigma_t} < \frac{\sigma_c}{\sigma_t}$ $(\boldsymbol{max})$ ***AND*** $\frac{\sigma_c}{\sigma_t} < 1$

COMPUTE $\sqrt{3}\frac{\sigma_s}{\sigma_t}(3), \sqrt{3}\frac{\sigma_s}{\sigma_t}(4)$

(iv-a) *If* $\sqrt{3}\frac{\sigma_s}{\sigma_t}$ *is less than* $\sqrt{3}\frac{\sigma_s}{\sigma_t}(3)$ *then it is projected to* $\sqrt{3}\frac{\sigma_s}{\sigma_t}(3)$

IF $\sqrt{3}\frac{\sigma_s}{\sigma_t} \leq \sqrt{3}\frac{\sigma_s}{\sigma_t}(3)$ ***THEN*** $\sqrt{3}\frac{\sigma_s}{\sigma_t} \rightarrow \sqrt{3}\frac{\sigma_s}{\sigma_t}(3)$

(iv-b) *If* $\sqrt{3}\frac{\sigma_s}{\sigma_t}$ *is greater than* $\sqrt{3}\frac{\sigma_s}{\sigma_t}(4)$ *then it is projected to* $\sqrt{3}\frac{\sigma_s}{\sigma_t}(4)$

IF $\sqrt{3}\frac{\sigma_s}{\sigma_t} \geq \sqrt{3}\frac{\sigma_s}{\sigma_t}(4)$ ***THEN*** $\sqrt{3}\frac{\sigma_s}{\sigma_t} \rightarrow \sqrt{3}\frac{\sigma_s}{\sigma_t}(4)$

(iv-c) *If* $\sqrt{3}\frac{\sigma_s}{\sigma_t}$ *is between* $\sqrt{3}\frac{\sigma_s}{\sigma_t}(3)$ *and* $\sqrt{3}\frac{\sigma_s}{\sigma_t}(4)$ *then it is inside the convexity region and no projection is made.*

IF $\sqrt{3}\frac{\sigma_s}{\sigma_t}(3) < \sqrt{3}\frac{\sigma_s}{\sigma_t} < \sqrt{3}\frac{\sigma_s}{\sigma_t}(4)$ ***THEN*** $\sqrt{3}\frac{\sigma_s}{\sigma_t} \rightarrow \sqrt{3}\frac{\sigma_s}{\sigma_t}$

Numerical verification cases of the convexity correction, using the projection onto convexity region boundary, are presented in section 4. Note that only the ratio $\frac{\sigma_s}{\sigma_t}$**,** and, therefore, the shear

yield stress, will be modified during the projection operation, if the $\frac{\sigma_c}{\sigma_t}$ ratio is located between minimum and maximum convexity ratios of $\frac{\sigma_c}{\sigma_t}$. As shown in figure 39, $\frac{\sigma_c}{\sigma_t}$ is not modified in this circumstance. If the $\frac{\sigma_c}{\sigma_t}$ ratio is less than the minimum or greater than the maximum ratios of the convexity region, both the $\frac{\sigma_c}{\sigma_t}$ and $\frac{\sigma_s}{\sigma_t}$ ratios, and, therefore, the compression and shear yield stresses, will be modified during the projection operation.

It is assumed that experimental yield curves in uni-axial tension, uni-axial compression, and pure-shear are available for the material for which a GYS model is being created. Review of the $\frac{\sigma_c}{\sigma_t}$ and $\frac{\sigma_s}{\sigma_t}$ ratios during the material model creation and verification, to understand if the given yield stress ratios are inside or outside of the convexity region, is strongly suggested. This review will make it clear if there are modifications being made to the $\frac{\sigma_c}{\sigma_t}$ or $\frac{\sigma_s}{\sigma_t}$ ratios due to projection onto a convexity boundary. Modification of the ratios leads to a change in the analytical compression or shear yield stress results.

3.9 Numerical Implementation of the GYS Model

In this section, the numerical implementation of the GYS model is presented. Implementation of the temperature dependency of material properties is presented first. Next, the Kuhn-Tucker conditions for GYS are described. The general procedure to integrate the plastic rate equation is then reviewed. The procedure of implementing material constitutive models into the commercial finite element package LS-DYNA is then presented.

3.9.1 Tabulated Input of Temperature and Rate Dependency

Temperature and rate dependency of a material may be included in a GYS material model by the use of tabulated input. The flow stresses of the GYS model can be formulated as a multiplicative decomposition of flow stress for strain rate and temperature dependency independently for the uni-axial tension, uni-axial compression, and pure-shear stresses as:

$$\begin{aligned} \sigma_t &= tr\left(\bar{\varepsilon}^p_{eff}, \dot{\bar{\varepsilon}}^p_{eff}\right) tt\left(\bar{\varepsilon}^p_{eff}, T\right), \bar{\varepsilon}^p_{eff} = \varepsilon^p_t \\ \sigma_c &= cr\left(\bar{\varepsilon}^p_{eff}, \dot{\bar{\varepsilon}}^p_{eff}\right) ct\left(\bar{\varepsilon}^p_{eff}, T\right), \bar{\varepsilon}^p_{eff} = \varepsilon^p_c \frac{\sigma_c}{\sigma_t} \\ \sigma_s &= sr\left(\bar{\varepsilon}^p_{eff}, \dot{\bar{\varepsilon}}^p_{eff}\right) st\left(\bar{\varepsilon}^p_{eff}, T\right), \bar{\varepsilon}^p_{eff} = \varepsilon^p_s \frac{\sigma_s}{\sigma_t} \end{aligned} \tag{218}$$

where $\bar{\varepsilon}^p_{eff}$ is the effective plastic strain, $\dot{\bar{\varepsilon}}^p_{eff}$ is the effective plastic strain rate, and T is the temperature. ε^p_t, ε^p_c, and ε^p_s are the true plastic strains in uni-axial tension, uni-axial compression, and pure-shear respectively. The yield stresses in uni-axial tension, uni-axial compression, and pure-shear are σ_t, σ_c, and σ_s. The functions *tr*, *cr*, and *sr* denote table input, which provides rate-dependent material properties. The functions *tt*, *ct*, and *st* denote table input, which provides temperature dependent material properties.

Tabulated inputs of strain-rate-dependent isothermal curves and temperature-dependent hardening curves can be provided directly as experimental curves using true stress-true plastic strain (IFLAG = 0 in the LS-DYNA implementation) in uni-axial tension (ε_t^p), uni-axial compression (ε_c^p), and pure-shear (ε_s^p). Alternately, the input can be provided as true stress-effective plastic strain ($\bar{\varepsilon}_{eff}^p$) (IFLAG = 1 in the LS-DYNA implementation) for uni-axial tension, uni-axial compression, and pure-shear stress states, respectively. Recall that in equation 76 it was shown that $\dot{\bar{\varepsilon}}_{eff}^p = \dot{\lambda}$.

The typical application of thermal dependency will be adiabatic heating due to the plastic work raising the temperature of the material, which will soften it. The adiabatic heating due to plastic work and the resulting temperature rise is calculated as:

$$T = T_{room} + \frac{\beta}{C_p \rho} \int_0^{\bar{\varepsilon}_{eff}^p} \sigma_p \, d\bar{\varepsilon}_{eff}^p \tag{219}$$

where T_{room} is the room or current temperature, β is the Taylor–Quinney coefficient that represents the proportion of plastic work converted into heat, C_p is the specific heat at constant pressure, ρ is the density, σ_p is a plastic stress, and $\bar{\varepsilon}_{eff}^p$ is the effective plastic strain.

The yield criterion f, equation 51, can be written with modified dependencies as:

$$f(\boldsymbol{\sigma}, \sigma_t, \sigma_c, \sigma_s) = f(\boldsymbol{s}, \sigma_t, \mathrm{c}_1, \mathrm{c}_2, \mathrm{c}_3) = \sigma_{vm}\left[c_1 + c_2 \frac{27 J_3}{2\sigma_{vm}^3} + c_3 \frac{729 J_3^2}{4\sigma_{vm}^6}\right] - \sigma_t \tag{220}$$

where c_1, c_2, and c_3 were previously summarized in equation 116, and are dependent on σ_t, σ_c, and σ_s. This can be seen in equation 218, because the stress parameters are a function of the effective plastic strains; σ_t, c_1, c_2, and c_3 are also a function of the effective plastic strain.

3.9.2 Kuhn-Tucker Conditions

The basic problem in elasto-plasticity is to obtain stresses that fulfill both the Kuhn-Tucker (Kuhn & Tucker, 1951) conditions and the consistency condition. As previously stated in section 3.1, the Kuhn-Tucker conditions (equation 40) require: that the plastic multiplier rate is always positive or zero $(\dot{\lambda} \geq 0)$, that the stress is always on or within the yield surface $(f(\boldsymbol{\sigma}, \sigma_y) \leq 0)$, and that the stresses remain on the yield surface during plastic loading $(\dot{\lambda} f(\boldsymbol{\sigma}, \sigma_y) = 0)$ (i.e., when $\dot{\lambda} > 0$). When $\dot{\lambda} > 0$, then $\dot{\lambda} f(\boldsymbol{\sigma}, \sigma_y) = 0$, which requires that $f(\boldsymbol{\sigma}, \sigma_y) = 0$, and the system is in a plastic state. Under continuous plastic loading, $f(\boldsymbol{\sigma}, \sigma_y)$ remains equal to zero for that period of loading, and then:

$$\dot{f}(\boldsymbol{\sigma}, \sigma_y) = 0 \tag{221}$$

which is the consistency condition. The stress rate must remain on the yield surface during plastic loading, and this enables the determination of the plastic multiplier $\dot{\lambda}$.

Beginning with the time derivative of the yield function (equation 220):

$$\dot{f} = \frac{df}{dt} = \frac{\partial f}{\partial \boldsymbol{\sigma}} : \dot{\boldsymbol{\sigma}} + \frac{\partial f}{\partial \lambda} \dot{\lambda} \tag{222}$$

Using equation 129:

$$\dot{\boldsymbol{\sigma}} = C_{ijkl}\left(\dot{\boldsymbol{\varepsilon}} - \dot{\lambda}\frac{\partial f}{\partial \boldsymbol{\sigma}}\right)$$

then the yield function rate is:

$$\dot{f} = \frac{\partial f}{\partial \boldsymbol{\sigma}} : \left[C_{ijkl}\dot{\boldsymbol{\varepsilon}} - \dot{\lambda}C_{ijkl}\frac{\partial f}{\partial \boldsymbol{\sigma}}\right] + \frac{\partial f}{\partial \sigma_t}\frac{\partial \sigma_t}{\partial \lambda}\dot{\lambda} + \sum_{i=1}^{3}\frac{\partial f}{\partial c_i}\frac{\partial c_i}{\partial \lambda}\dot{\lambda} \tag{223}$$

The derivative of the yield function, equation 220, with respect to the tension yield stress is:

$$\frac{\partial f}{\partial \sigma_t} = -1 \tag{224}$$

Therefore, for continuous plastic loading (equation 221), and using equation 224, equation 223 may be may be written as:

$$\dot{f} = 0 = \frac{\partial f}{\partial \boldsymbol{\sigma}} : C_{ijkl}\dot{\boldsymbol{\varepsilon}} - \dot{\lambda}\frac{\partial f}{\partial \boldsymbol{\sigma}} : C_{ijkl}\frac{\partial f}{\partial \boldsymbol{\sigma}} - \frac{\partial \sigma_t}{\partial \lambda}\dot{\lambda} + \sum_{i=1}^{3}\frac{\partial f}{\partial c_i}\frac{\partial c_i}{\partial \lambda}\dot{\lambda} \tag{225}$$

Then solving for the plastic multiplier rate yields:

$$\dot{\lambda} = \frac{\frac{\partial f}{\partial \boldsymbol{\sigma}} : C_{ijkl}\dot{\boldsymbol{\varepsilon}}}{\frac{\partial f}{\partial \boldsymbol{\sigma}} : C_{ijkl}\frac{\partial f}{\partial \boldsymbol{\sigma}} - \frac{\partial \sigma_t}{\partial \lambda} + \sum_{i=1}^{3}\frac{\partial f}{\partial c_i}\frac{\partial c_i}{\partial \lambda}} \tag{226}$$

Because by definition $\frac{\partial f}{\partial \boldsymbol{\sigma}}$ is deviatoric, then $C_{ijkl}\frac{\partial f}{\partial \boldsymbol{\sigma}} = 2G\frac{\partial f}{\partial \boldsymbol{\sigma}}$ and $C_{ijkl}\dot{\boldsymbol{\varepsilon}} = 2G\dot{\boldsymbol{e}}$

and equation 226 may be written as:

$$\dot{\lambda} = \frac{2G\frac{\partial f}{\partial \boldsymbol{\sigma}} : \dot{\boldsymbol{e}}}{2G\frac{\partial f}{\partial \boldsymbol{\sigma}} : \frac{\partial f}{\partial \boldsymbol{\sigma}} - \frac{\partial \sigma_t}{\partial \lambda} + \sum_{i=1}^{3}\frac{\partial f}{\partial c_i}\frac{\partial c_i}{\partial \lambda}} \tag{227}$$

In equation 227, $\frac{\partial \sigma_t}{\partial \lambda} - \sum_{i=1}^{3}\frac{\partial f}{\partial c_i}\frac{\partial c_i}{\partial \lambda}$ represents the hardening behavior terms. In the case of perfectly plastic material behavior, these terms are equal to zero because material exhibits no strain-hardening.

In the GYS model, the value for $\Delta\lambda$ is determined using a secant iteration, with $\Delta\lambda_0 = 0$ for the initial value $(f > 0)$. The second value for the increment of the plastic multiplier, $\Delta\lambda_1$, is determined from equation 227, where $\frac{\partial \sigma_y^t}{\partial \lambda} - \sum_{i=1}^{3}\frac{\partial f}{\partial c_i}\frac{\partial c_i}{\partial \lambda} = 0$. This means that the initial response is perfectly plastic, and it corresponds to the return of $\boldsymbol{\sigma}_{n+1}^{trial}$ to the frozen yield surface of time t_n as if the material were perfectly plastic with no hardening evolution. The initial solution interval is bounded using the first two values for the secant iteration, $\Delta\lambda_0 = 0$ $(f > 0)$ and $\Delta\lambda_1$. The initial perfect plasticity ensures that the stress state returns to the interior of the yield surface, resulting in a negative value of the yield function $(f < 0)$.

3.9.3 Time Integration and Numerical Implementation of GYS Into LS-DYNA

The GYS was implemented into LS-DYNA (Hallquist, 1993), a widely available commercial finite element software program. Typical dynamic stress wave problems in LS-DYNA are solved with an explicit time-marching procedure. The strain rate tensor is assembled from the nodal velocities at the beginning of each computational cycle. The strain rate tensor and associated stresses from the beginning of the cycle are then input to the material constitutive model, in which updated stresses are calculated. The new stresses are subsequently used in the momentum equation to update the nodal velocities, completing the cycle.

Therefore, within the material constitutive model at each time increment, integrating the constitutive equations governing material behavior requires a stress update algorithm. There exist a number of different stress update algorithms (Ortiz & Simo, 1986, Kojic, 2002, Hughes, 1983, Becker, 2011, Simo & Taylor, 1986, Krieg & Krieg, 1977, and Wilkins, 1964). A summary of the principal methods is given by Belytschko and Simo (Belytschko, et al., 2000) and Hughes (Simo & Hughes, 1998).

The GYS was implemented into LS-DYNA using a return-mapping algorithm and semi-implicit integration. Return-mapping algorithms are widely used for numerically implementing these stress updates. Return-mapping algorithms first predict the trial stresses based on the current total strain increment (an elastic predictor step) and then return the stresses back to the yield surface using an iterative procedure for the plastic deformation correction (see figure 40). Semi-implicit backward Euler methods (Belytschko, et al., 2000, Ortiz & Simo, 1986, and Simo & Hughes, 1998) are implicit in the plasticity parameter, but explicit in the plastic flow direction (i.e., the increments in the plasticity parameter [$\Delta\lambda$] are calculated at the end of each step, but plastic flow direction $\frac{\partial f}{\partial \boldsymbol{\sigma}}$ is calculated at the beginning of the step).

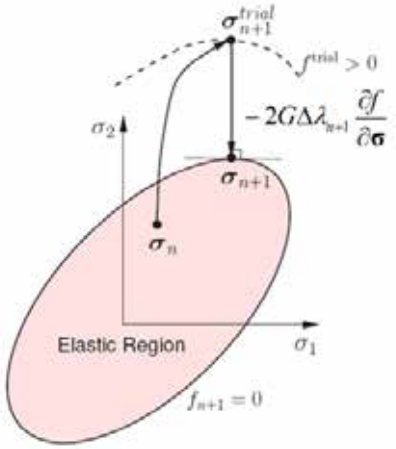

Figure 40. Schematics of return-mapping algorithm in stress space

The semi-implicit integrating of the stresses is a nonlinear scalar equation, which is a function of the plastic multiplier. This equation is solved using a secant method. In each time step, all of the constitutive variables (stresses) at the state t_n, and the total strain at the state t_{n+1}, are available.

The stresses are updated at t_{n+1} with the return-mapping algorithm. Figure 41 shows the relationship between LS-DYNA and GYS subroutine and return-mapping algorithms for the GYS.

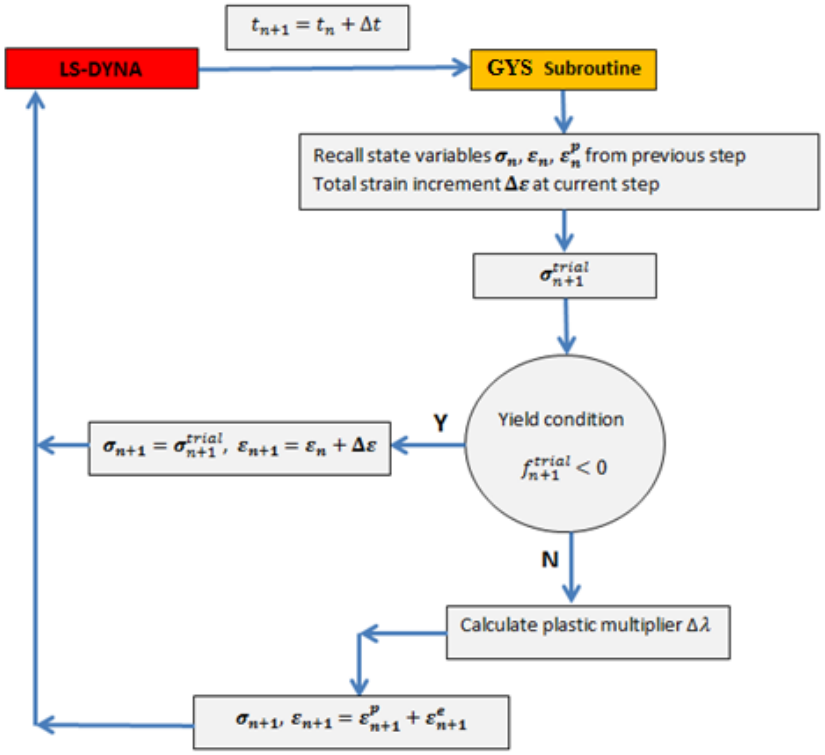

Figure 41. Schematic of return-mapping algorithm for the GYS

The main steps in the return-mapping algorithm with semi-implicit (semi-backward Euler) integration are given as follows:

1. Initializing: the initial values of plastic strain and internal variables are set to the last converged values from previous time step.
2. Elastic prediction.
3. Checking the yielding condition.
4. Calculating the incremental plastic multiplier.
5. Computing the incremental stress and internal variables.
6. Updating the stress and internal variables.

The time step t_n to t_{n+1} is defined by the time increment $\Delta t = t_{n+1} - t_n$. At the beginning of each time step t_n, the stress and strain tensor are input to the GYS subroutine. Additionally, the total strain at t_{n+1} is known because the total strain increment for Δt is provided by the input from LS-DYNA. Therefore, the known values are $\boldsymbol{\sigma}_n, p_n, \boldsymbol{s}_n, \boldsymbol{\varepsilon}_n, \Delta\boldsymbol{\varepsilon}, \boldsymbol{\varepsilon}_{n+1}, \bar{\varepsilon}_n^p, T_n$, where:

$$\boldsymbol{\varepsilon}_{n+1} = \boldsymbol{\varepsilon}_n + \Delta\boldsymbol{\varepsilon} \tag{228}$$

Beginning with the hydrostatic terms, using the total strain tensor increment, $\Delta\boldsymbol{\varepsilon}$, corresponding to time increment Δt, the increment in pressure is:

$$\Delta p_n = -K\, trace(\Delta \boldsymbol{\varepsilon}) \tag{229}$$

The correspondingly hydrostatic stress increment and trial hydrostatic stress are:

$$\begin{aligned} \Delta \sigma^H &= -\Delta p_n = K\, trace(\Delta \boldsymbol{\varepsilon}) \\ \sigma^H_{(n+1)trial} &= \Delta \sigma^H + \sigma^H_n \end{aligned} \tag{230}$$

The hydrostatic stress tensor of the trial elastic state is equivalent to the hydrostatic stress tensor at the end of the time increment at t_{n+1}, because there is no plastic volumetric strain ($trace(\Delta \boldsymbol{\varepsilon}^p) = \mathbf{0}$):

$$\sigma^H_{(n+1)trial}\boldsymbol{\delta} = \sigma^H_{(n+1)}\boldsymbol{\delta} \tag{231}$$

The yield surface is pressure-independent and can be written solely in terms of the deviatoric stress tensor. The deviatoric strain increment is:

$$\Delta \boldsymbol{e} = \Delta \boldsymbol{\varepsilon} - \frac{1}{3} trace(\Delta \boldsymbol{\varepsilon})\boldsymbol{\delta} \tag{232}$$

Then the trial deviatoric stress tensor and the trial stress tensor are given by:

$$\begin{aligned} \boldsymbol{s}_{(n+1)trial} &= \boldsymbol{s}_n + 2G\Delta \boldsymbol{e} \\ \boldsymbol{\sigma}_{(n+1)trial} &= \sigma^H_{(n+1)trial}\boldsymbol{\delta} + \boldsymbol{s}_{(n+1)trial} \\ \boldsymbol{\sigma}_{(n+1)trial} &= \boldsymbol{\sigma}_n + K\, trace(\Delta \boldsymbol{\varepsilon})\boldsymbol{\delta} + 2G\Delta \boldsymbol{e} \end{aligned} \tag{233}$$

Correspondingly, the trial von Mises stress and trial Lode parameter are:

$$\sigma_{vm(n+1)trial} = \sqrt{\frac{3}{2}\boldsymbol{s}_{(n+1)trial} : \boldsymbol{s}_{(n+1)trial}} \tag{234}$$

$$J_3^{(n+1)trial} = det(\boldsymbol{s}_{(n+1)trial}) \tag{235}$$

and the trial effective stress is:

$$\sigma_{eff(n+1)trial} = \sigma_{vm(n+1)trial}\left(c_1^n + c_2^n \frac{27 J_3^{(n+1)trial}}{2\left(\sigma_{vm(n+1)trial}\right)^3} + c_3^n \frac{729\left(J_3^{(n+1)trial}\right)^2}{4\left(\sigma_{vm(n+1)trial}\right)^6}\right) \tag{236}$$

If the effective stress of the GYS model at step n+1, $\sigma_{eff(n+1)trial}$ is inside the yield surface, the response is elastic, and no return mapping is needed. In this elastic case, the trial values become the final values at the end of the time step. When $\sigma_{eff(n+1)trial}$ is beyond the yield surface, the trial stress needs to be corrected back to the yield surface.

The integration operator is composed of an elastic predictor and plastic correction step. In the elastic predictor, the incremental total strain vector, $\Delta \boldsymbol{\varepsilon}$, is imposed while keeping internal

variables constant and equal to their respective values at t_n. These conditions lead to a trial elastic state, defined by the trial stress, which is iteratively corrected by the plastic correction, as shown in figure 42.

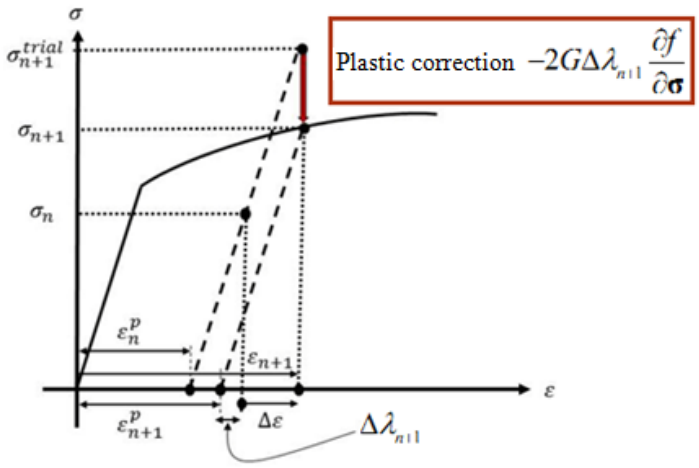

Figure 42. Stress update scheme using trial stress and plastic correction

The direction of the plastic flow is assumed to be coaxial with the elastic trial stress. Consequently, the stress at the end of the time step is in the same direction as the elastic trial stress. This leads to a coaxial return in deviatoric stress space. In the case of von Mises plasticity, this return is radial in deviatoric space. However, in GYS when there is tension-compression asymmetry or there is a shear-to-tension yield ratio other than $1/\sqrt{3}$, return is not radial because, in these cases, the yield surface is no longer a sphere in deviatoric stress space. The time increment is achieved through a central difference scheme. The incremental algorithm is summarized in equation 237 and includes previously defined equations 232 through 236, with the subscripts condensed for clarity:

$$\dot{\boldsymbol{e}} = \dot{\boldsymbol{\varepsilon}} - \frac{1}{3} trace(\dot{\boldsymbol{\varepsilon}})\boldsymbol{\delta}$$

$$\boldsymbol{s}_{trial} = \boldsymbol{s}_n + 2G\dot{\boldsymbol{e}}\Delta\boldsymbol{t}$$

$$\sigma_{vm(trial)} = \sqrt{\frac{3}{2}\boldsymbol{s}_{trial} : \boldsymbol{s}_{trial}}$$

$$J_3^{trial} = \det(\boldsymbol{s}_{trial})$$

$$\sigma_{eff(trial)} = \sigma_{vm(trial)}\left(c_1^n + c_2^n \frac{27 J_3^{trial}}{2\left(\sigma_{vm(trial)}\right)^3} + c_3^n \frac{729\left(J_3^{trial}\right)^2}{4\left(\sigma_{vm(trial)}\right)^6}\right) \tag{237}$$

$$If\ \sigma_{eff(trial)} \leq \sigma_{y(n)} \implies \Delta\lambda = 0 \implies \boldsymbol{s}_{n+1} = \boldsymbol{s}_{trial}$$

$$If\ \sigma_{eff(trial)} > \sigma_{y(n)} \implies \Delta\lambda > 0 \implies f_{n+1}(\Delta\lambda) = 0 \implies \boldsymbol{s}_{n+1} = \boldsymbol{s}_{trial} - 2G\Delta\lambda\frac{\partial f}{\partial \boldsymbol{\sigma}}$$

$$\boldsymbol{\sigma}_{n+1} = \boldsymbol{\sigma}_{trial} - 2G\Delta\lambda\frac{\partial f}{\partial \boldsymbol{\sigma}}$$

To determine the yield function at time t_{n+1}, a nonlinear equation is derived and solved for the increment of the plastic multiplier $\Delta\lambda$. Because the hardening is nonlinear, the equation is nonlinear. Note that because it was previously shown that $\dot{\bar{\varepsilon}}_{eff}^{p} = \dot{\lambda}$, the increment of the plastic multiplier is equal to the effective plastic strain increment $\Delta\lambda = \Delta\bar{\varepsilon}_{eff}^{p}$. The equations required to solve for the yield function, including updated versions of equations 234 through 236, are:

$$\sigma_{vm}^{n+1} = \sqrt{\frac{3}{2}\boldsymbol{s}^{n+1} : \boldsymbol{s}^{n+1}}$$

$$J_3^{n+1} = \det(\boldsymbol{s}^{n+1})$$

$$\sigma_{eff}^{n+1} = \sigma_{vm}^{n+1}\left(c_1^{n+1} + c_2^{n+1} \frac{27 J_3^{n+1}}{2\left(\sigma_{vm}^{n+1}\right)^3} + c_3^{n+1} \frac{729\left(J_3^{n+1}\right)^2}{4\left(\sigma_{vm}^{n+1}\right)^6}\right) \tag{238}$$

$$f^{n+1}(\Delta\lambda) = \sigma_{eff}^{n+1}(\lambda^{n+1}) - \sigma_y^{n+1}\left(\lambda^{n+1}, \frac{\Delta\lambda}{\Delta t}, T^{n+1}\right)$$

$$f^{n+1}(\Delta\lambda) = \sigma_{eff}^{n+1}(\lambda_{\,n} + \Delta\lambda) - \sigma_y^{n+1}\left(\lambda_{\,n} + \Delta\lambda, \frac{\Delta\lambda}{\Delta t}, T_n + \frac{\beta\Delta\lambda}{C_p\rho}\left(\frac{\sigma_{vm}^{n+1} + \sigma_{vm}^{n}}{2}\right)\right)$$

where T^{n+1} is the current temperature, C_p is the specific heat at constant pressure (assumed constant during the numerical simulation), and β is the Taylor-Quinney coefficient that represents the proportion of plastic work converted into heat. As discussed in section 3.9.1, the incremental temperature increase caused by dissipation of plastic work due to adiabatic heating is calculated and will create thermal softening.

In the GYS model, the return mapping is coaxial with the trial state and not radial. Even though the return is not radial, the return direction remains the same as that defined by the initial trial state. It does not change during iterations within the time interval. Figure 43 is a schematic representation of the return algorithm, with pressure versus the invariant plane of deviatoric stress. This figure also demonstrates how the pressure remains unaffected by the GYS plasticity.

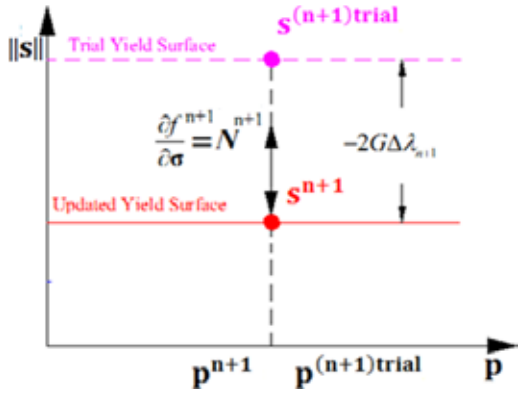

Figure 43. Geometric interpretation of the return on the invariant plane

The implemented return method finds the root of the nonlinear implicit scalar function iteratively. This root is the increment in the plastic multiplier and effective plastic strain. The scalar function might have more than one root; one might be negative (a solution with $\Delta\lambda < 0$). A negative $\Delta\lambda$ is physically meaningless and is disregarded. Physically, $\Delta\lambda$ can range from zero to a large value of $\Delta\lambda$. The nonlinear scalar function monotonically decreases (Kojic & Bathe, 2005) because the derivative of the function with respect to incremental plastic multiplier, $\frac{df}{d(\Delta\lambda)}$ is negative (see appendix B for details). Therefore, it has only one positive root in the solution interval, as shown in figure 44.

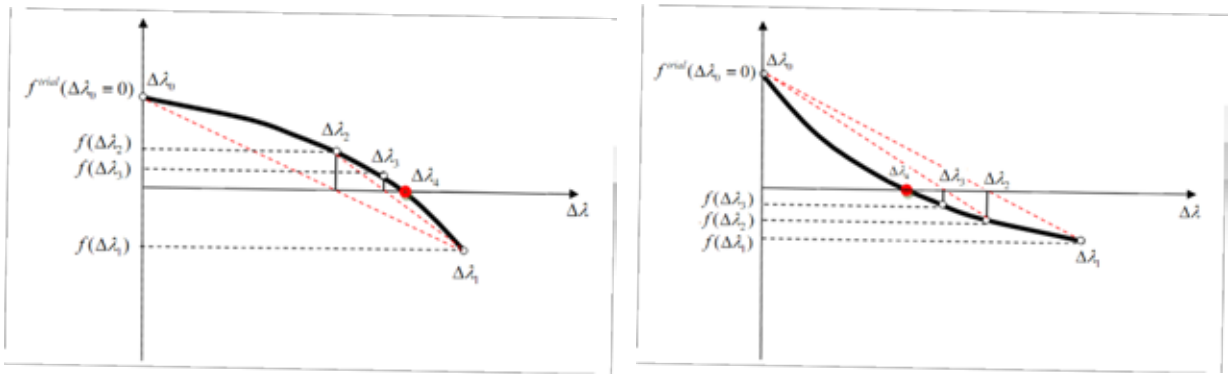

Figure 44. Successive secant iterations and dependence of function *f* on the increment of equivalent plastic strain; note that curvature of the function f could be either (a) or (b) without effecting the monotonic decreasing of the function (Du Bois, 2012, and Kojic & Bathe, 2005)

In the GYS implementation, a secant method is used to determine the correct value of the root. In the secant method, a solution interval is bounded by two initial guesses, $\Delta\lambda_0$ and a large value of $\Delta\lambda_1$ (corresponds to perfect plasticity). Within the solution interval, the root is estimated and then determined iteratively. The only assumption made by the algorithm is that the plastic flow direction is the same for the trial state and updated state. No iteration is performed on the flow direction, and the return to yield surface is coaxial with trial state. This assumption is valid for a small time step and the resulting small strain increment, small being relative to the yield strain. Considering explicit finite element methods, in which the time step is limited by the Courant condition (Courant, et al., 1928), time steps in LS-DYNA will be small enough that this assumption is valid.

In summary, the nonlinear implicit scalar function is solved using the secant method to calculate $\Delta\lambda$, which is the root for which $f = 0$ (within a tolerance):

$$f^{n+1}(\Delta\lambda) = f^{trial} + \frac{\partial f}{\partial \boldsymbol{\sigma}} : \left[-\dot{\lambda}\Delta t C_{ijkl}\frac{\partial f}{\partial \boldsymbol{\sigma}}\right]$$
$$f^{n+1}(\Delta\lambda) = \sigma_{eff}^{n+1}(\lambda^{n+1}) - \sigma_y^{n+1}\left(\lambda^{n+1}, \frac{\Delta\lambda}{\Delta t}, T^{n+1}\right) = 0 \quad (239)$$

In both equation 239 and equation 240, the derivative $\frac{\partial f}{\partial \boldsymbol{\sigma}}$ is evaluated at the trial stress point. The secant method solution for the plastic multiplier and effective plastic strain increment ($\Delta\lambda = \Delta\bar{\varepsilon}_{eff}^{p}$), including the iterative scheme (Kojic & Bathe, 2005) (Berstad, et al., 1994) and initial estimates, is summarized in equation 240:

$$\Delta\lambda_0 = 0$$
$$\Delta\lambda_1 = \frac{f^{trial}}{\frac{\partial f}{\partial \boldsymbol{\sigma}} : C_{ijkl}\frac{\partial f}{\partial \boldsymbol{\sigma}}} = \frac{\sigma_{eff}^{trial} - \sigma_y^n}{2G\frac{\partial f}{\partial \boldsymbol{\sigma}} : \frac{\partial f}{\partial \boldsymbol{\sigma}}}$$
$$\Delta\lambda_2 = \Delta\lambda_1 - f(\Delta\lambda_1)\frac{\Delta\lambda_1 - \Delta\lambda_0}{f(\Delta\lambda_1) - f(\Delta\lambda_0)} \quad (240)$$
$$\Delta\lambda_{k+1} = \Delta\lambda_k - f(\Delta\lambda_k)\frac{\Delta\lambda_k - \Delta\lambda_{k-1}}{f(\Delta\lambda_k) - f(\Delta\lambda_{k-1})}$$
$$If\ f^{n+1}(\Delta\lambda_{\boldsymbol{k+1}}) - (\Delta\lambda_{\boldsymbol{k}}) \leq \boldsymbol{tolerance} = 10^{-6} \implies STOP$$

In the LS-DYNA implementation, the initial increment was programmed using a von Mises approximation. It was assumed that a von Mises initial estimate will always be larger than that based on equation 240, and therefore the value of the converged root and plastic multiplier would be the same.

3.9.4 LS-DYNA GYS Keyword Input

The GYS material model has been implemented into the LS-DYNA finite element program as a material law called MAT TABULATED JOHNSON COOK GYS or, alternately, MAT224_GYS. The GYS material law is only available for solid elements.

Plastic deformation in metals can be strain-rate dependent. Including those rate effects is important for accurate analytical predictions. The von Mises yield function assumes that strain-rate sensitivity in all stress states is the same as it is in tension. However, strain-rate sensitivity is not symmetric in all metals. Material tests at different strain rates for uni-axial tension, uni-axial compression, and pure-shear stress states should be performed. If these dynamic tests are available, the load curves defining the yield stress in uni-axial tension, uni-axial compression, and pure-shear can be defined using the table definitions LCK1, LCCR, and LCSR in MAT224_GYS. These tables contain multiple load curves corresponding to stress at different values of the plastic strain rate, as shown in figure 45. Separate temperature dependency for tension, compression, and shear may also be included in MAT224_GYS using tables LCKT, LCCT, and LCST. Detailed instructions for, and an example of, the preparation of data for MAT224_GYS are included in section 5.

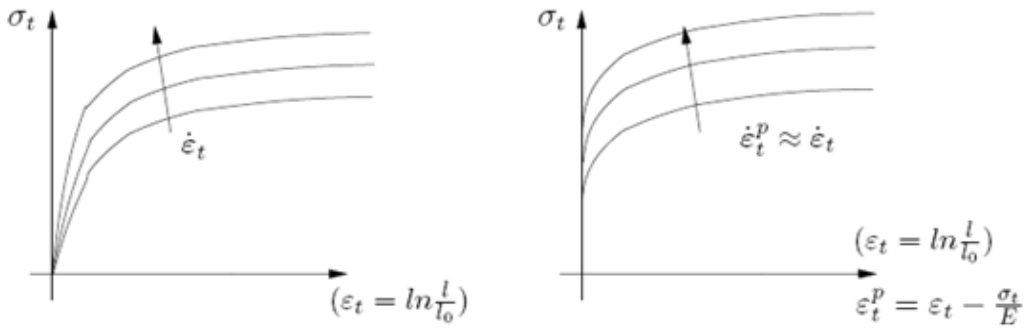

Figure 45. Rate-dependent tensile hardening curve from dynamic tensile test

In the LS-DYNA implementation, a plasticity algorithm of the GYS model is coupled with the previously developed stress-state-dependent failure model of MAT224 (i.e., material laws MAT224 and MAT224_GYS use the same element erosion criteria, but MAT224 uses classical J_2 plasticity [von Mises Plasticity], and MAT224_GYS uses the presented J_3 dependent plasticity model). More information regarding the failure model can be found in references (Hallquist, 2009, Buyuk, et al, 2009, Buyuk, 2013, and Carney, et al., 2009).

Two parameters, SFIEPM and NITER, are available that modify the search for the root during the secant iterations. SFIEPM scales the solution interval determined by the two initial guesses for plastic multiplier. As discussed in the previous section, the root should be in the solution interval covered by the first two initial values of the secant method. If a solution for the plastic multiplier is not obtained in an analysis using GYS, SFIEPM may be modified by trial and error until the root is in the solution interval. NITER increases the number of secant iterations to be performed in the search for the root, within the solution interval.

The keyword input for the MAT224_GYS model is given in table 3. Users are encouraged to reference a recent version of the LS-DYNA User's Manual (Hallquist, 2009) for updates, enhancements, or additional implementation details.

Table 3. MAT224_GYS input in LS-DYNA

Card 1	1	2	3	4	5	6	7	8
Variable	MID	RO	E	PR	CP	TR	BETA	NUMINT
Type	A8	F	F	F	F	F	F	F
Default	none	none	none	none	none	0.0	1.0	1.0

Card 2	1	2	3	4	5	6	7	8
Variable	LCK1	LCKT	LCF	LCG	LCH	LCI		
Type	I	I	I	I	I	I		
Default	0	0	0	0	0	0		

Card 3	1	2	3	4	5	6	7	8
Variable	LCCR	LCCT	LCSR	LCST	IFLAG	SFIEPM	NITER	
Type	I	I	I	I	I	F	I	
Default	0	0	0	0	0	1	100	

MID: Material ID

RO: Mass density

E: Young Modulus

PR: Poison Ratio

CP: Specific Heat

TR: Room Temperature (or Reference Temperature)

BETA: Taylor–Quinney Coefficient (fraction of plastic work converted into heat)

NUMINT: Number of integration points that must fail before the element is deleted

LCK1: Rate-dependent table of load curves giving tensile yield stress as a function of plastic strain or effective plastic strain

LCKT: Temperature-dependent table of load curves giving tensile yield stress as a function of plastic strain or effective plastic strain

LCF: State-of-stress-dependent table giving plastic strain for element erosion

LCG: Scaling of LCF as a function of strain rate

LCH: Scaling of LCF as a function of temperature

LCI: Scaling of LCF as a function of element size

LCCR: Rate-dependent table of load curves giving compressive yield stress as a function of plastic strain or effective plastic strain

LCCT: Temperature-dependent table of load curves giving compressive yield stress as a function of plastic strain or effective plastic strain

LCSR: Rate-dependent table of load curves giving shear yield stress as a function of plastic strain or effective plastic strain

LCST: Temperature-dependent table of load curves giving shear yield stress as a function of plastic strain or effective plastic strain

IFLAG: If IFLAG = 0, the compressive and shear yields are given as a function of plastic strain and if IFLAG = 1, the compressive and shear yields are given as a function of effective plastic strain

SFIEPM: Scale factor on the initial estimate of the plastic multiplier

NITER: Number of secant iterations to be performed

4. SINGLE-ELEMENT TESTING OF THE GYS PLASTICITY MODEL

In this section, the testing of the GYS model implementation using single-element models is presented. To test the implementation, single-element test cases using various stress states, temperatures, and strain rates were simulated. Single-element test cases using different stress states were also run using different time steps to test stability. The semi-implicit integration method used in the GYS stress-update algorithm was shown to be accurate, using the time step size calculated by LS-DYNA to guarantee stability. The single-element testing of the convexity algorithm is also presented.

4.1 Testing of the GYS Material Model using Various Loadings

Fully integrated, hexahedral finite elements are used to model cubes under different states of stress. Uni-axial tension, bi-axial tension, uni-axial compression, bi-axial compression, pure-shear, plane-strain tension, and plane-strain compression cases are modeled, as shown in figure 46. A constant velocity displacement boundary condition is defined for the nodes on the top surface of the finite elements. The LS-DYNA material model MAT PIECEWISE LINEAR PLASTICITY (MAT24), which uses a von Mises yield function, was selected for comparison with MAT224_GYS.

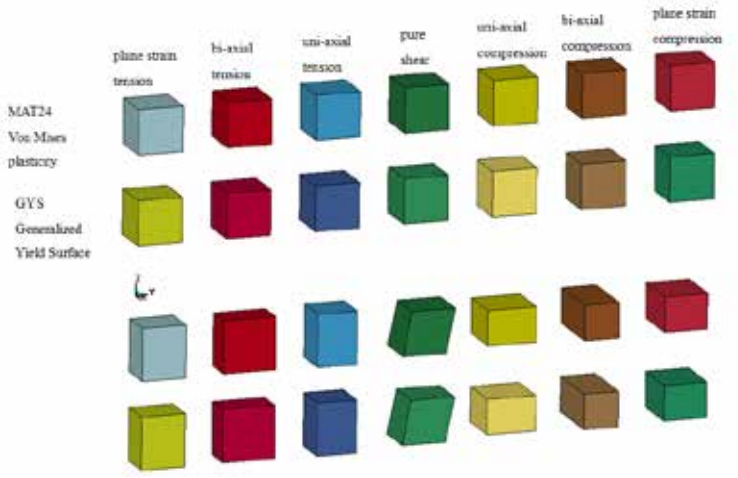

Figure 46. Single-element models undergoing different states of stress, with the top two rows showing the undeformed geometry, and the bottom two rows showing the deformed geometry

The first check was to ensure that the MAT224_GYS implementation, with comparable input, will produce identical results to MAT24. The same generic, rate-independent stress-strain curve was used for both tension and compression in the MAT224_GYS model and that used in the MAT24 model. In the GYS material model, the input shear curve stress was $1/\sqrt{3}$ times the tension stress. These GYS input curves should produce the same results as a von Mises model. The identical results were obtained for all of the modeled stress-states. The MAT24 and MAT224_GYS output are overlaid in figure 47 to show the exact matches.

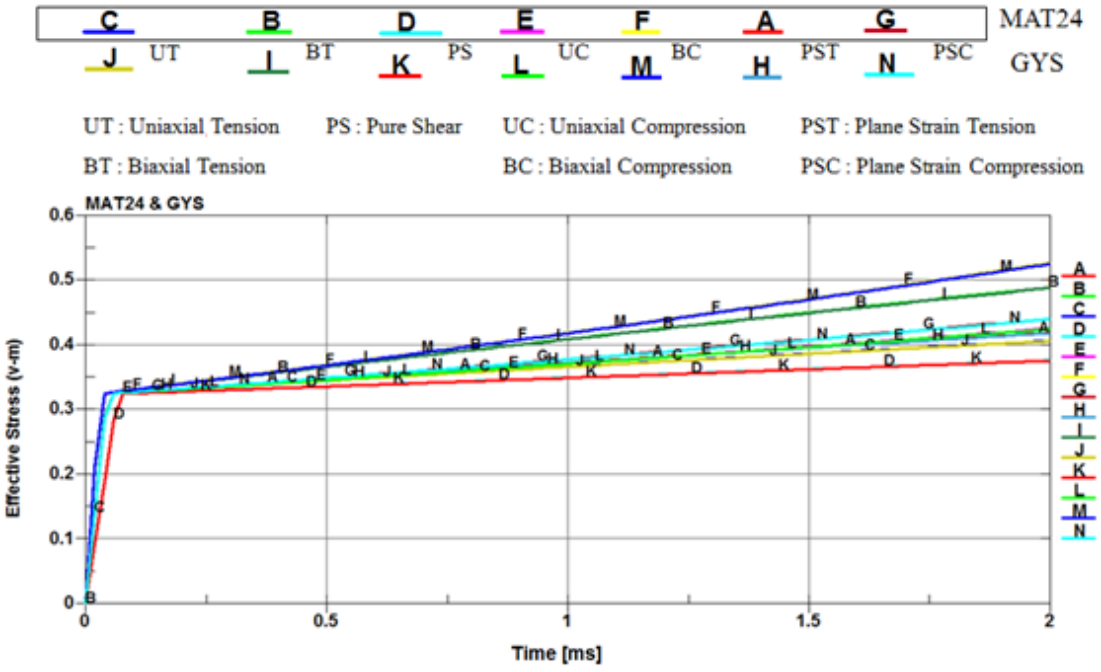

Figure 47. GYS-Mat24 comparison under the von Mises plasticity assumption for both models

Second, the functioning of the temperature-dependency curves was checked. Two different MAT224_GYS models were created. One model used the same compression and tension curves at both the 300 K and 775 K temperatures, consistent with von Mises plasticity. The other model used different tension and compression curves at the elevated temperature of 775 K. The generic, temperature-dependent yield curves for the model labeled "GYS" in the following figures are shown in figure 48. The "GYS" model had different tension and compression yield curves for the elevated temperature. The model labeled "von Mises Plasticity" in the following figures used curve B in figure 48 for both tension and compression and, therefore, used the same elevated temperature tension curve as the "GYS" model.

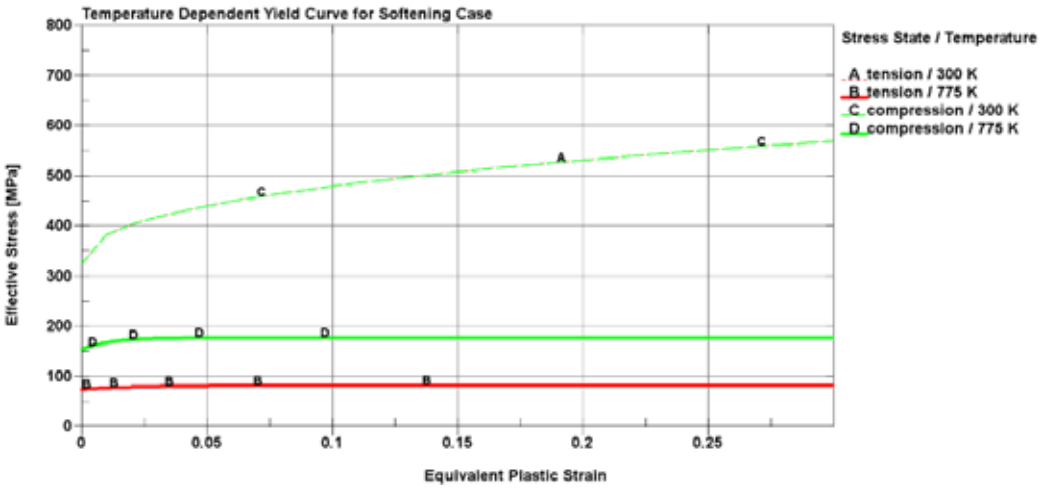

Figure 48. MAT224_GYS temperature-dependent stress-strain curves

In the uni-axial tension single-element test cases, temperature increase due to the plastic work and the resulting thermal softening as a function of the temperature-dependent stress-strain curves were as expected. For this study, a Taylor-Quinney coefficient (β) of 0.9 was used. Because both the "GYS" and the "von Mises Plasticity" labeled models used the same curves in tension, both models have the same response in uni-axial tension, as shown in figure 49. The associated temperature increase in this analysis is shown in figure 50.

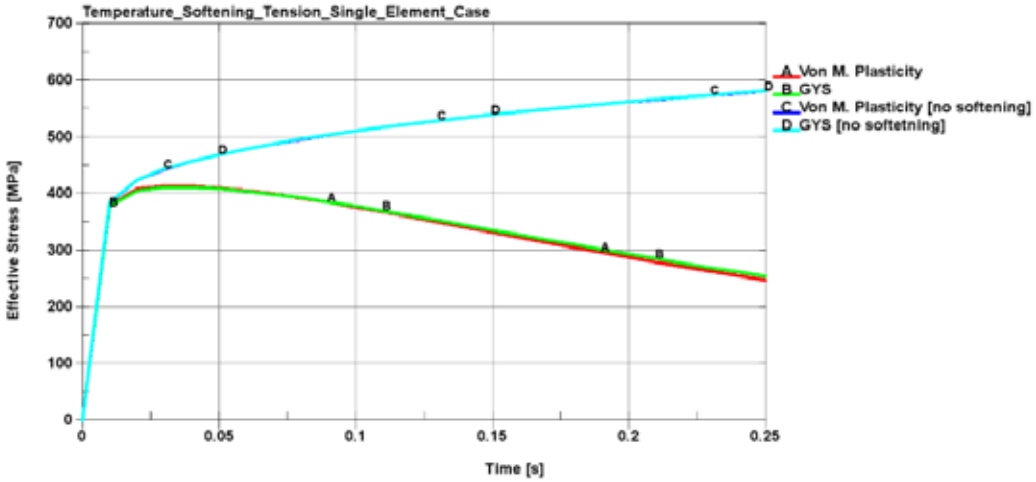

Figure 49. Thermal softening—tension single-element case (von Mises Plasticity vs. GYS)

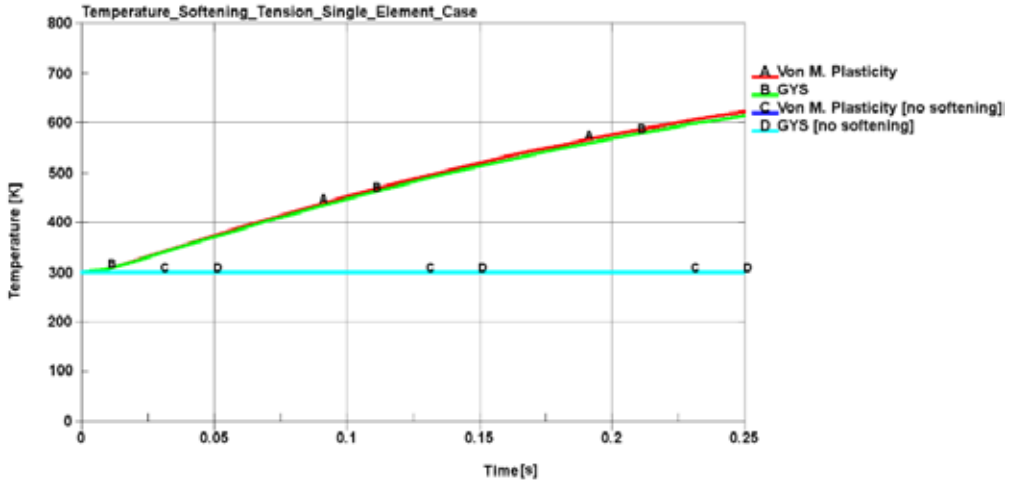

Figure 50. Temperature increase in the tension single-element case (von Mises Plasticity vs. GYS)

As shown in figure 51, in the case of uni-axial compression the thermal softening has a different effect on the effective stress of the “GYS” labeled model than that of the “von Mises Plasticity” labeled model. This is expected because the “GYS” model uses curve D in compression, and the “von Mises Plasticity” model uses curve B in compression for elevated temperatures, as shown in figure 48. Remember that the “von Mises Plasticity” labeled model is using the same temperature-dependent curve for both tension and compression. The associated temperature increase in this analysis is shown in figure 52.

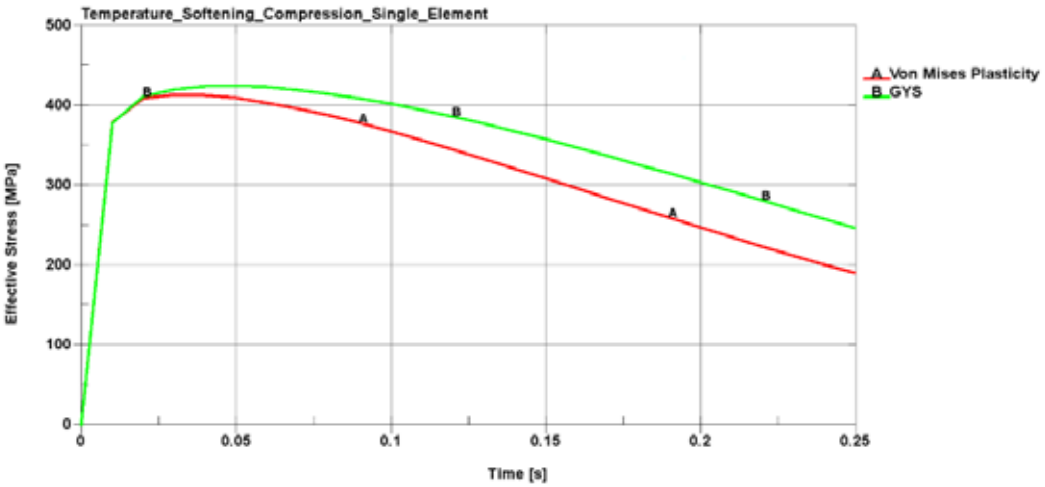

Figure 51. Temperature softening—compression single-element case (von Mises Plasticity vs. GYS)

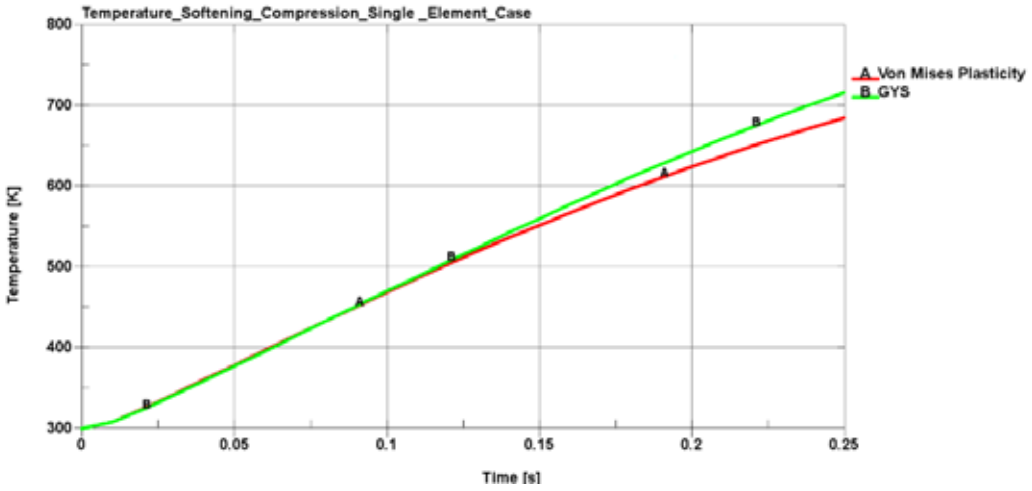

Figure 52. Temperature increase in the compression single-element case (von Mises Plasticity vs. GYS)

Third, the functioning of the strain-rate dependency curves was checked. As in the temperature dependency study, two different MAT224_GYS models were created. One model used the same compression and tension curve for both of the 1/s and 100/s strain rates, consistent with von Mises plasticity. The other model used different tension and compression curves at the elevated strain rate of 100/s. The generic, strain-rate-dependent yield curves for the model entitled “GYS” in the following figures are shown in figure 53. The “GYS” model had different tension and compression yield curves at the elevated strain rate. The model entitled “von Mises Plasticity” in the following figures used curve B in figure 53 for both tension and compression and therefore used the same elevated strain-rate tension curve as the “GYS” model.

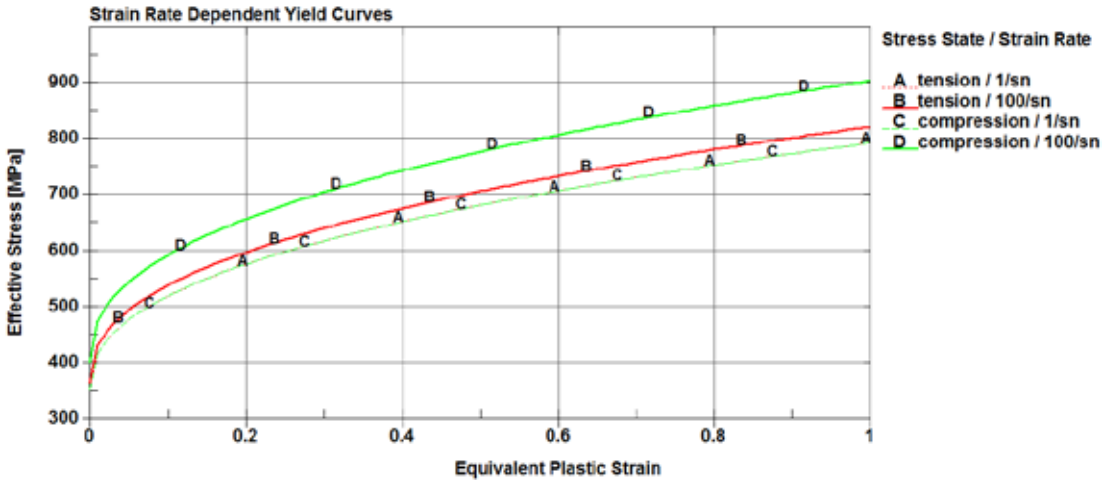

Figure 53. Strain-rate-dependent yield curves for single-element strain-rate dependency case

As shown in figure 54, both models produce the same results under compression at a strain rate of 1/s because they have the same rate-dependent input curve at 1/s. In contrast, the "GYS" labeled model results in a higher flow stress under compression at a strain rate of 100/s, compared to the "von Mises Plasticity" labeled model, as shown in figure 55. This is expected because the "GYS" model uses curve D in compression, and the "von Mises Plasticity" model uses curve B in compression for elevated strain rates, as shown in figure 53. Remember that the "von Mises Plasticity" model is then using the same strain-rate-dependent curve for both tension and compression.

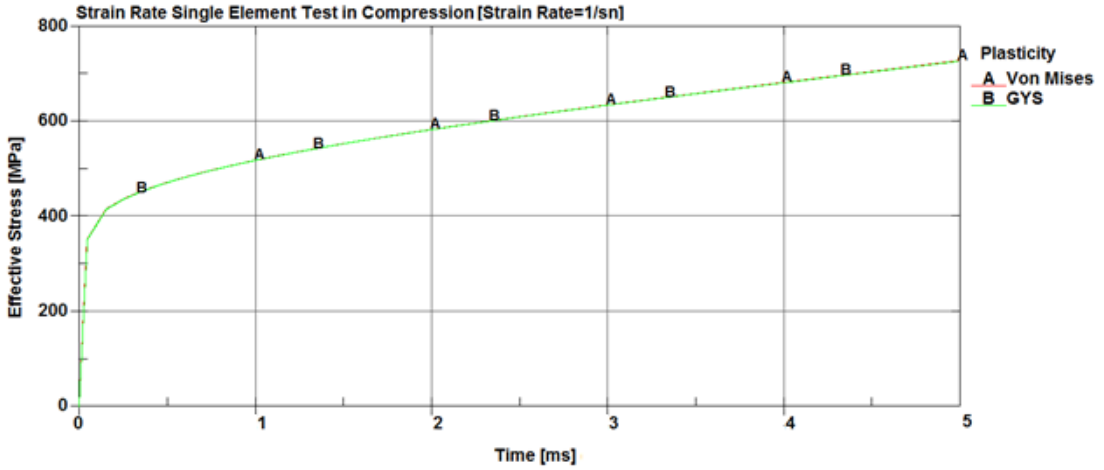

Figure 54. Strain-rate single-element test in compression (strain rate = 1/sn)

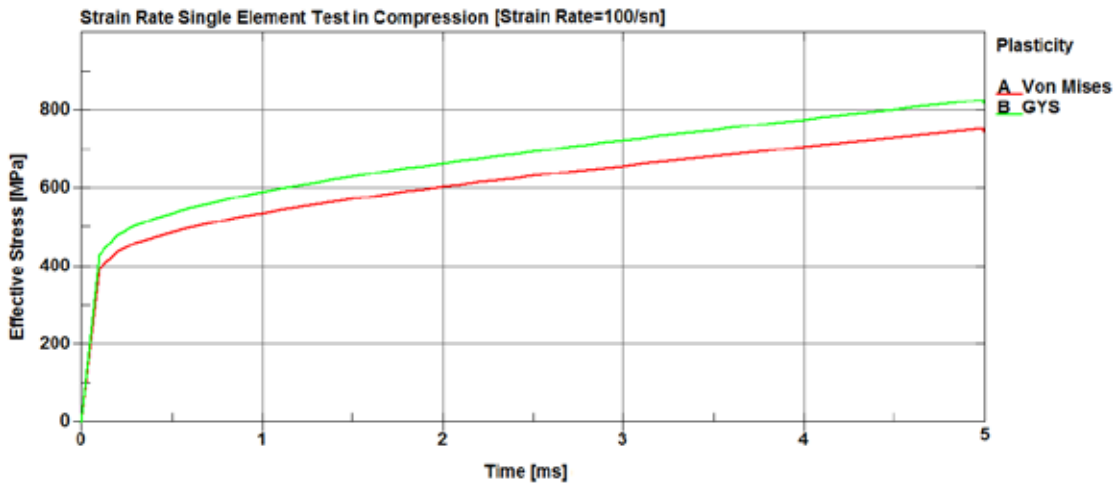

Figure 55. Strain-rate single-element test in compression (strain rate = 100/sn)

Fourth and finally, the numerical stability of the algorithm with varying time steps, using different loadings on single-element models, was tested. In general, there are small errors in stress predictions as a consequence of the numerical approximations and round-off present in computations. In the presence of these errors, the algorithm should provide reasonable accuracy and stability, and error should diminish as the strain increments are decreased.

In figure 56, the effect of having too large of a time step, and corresponding strain increment, on the accuracy of the return-mapping response is shown. The stress increment and return mapping in figure 56 (a) is acceptable, in which a plastic strain direction estimated from the beginning of the time step for a small strain increment results in a small percentage change in stress level. In figure 56 (b), an exaggerated stress increment (i.e., an order of magnitude larger than the stress level) is problematic because the return is not to the yield surface.

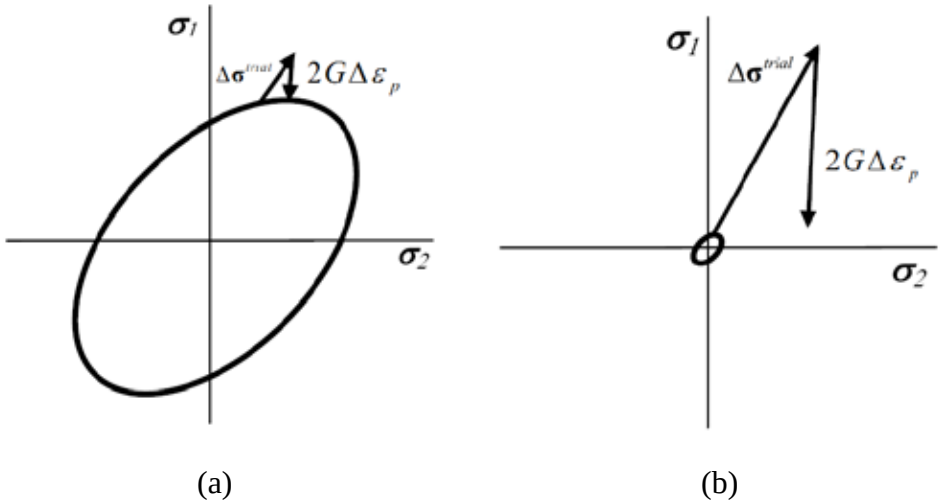

(a) (b)

Figure 56. Stress increment and return mapping using a plastic strain direction estimated from the beginning of the time step for: a) a small strain increment and b) a strain more than an order of magnitude larger than the yield strain (Becker, 2011)

To create a large-magnitude strain increment in one time step, an average strain rate of 1000/s was imposed during the test cases. This rate corresponds roughly to a 20% plastic strain in 0.2 milliseconds. The maximum time step corresponds to a single strain increment that is half of the generic material's yield strain. In this order of the strain increment, the integration algorithm performs well for the prediction of stresses under the different loadings. In an explicit FEA, in which small step sizes are used to ensure numerical stability, acceptable accuracy can be expected.

To show the effect of time step and corresponding strain increment on the integration method of the GYS model, single-element test cases undergoing uni-axial tension (see figure 57), uni-axial compression (see figure 58), and simple shear stress (see figure 59) were run at three different time steps. Because of high loading rate, inertial effects cause initial ringing in the stress plots for the uni-axial tension and compression test cases. Note that the magnitude of the oscillatory response is decreased using smaller time steps in the tension loading case.

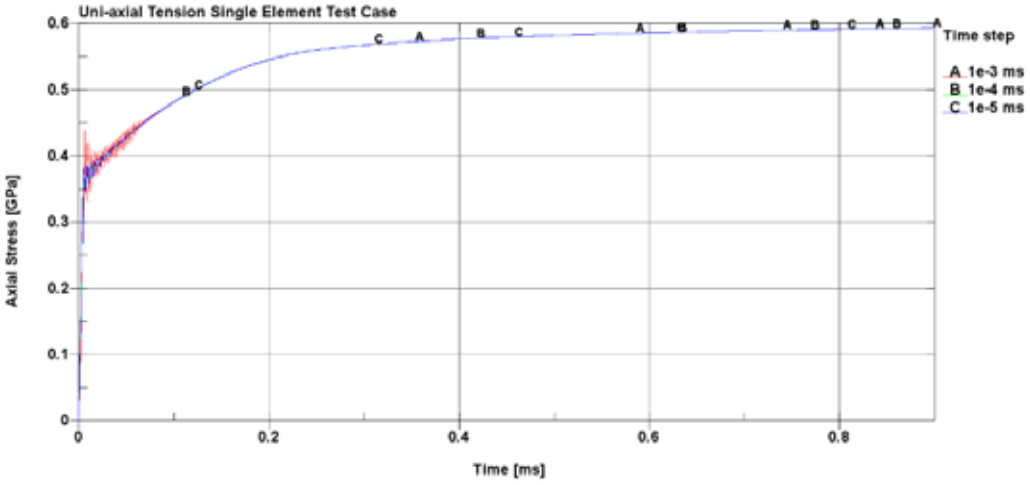

Figure 57. Effect of time step on GYS response—uniaxial tension case

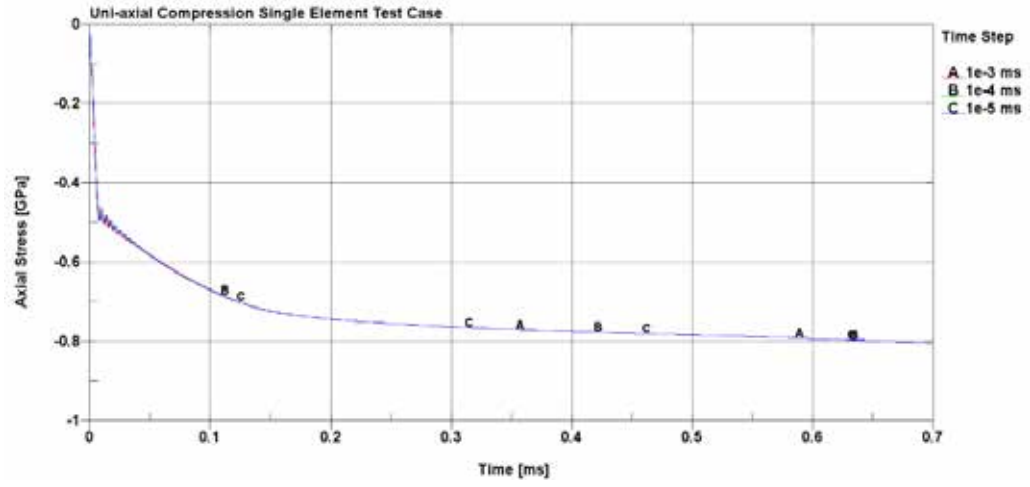

Figure 58. Effect of time step on GYS response—uniaxial compression case

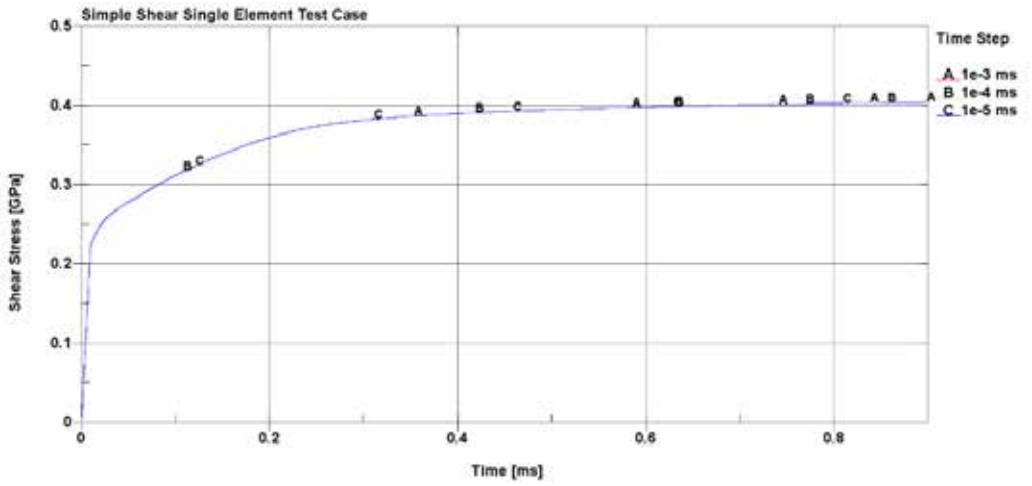

Figure 59. Effect of time step on GYS response—simple shear case

Single-element simulations, in which there was a change in the applied loading, partially through the analysis, and using different time steps, were also used to test the GYS implementation. Cases that began in uni-axial tension and switched to tension–biaxial tension (see figures 60 and 61) and that began in plane strain and switched to tension-uniaxial tension stress state (see figures 62 and 63) are presented. The same type of oscillatory response that occurred in the tension and compression cases occurs in these cases both initially and after the stress state changes suddenly at 0.15 ms (see figures 60–63). For all the cases, the stress converges to a smooth response for all time steps.

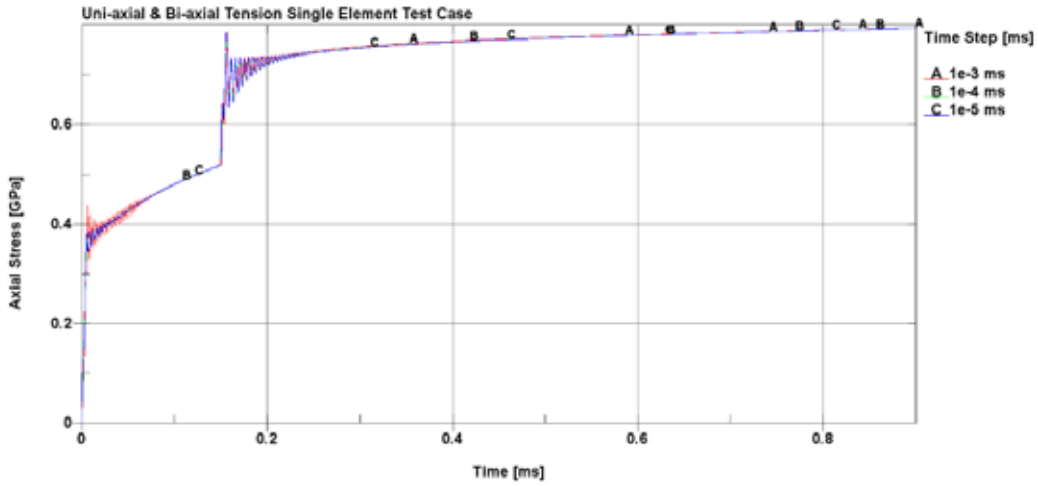

Figure 60. Effect of time step on GYS response loading case—uni-axial tension switching to bi-axial tension (axial stress)

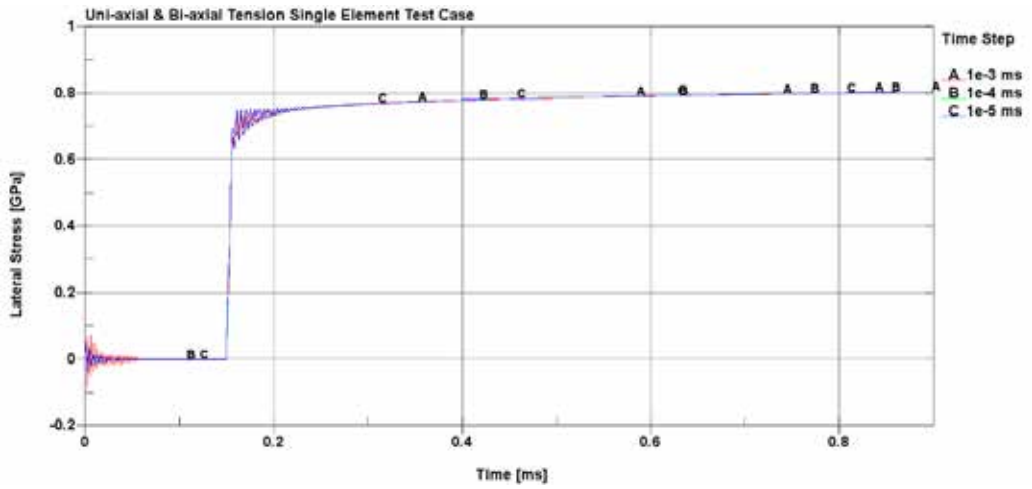

Figure 61. Effect of time step on GYS response loading case—uni-axial tension switching to bi-axial tension (lateral stress)

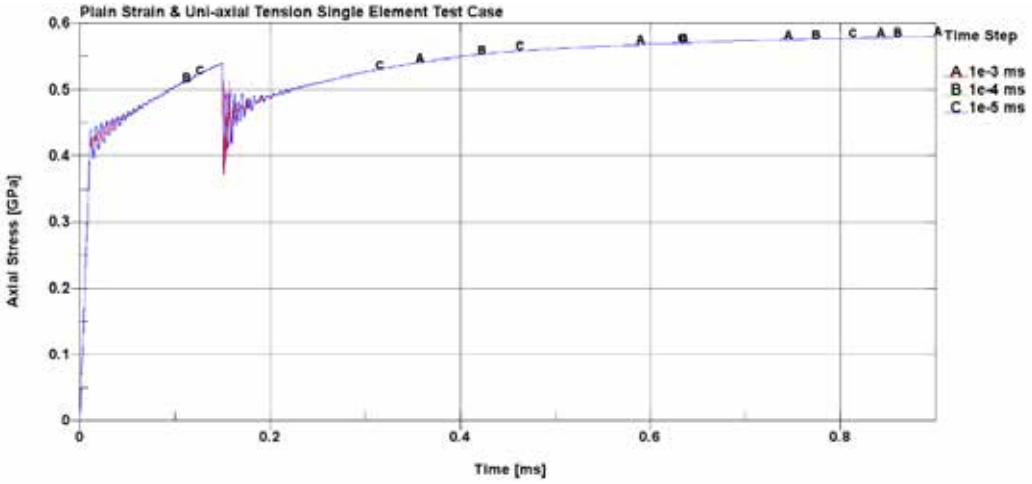

Figure 62. Effect of time step on GYS response loading case—plane strain tension switching uni-axial tension (axial stress)

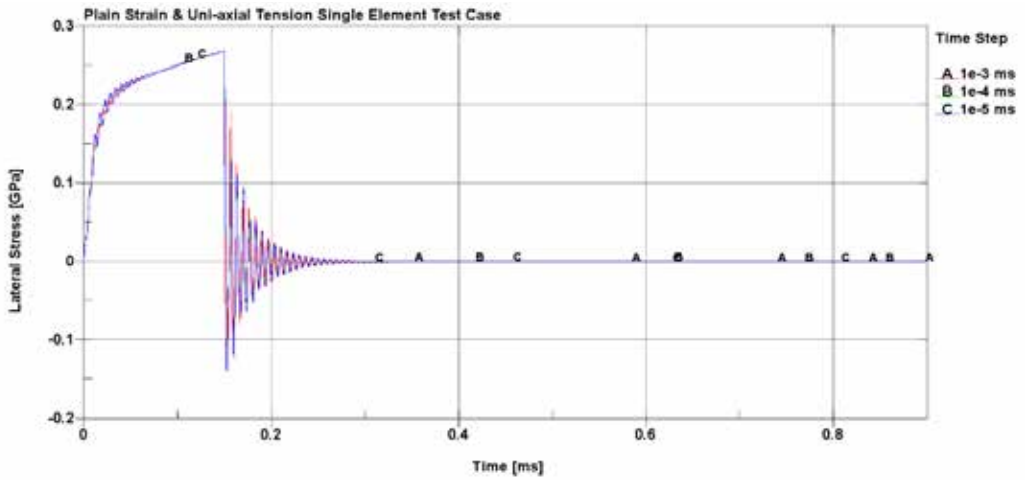

Figure 63. Effect of time step on GYS response loading case—plane strain tension switching uni-axial tension (lateral stress)

4.2 Single-Element Verification of the Convexity Projection Algorithm

The convexity algorithm of the GYS model, using the ratio of uni-axial compression to uni-axial tension and the ratio of shear to uni-axial tension as metrics, was presented in sections 3.7 and 3.8. Refer to figure 38 as a reminder of the projection algorithm. In the algorithm, the projection of the yield stresses and ratios onto the convexity boundary is tested using the cases presented in table 4. Details of verification Case 2, Case 3, Case 4, and Case 8 are presented in this section.

Table 4. Verification cases of projection algorithm for the dataset out of convexity region

CASE 1	CASE 2	CASE 3	CASE 4	CASE 5	CASE 6	CASE 7	CASE 8
YIELD RATIO	YIELD RATIO	YIELD RATIO	YIELD RATIO	YIELD RATIO	YIELD RATIO	YIELD RATIO	YIELD RATIO
$\frac{\sigma_c}{\sigma_t} = 1$ $\frac{\sigma_s\sqrt{3}}{\sigma_t} = 1$	$\frac{\sigma_c}{\sigma_t} = 1.8$ $\frac{\sigma_s\sqrt{3}}{\sigma_t} = 1$	$\frac{\sigma_c}{\sigma_t} = 0.5$ $\frac{\sigma_s\sqrt{3}}{\sigma_t} = 1$	$\frac{\sigma_c}{\sigma_t} = 1$ $\frac{\sigma_s\sqrt{3}}{\sigma_t} = 1.3$	$\frac{\sigma_c}{\sigma_t} = 1$ $\frac{\sigma_s\sqrt{3}}{\sigma_t} = 0.8$	$\frac{\sigma_c}{\sigma_t} = 1.3$ $\frac{\sigma_s\sqrt{3}}{\sigma_t} = 1$	$\frac{\sigma_c}{\sigma_t} = 0.7$ $\frac{\sigma_s\sqrt{3}}{\sigma_t} = 1$	$\frac{\sigma_c}{\sigma_t} = varying$ $\frac{\sigma_s\sqrt{3}}{\sigma_t} = 1$

Figure 64 shows Case 2, in which the yield ratio of uni-axial compression to uni-axial tension is 1.8. This ratio is above the maximum ratio (blue point), $\frac{\sigma_c}{\sigma_t}(\boldsymbol{max})$=1.693, of the convexity region. A graph of the effective stress versus effective plastic strain response for the single-element models in uni-axial tension and uni-axial compression is shown in figure 65 (a). Because of the projection of the dataset to the maximum ratio $\frac{\sigma_c}{\sigma_t}(\boldsymbol{max})$, the updated uni-axial compression to uni-axial tension yield ratio is expected to be 1.693, as described in section 3.8. The result is checked by applying a scale factor of 1.693 to the tension curve, as shown in figure 65 (b), with an exact match to the compression curve being obtained.

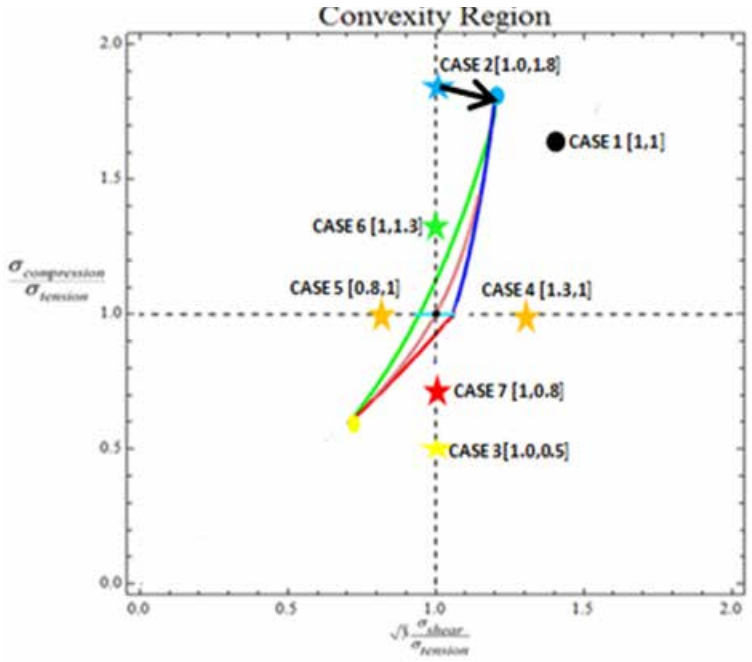

Figure 64. Case 2 (σ_c/σ_t = 1.8) and projection onto the convexity region

(a)

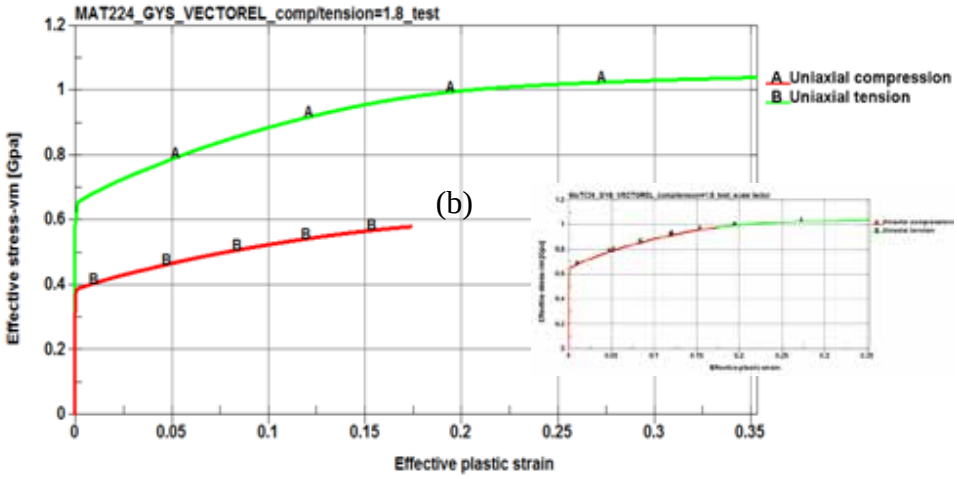

Figure 65. Case 2 (σ_c/σ_t = 1.8) (a) tension and compression effective stresses after the convexity correction, and (b) tension curve check using a scale factor of 1.693

Figure 66 shows Case 3, in which the ratio of uni-axial compression yield to uni-axial tension yield is 0.5. This ratio is below the minimum ratio (yellow point), $\frac{\sigma_c}{\sigma_t}(\boldsymbol{min})$=0.590, of the GYS convexity region. A graph of the effective stress versus effective plastic strain response for the single-element models in uni-axial tension and uni-axial compression is shown in figure 67 (a). Based on the projection of the dataset to the minimum ratio, the updated uni-axial compression to uni-axial tension yield ratio is expected to be 0.59, as described in section 3.8. This response is checked using a scale factor of 0.59 on the uni-axial tension curve, as shown in figure 67 (b), and an exact match to the uni-axial compression yield curve is obtained.

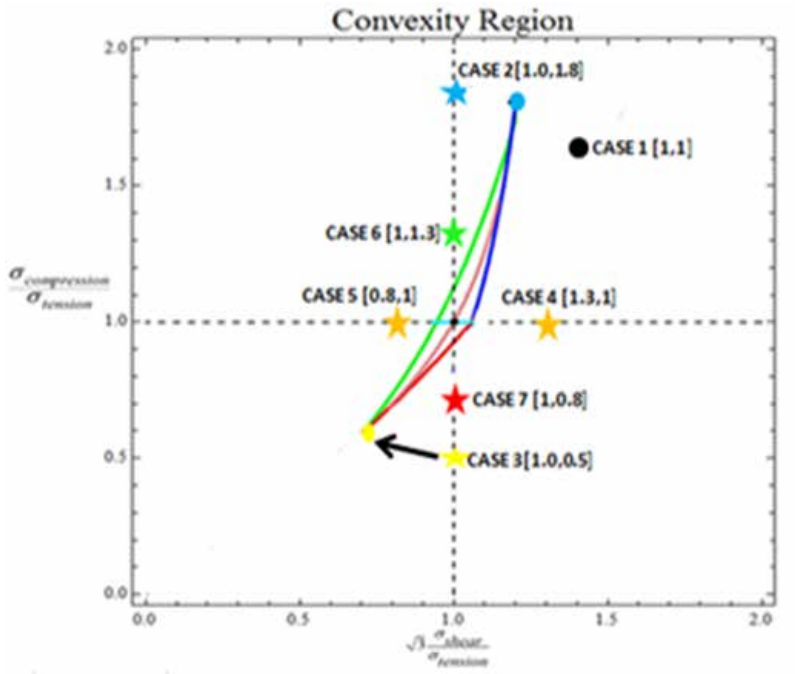

Figure 66. Case 3 (σ_c/σ_t =0.5) and projection onto the convexity region

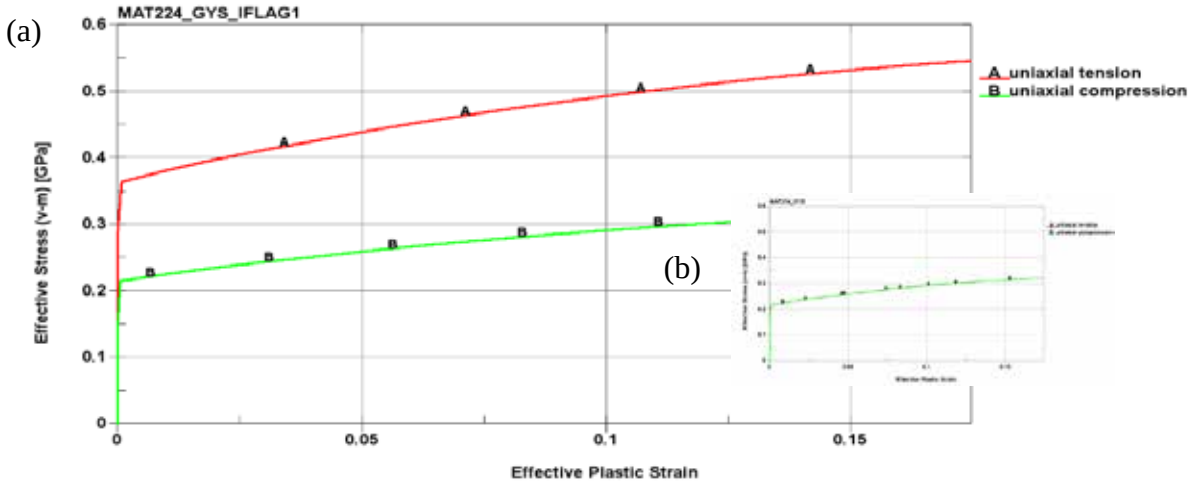

Figure 67. Case 3 (σ_c/σ_t = 0.5) (a) tension and compression effective stresses after the convexity correction and (b) tension curve check using a scale factor of 0.59

Figure 68 shows Case 4, in which $\sqrt{3}$ times the pure-shear to uni-axial tension yield ratio is 1.3, with $\frac{\sigma_c}{\sigma_t}$ =1.0 . This is outside the convexity limit of $\sqrt{3}\,\frac{\sigma_s}{\sigma_t}$ =1.0588, at $\frac{\sigma_c}{\sigma_t}$ =1.0. A graph of the effective stress versus effective plastic strain response for the single-element tests in uni-axial tension and pure shear is shown in figure 69 (a). Based on the projection of the dataset, the updated $\sqrt{3}$ times the pure-shear to uni-axial tension ratio is expected to be 1.0588, as described in section 3.8. The result is checked by applying a scale factor of 1.0588 to the tension curve, as shown in figure 69 (b), with an exact match to the compression curve being obtained.

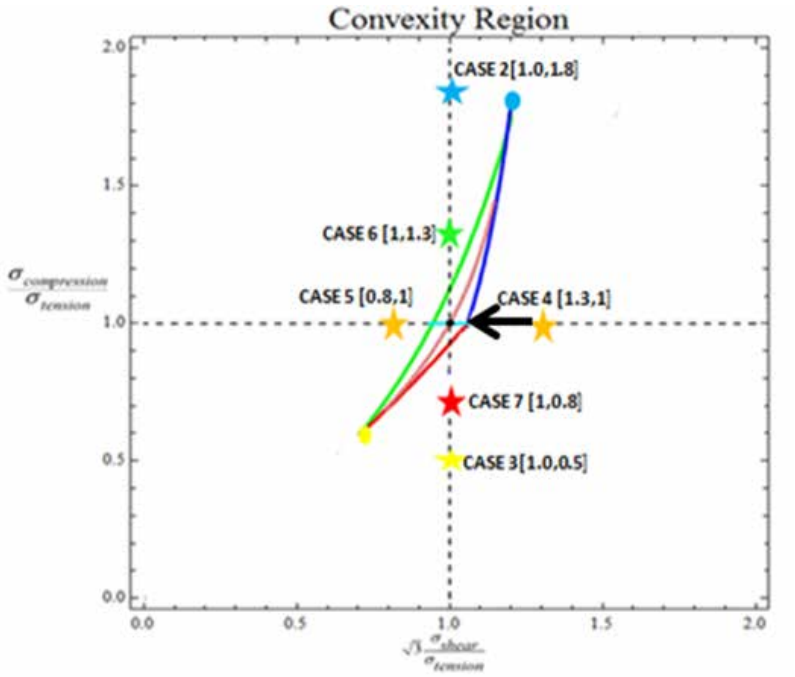

Figure 68. Case 4 ($\sqrt{3}\sigma_s/\sigma_t$ = 1.3) and projection onto the convexity region

(a)

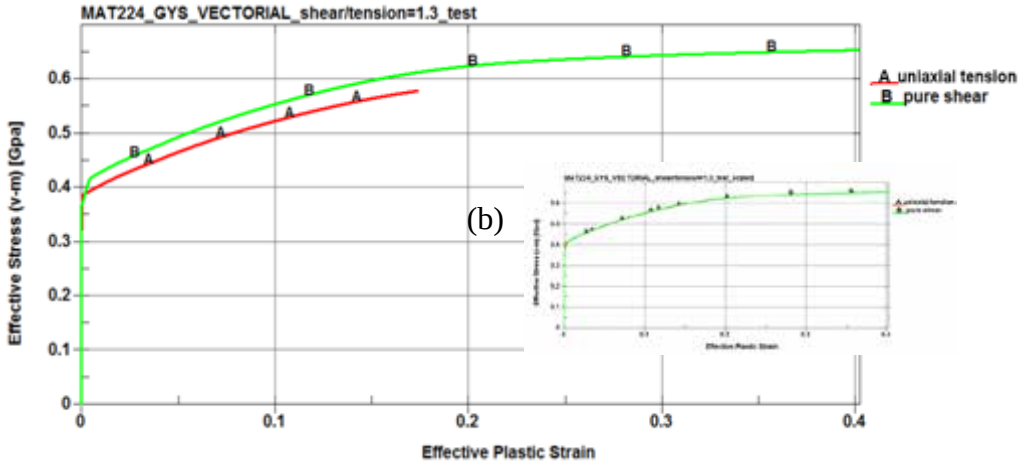

Figure 69. Case-4 ($\sqrt{3}\sigma_s/\sigma_t$ = 1.3) (a) tension and pure shear effective stresses after convexity correction, and (b) tension curve check using a scale factor of 1.0588

Figure 70 shows Case 8, in which the ratio of compression yield to tension yield varies from 0.3 to 2.29 (before being corrected for convexity), and $\sqrt{3}$ times the shear to tension yield ratio is 1. This range of ratios is partially outside the convexity region. A graph of the effective stress versus effective plastic strain response for the single-element tests in uni-axial tension and uni-axial compression is shown in figure 71 (a). Projection onto the convexity surface is performed for the ratios below the minimum (0.59) and above the maximum (1.69) of the convexity region, at $\sqrt{3}\frac{\sigma_s}{\sigma_t}$ =1.0. Between the minimum and maximum convexity ratios, no projection is performed, and the compression curve remains as shown in figure 70. Based on the projection when the ratio is

above the maximum, the compression to tension yield ratio is limited to 1.69. This response is checked using scale factor of 1.69 on the tension curve, as shown in figure 71 (b), and it can be seen that the result will be this correct ratio. Based on the projection of the dataset below the minimum, compression-to-tension yield ratio is expected to be 0.59. This response is checked using scale factor of 0.59 on the tension curve as shown in figure 71 (c) and an exact match with the uni-axial compression curve is obtained.

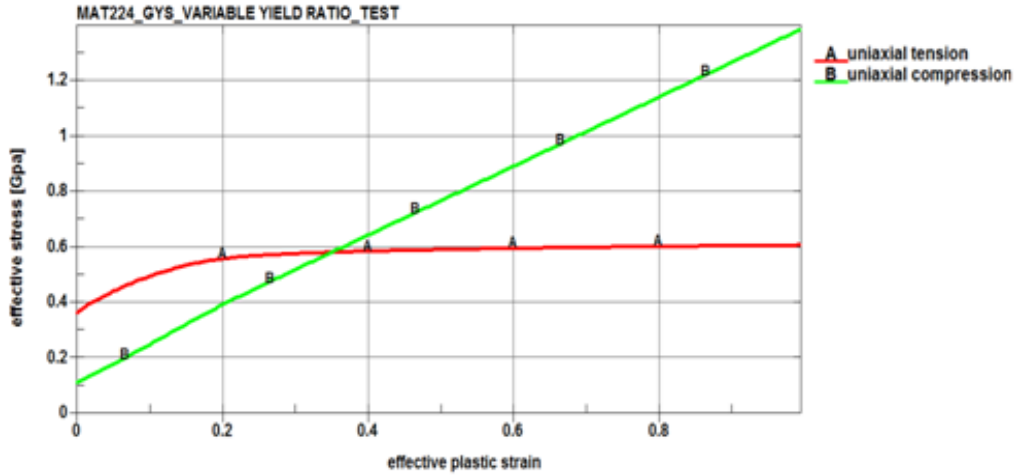

Figure 70. Case 8 (σ_c/σ_t = 0.3 to 2.29) uni-axial tension and uni-axial compression effective stresses without convexity correction

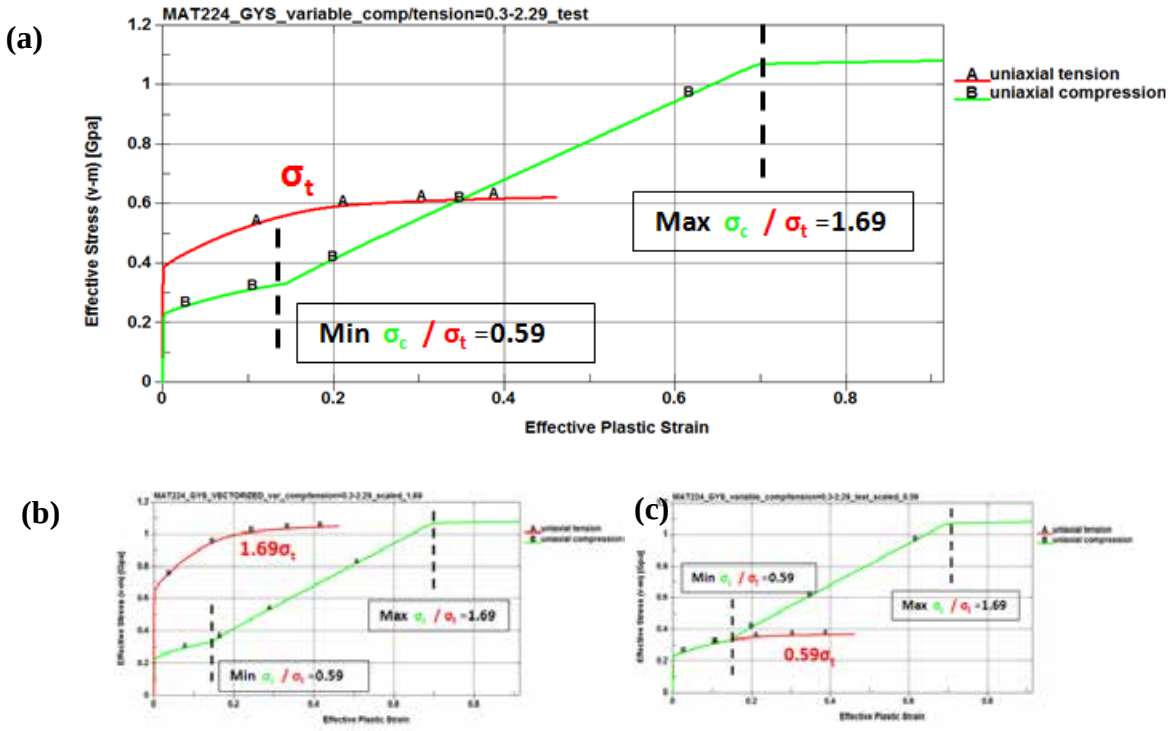

Figure 71. Case 8 (σ_c/σ_t = 0.3 to 2.29) (a) tension and pure shear effective stresses with convexity correction, (b) tension curve check using a scale factor of 1.69, and (c) tension curve check using a scale factor of 0.59

4.3 Comparison of MAT224 and MAT224_GYS Failure-Related History Variable Output

As another test of the MAT224_GYS implementation, history variable output from it was compared to the corresponding output from a MAT224 model using comparable input. The MAT224_GYS uses the same element erosion criteria as MAT224. A MAT224_GYS model using the same tension and compression input curves, and an input shear curve that was $1/\sqrt{3}$ times the tension input curve, and therefore reproduces a von Mises plasticity model, was created. Both the MAT224 and MAT224_GYS models used the same failure surface. Therefore, the results from the MAT224 and MAT224_GYS models are directly comparable.

Figure 72 shows the loading cases and evolution of the stress-state values. The results were compared for single-element test cases undergoing uni-axial tension (see figure 73), plane strain tension (see figure 74), and a non-proportional loading case combining plane strain tension and uni-axial tension (see figure 75). The history variable output that was compared are parameters related to the element erosion criteria. They are: plastic strain to failure, damage, tri-axiality, and effective stress. It is shown that the failure parameters from the MAT224 and MAT224_GYS models match (see figures 73–75).

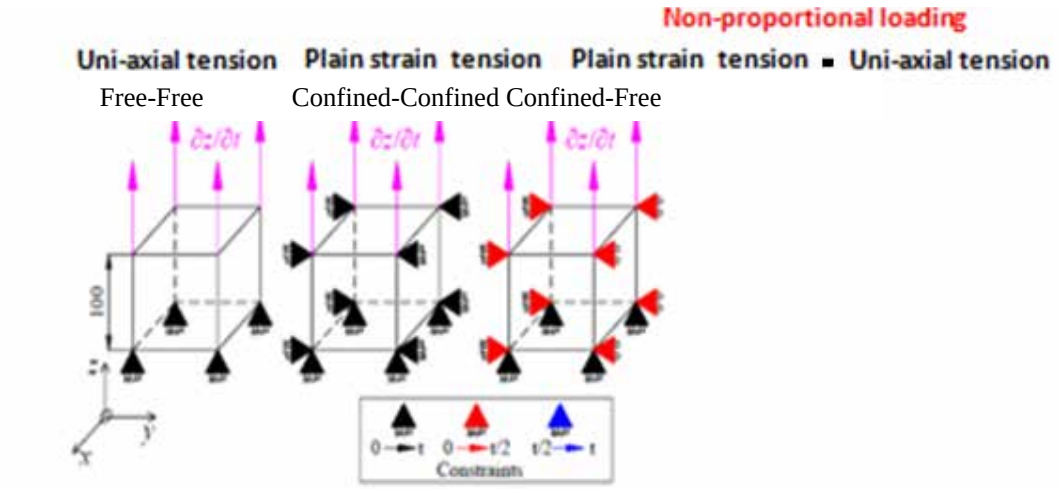

Evolution of the Stress-State Values

Loading Conditions	Stress tri-axiality σ^* $t=0 \rightarrow \frac{t}{2}$	Stress tri-axiality σ^* $t=\frac{t}{2} \rightarrow t$	Lode parameter θ_L $t=0 \rightarrow \frac{t}{2}$	Lode parameter θ_L $t=\frac{t}{2} \rightarrow t$
Free-Free	-0.333	-0.333	+1.0	+1.0
Confined-Confined	-0.577	-0.577	0.0	0.0
Confined-Free	-0.577	-0.333	0.0	+1.0

Figure 72. Loading cases and evolution of the stress-state values

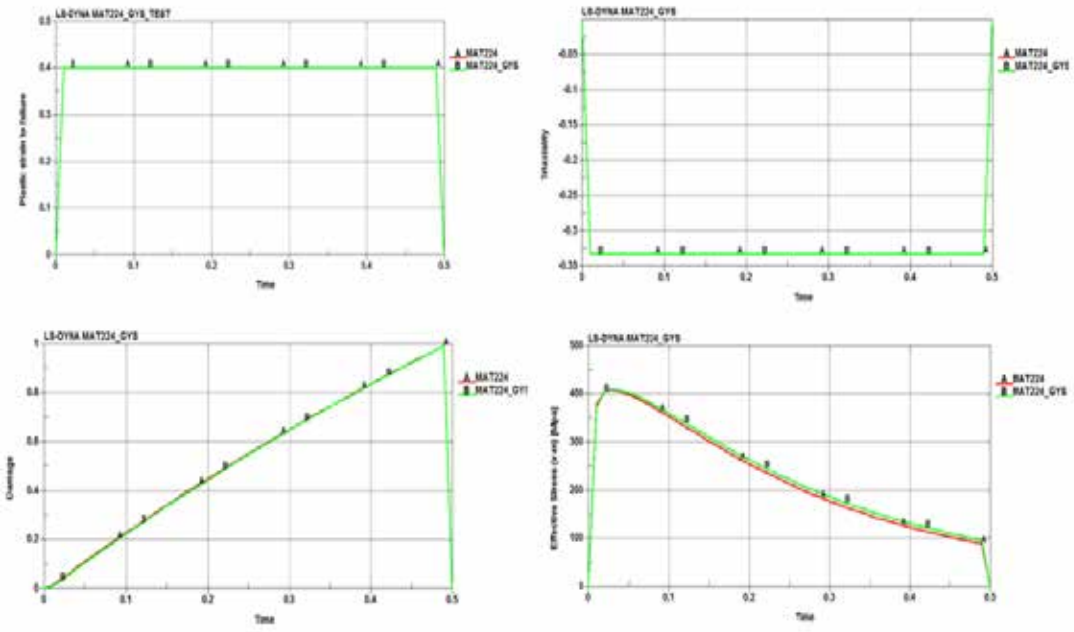

Figure 73. Uni-axial tension case—plastic strain to failure, damage, triaxiality, and effective stress

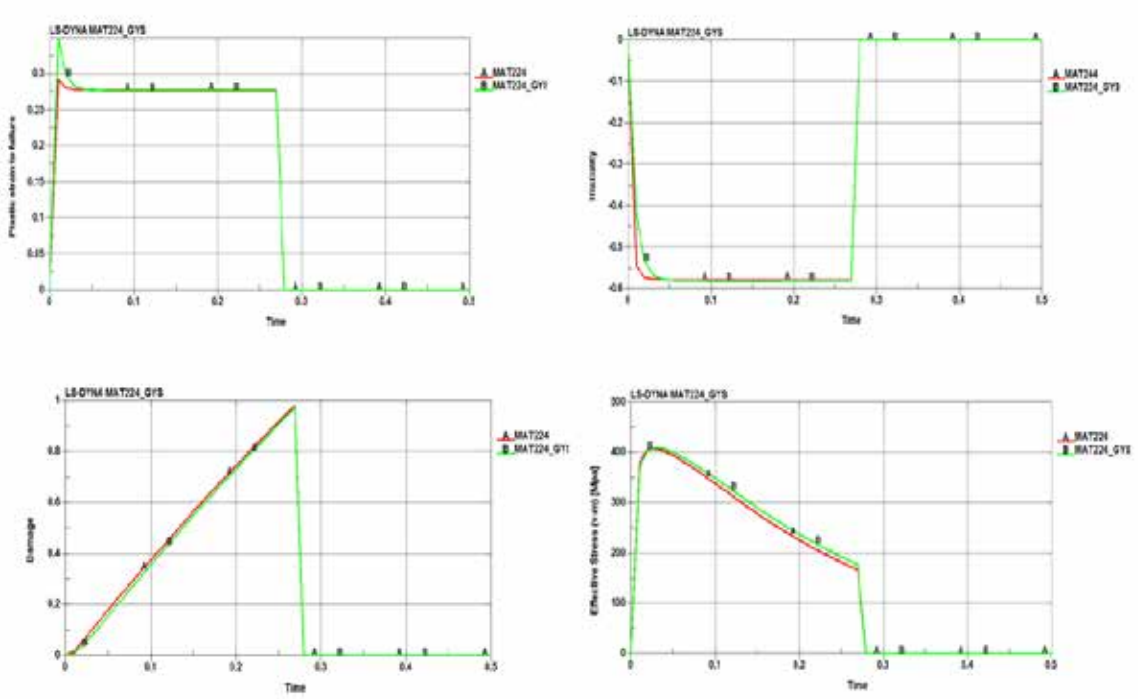

Figure 74. Plane strain tension case—plastic strain to failure, damage, triaxiality, and effective stress

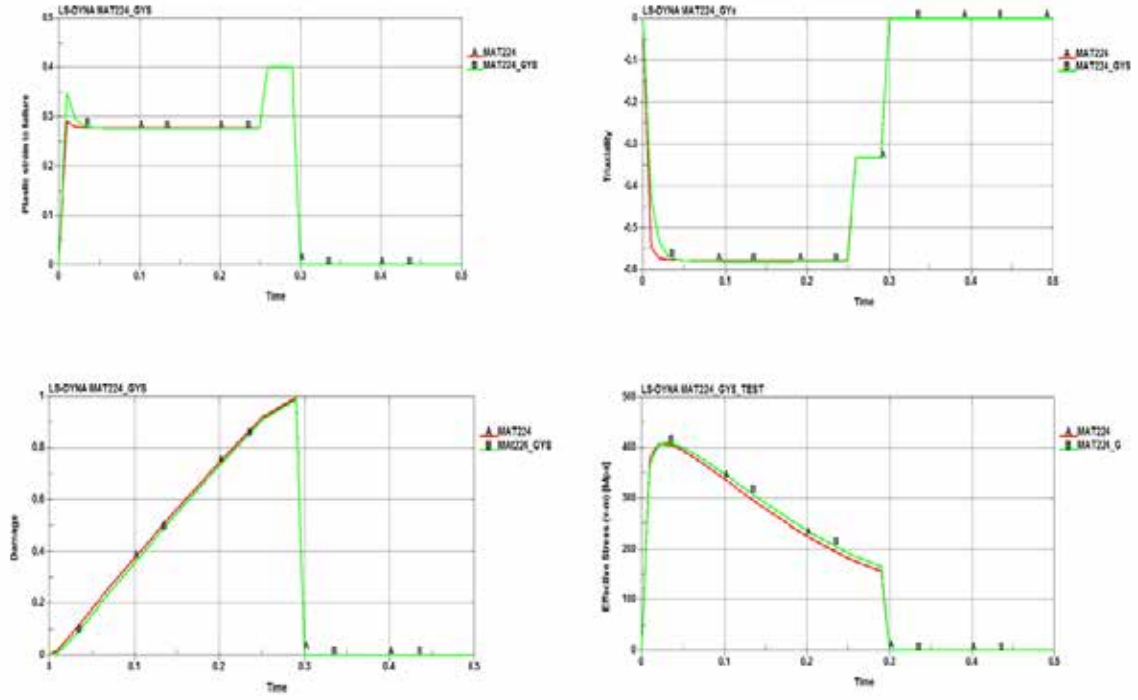

Figure 75. Non-proportional loading case (uni-axial tension-plane strain tension) case—plastic strain to failure, damage, triaxiality, and effective stress

5. APPLICATION OF THE GYS USING A TI-6AL-4V PLATE

5.1 The Application Example

The selected example is a 0.25-inch plate of titanium alloy derived from experimental testing conducted at the Ohio State University (Hammer, 2012). Ti-6Al-4V has tension-compression asymmetry in plasticity (see figure 76). Because of the asymmetry, this is an appropriate sample to demonstrate the use of MAT224_GYS. The rate- and temperature-dependent hardening laws need to be defined separately in the tension and compression directions. The suggested techniques for preparing this input for MAT224_GYS are presented in this section. (Wang, et al., 2018)

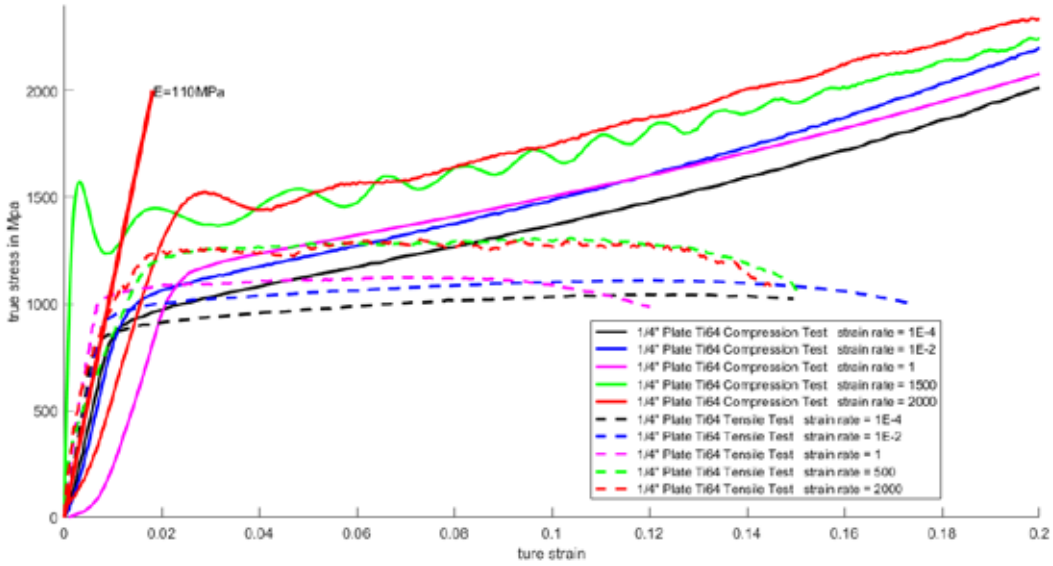

Figure 76. Experimental results of tension compression asymmetry for 0.25-inch Ti-6Al-4V plate under different strain rates (force displacement relation is normalized to true strain and true stress with classical formula to contour the geometric difference)

Figures 77–78 show the Ti-6Al-4V uniaxial tension and compression tests, at a strain rate of 0.01 1/sec and at room temperature, versus simulation results using the MAT_224_GYS and von Mises (MAT_224) plasticity models. Both numerical models match the test data from the uni-axial tension test, as shown in figure 77. However, von Mises plasticity, whereas initially matching the yielding as shown in figure 78, cannot duplicate the compressive behavior, eventually resulting in an error in force of more than 10%. In contrast, GYS matches the complete compression force and displacement test data, as shown in figure 78.

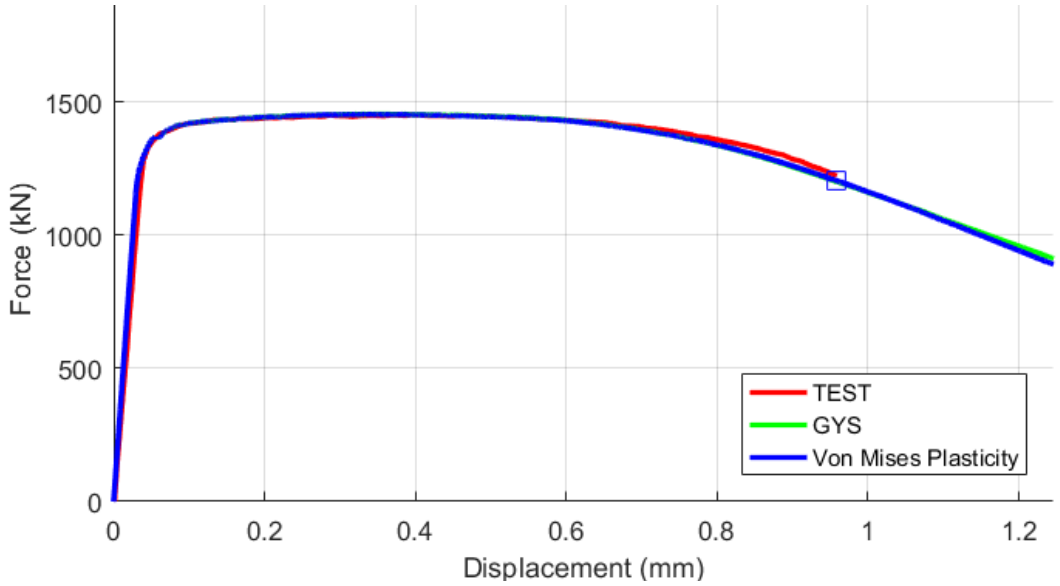

Figure 77. Ti-6Al-4V uniaxial tension test and simulation at strain rate = 0.01 (1/s), test: M2-TMT-P3-SG1-O1-SR2-T1-N3

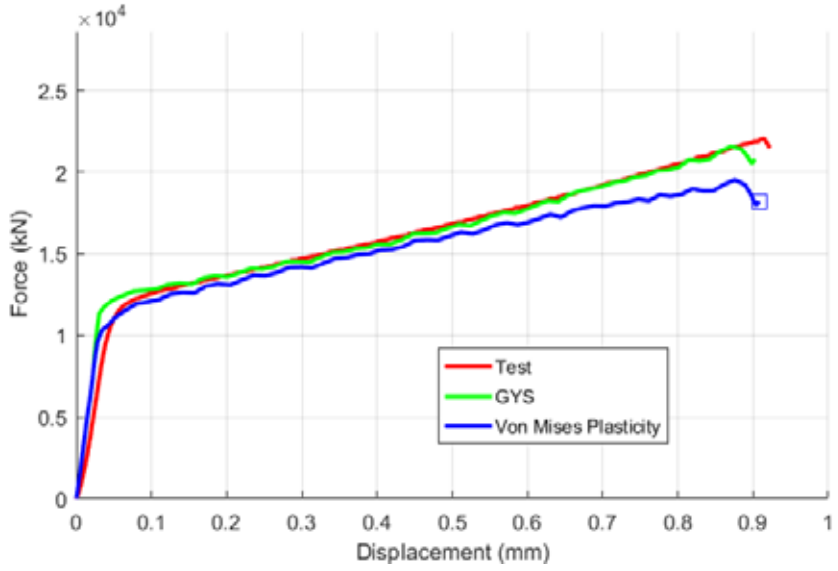

Figure 78. Ti-6Al-4V uniaxial compression test and simulation at strain rate = 0.01 (1/s), test: M2-TMC-P3-SG1-O1-SR2-T1-N1

5.2 Material Model Input Generation

The available mechanical test data for the 0.25-inch titanium plate are summarized here. Tension and compression test series are carried out using five strain rates and five temperatures. A shear test series was not performed on this plate; therefore, the shear table was not defined on the MAT224_GYS. Compression curve fitting and tension curve fitting are carried out in sequence. It is important to note that the nominal strain rate is used only to categorize the test. It does not represent the real strain rate of the material test. The real strain rate of each test is not constant.

Before necking, the strain rate of the test is not constant because of the limitations of the testing machine. After necking, the specimen is not uniform, and the strain rate in the necked area naturally has a much higher strain rate value. The strain rates defined in the tension and compression input tables are related to the curves, which result from the trial and error iterations of their creation. They do not directly relate to the nominal strain rate.

5.2.1 Compression Test Simulations

The compression tests with different strain rates and temperatures were simulated using LS-DYNA Revision 8.0, MPP, and double precision. A solid cylindrical specimen placed on a stationary platform is compressed with another moving platform (see figure 79). A linear elastic material model with steel material properties is used for the platforms. The fixed and moving boundary condition constrains only the very top and bottom nodes of the moving and stationary platforms, respectively. The elastic platform allows some deformation, which approximates the test condition. The contact surfaces for both the platforms and the specimen are wrapped with a layer of null shell elements to improve the contact performance.

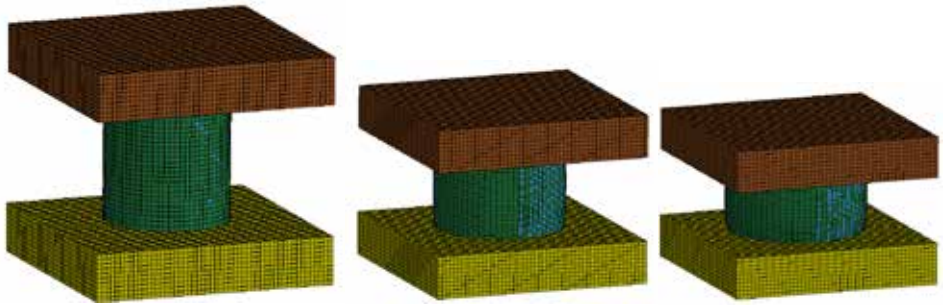

Figure 79. Compression simulation setup

*CONTACT_AUTOMATIC_SINGLE_SURFACE is used to define the contact between the null shell elements. A static coefficient of 0.05, dynamic coefficient of 0.04, and exponential decay coefficient of 0.001 are used to model the friction between the specimen and platforms. These parameters are chosen such that the deformed “barrel” shape of the simulation is similar to that of the test (see figure 80). The specimen and the platform are modeled with reduced integrated solid element (ELFORM = 1) with hourglass control number 6.

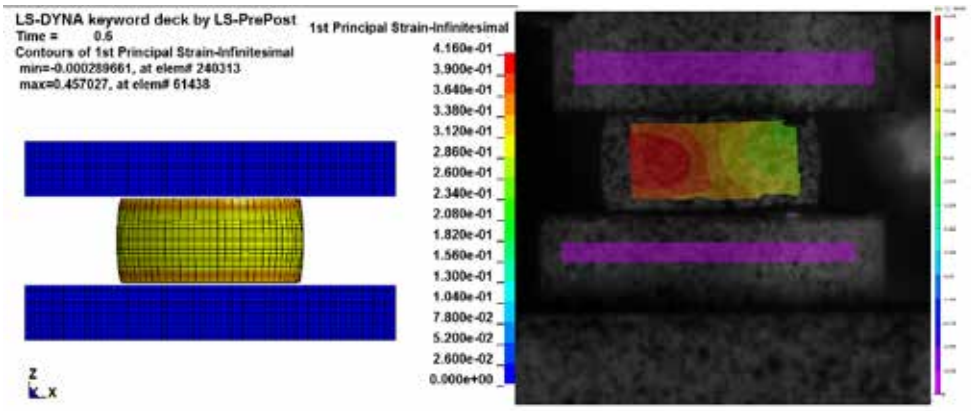

Figure 80. The first principal strain contour between test and simulation and the barrel shape comparison

5.2.2 Tension Test Simulations

The tension specimen has the shape of a dog-bone (see figure 81). For lower strain rate tests of 1.E-4 (1/s), 1.E-2 (1/s), and 1. (1/s), the test is performed using an Instron test frame. The moving grip at the top pulls the specimen upward, whereas the bottom grip holds the specimen fixed. The force is measured by the test frame, and the displacement is measured by digital image correlation (DIC). Data were provided at a virtual strain gauge with a length of 4 mm, which is marked with a white dot in figure 81. Notice that the displacement was provided at the 4 mm virtual strain gauge points, not at the end of the specimen where the grip is fixed. In the low rate test simulations, the displacement boundary condition was specified at the end of the test section of the specimen (at the edge of the picture in figure 81). This difference in boundary condition locations makes little difference for the lower strain rate cases.

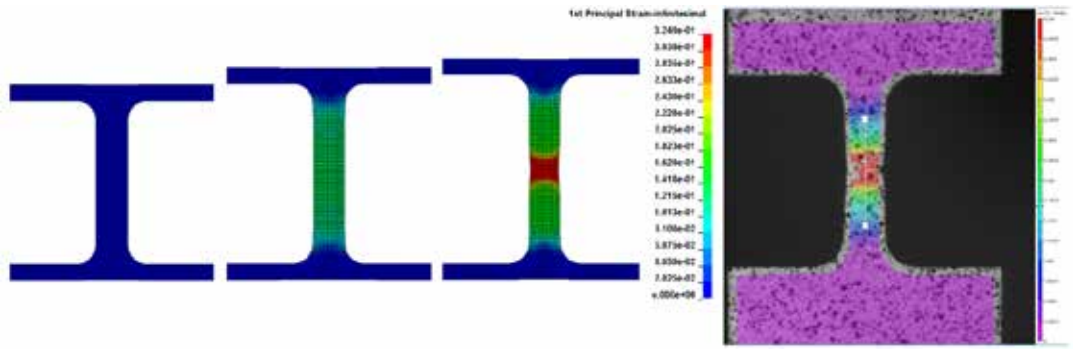

Figure 81. Simulation setup (left) and the test photo with virtual DIC 4 mm apart (right)

For higher strain rates of 500 (1/s) and 1000 (1/s), the tests are performed on a split Hopkinson bar. Because the dynamics effects are large in a split Hopkinson bar test, a small change in boundary conditions may cause large differences in the strains of the necking region. In split Hopkinson bar tests, the constrained end of the test specimen is usually not completely fixed. Therefore, for the higher strain rate tests, the boundary conditions were applied directly at the 4-mm virtual DIC point. The test and simulation displacements were also compared at these points.

5.3 Example Fitting Result

The material model input is built using the iterative method described in the report describing the development of a MAT224 Titanium model (FAA, 2016). The example analysis shown in this section (5.3) yields an overall good agreement with the test. Each test condition had three test repeats. One of the three available tests for each condition was selected to compare to the simulation. The force versus displacement plots, and the strain contours from DIC, are compared for three tests and simulations.

As presented in section 5.2.2, in the tension high-strain rate tests (500 (1/s) and 1000 (1/s)), the boundary conditions are placed directly on the DIC points. For the compression tests, the displacement is measured at the platform.

In figure 82, the input tables of the MAT224_GYS material model for the 0.25-inch Ti-6Al-4V plate are plotted. All the presented results used this input model, and are labeled "aa12_attempt_22" in the figures. Tests and simulations are compared for tension strain rate series (see figure 83), tension temperature series (see figure 84), compression strain rate series (see figure 85), and the compression temperature series (see figure 86), and are presented in this section. For the tension tests at elevated temperatures, (note in figure 84), there a mismatch with the test in the -50°C simulation at 1 (1/s) strain rate. It is possible that the test is neither isothermal nor adiabatic, and therefore would require a coupled mechanical thermal solution to simulate.

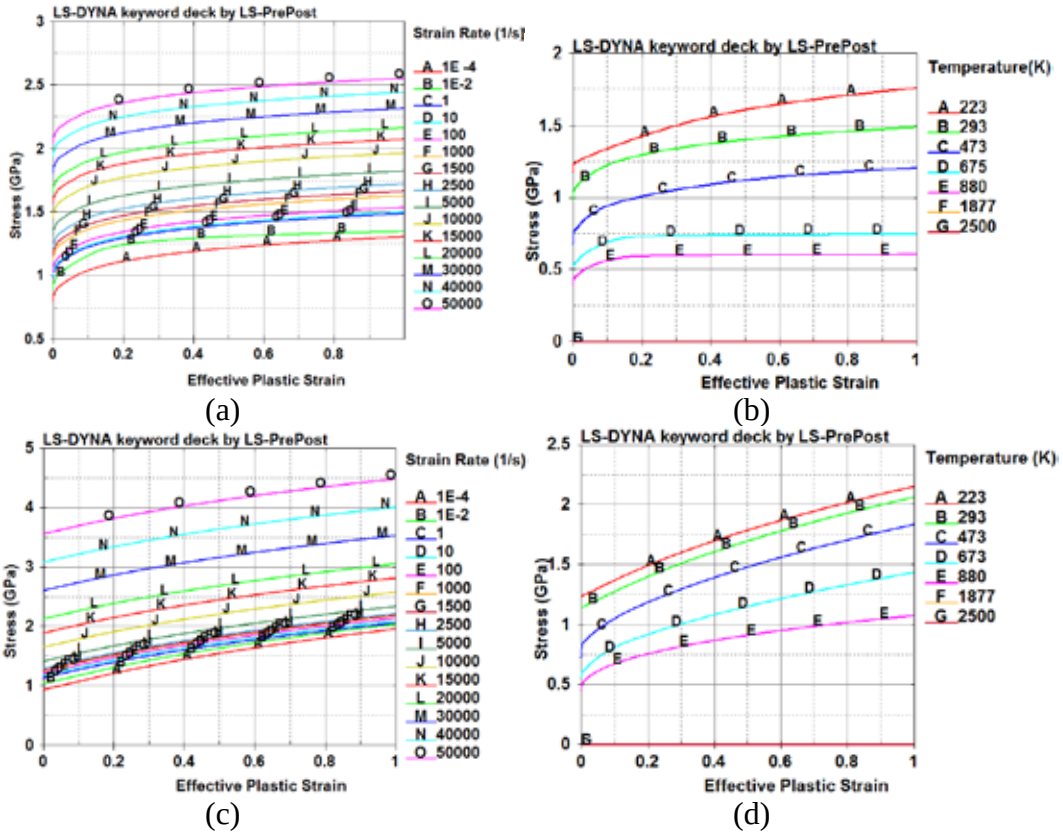

Figure 82. MAT_224_GYS input curves for 0.25-inch Ti-6Al-4V plate: (a) tension strain rate table, (b) tension temperature table, (c) compression strain rate table, and (d) compression temperature table

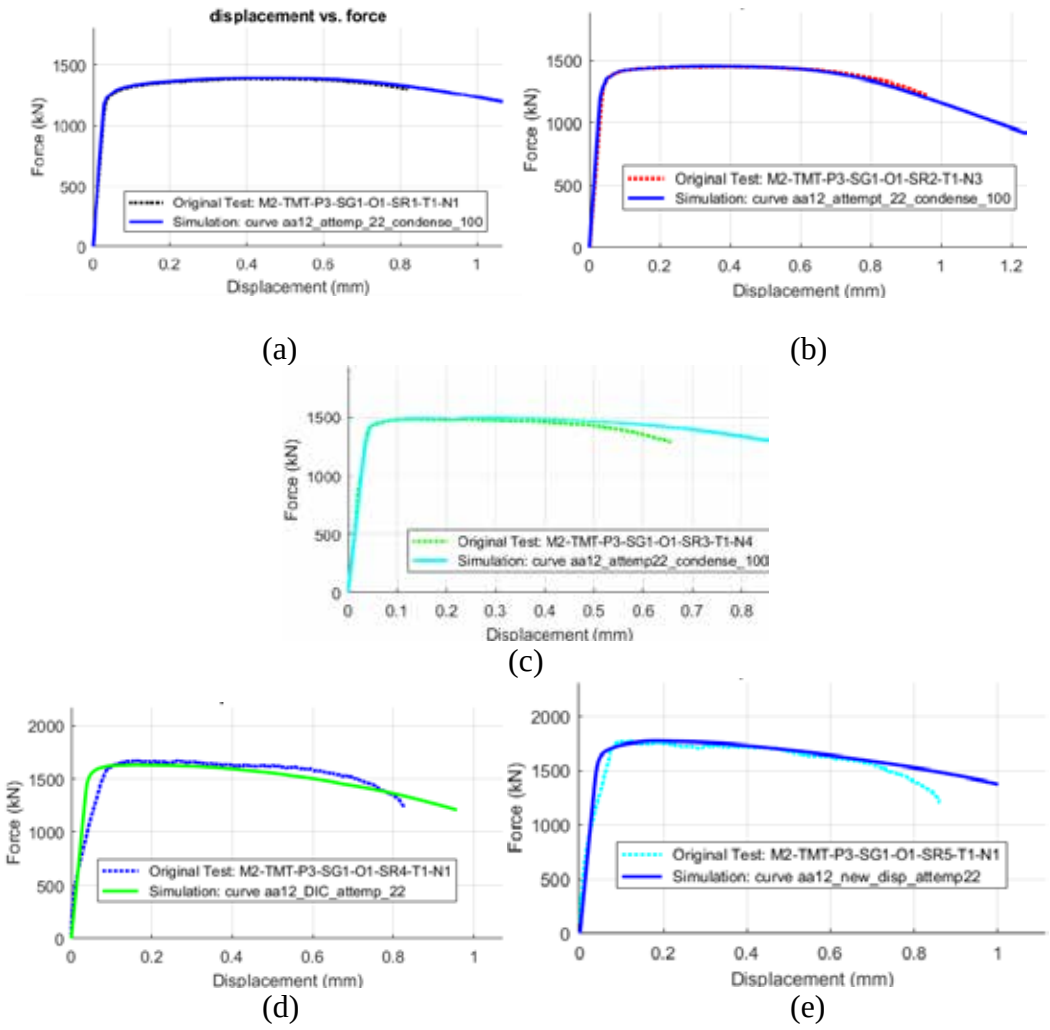

Figure 83. Simulation and test data comparison for Tension Strain Rate Series: (a) 1E-4 (1/s) strain rate test, (b) 1E-2 (1/s) strain rate test, (c) 1 (1/s) strain rate test, (d) 500 (1/s) strain rate test, and (e) 1000 (1/s) strain rate test; strain rate labels are nominal, actual strain rate varies for each test; all tests are at room temperature

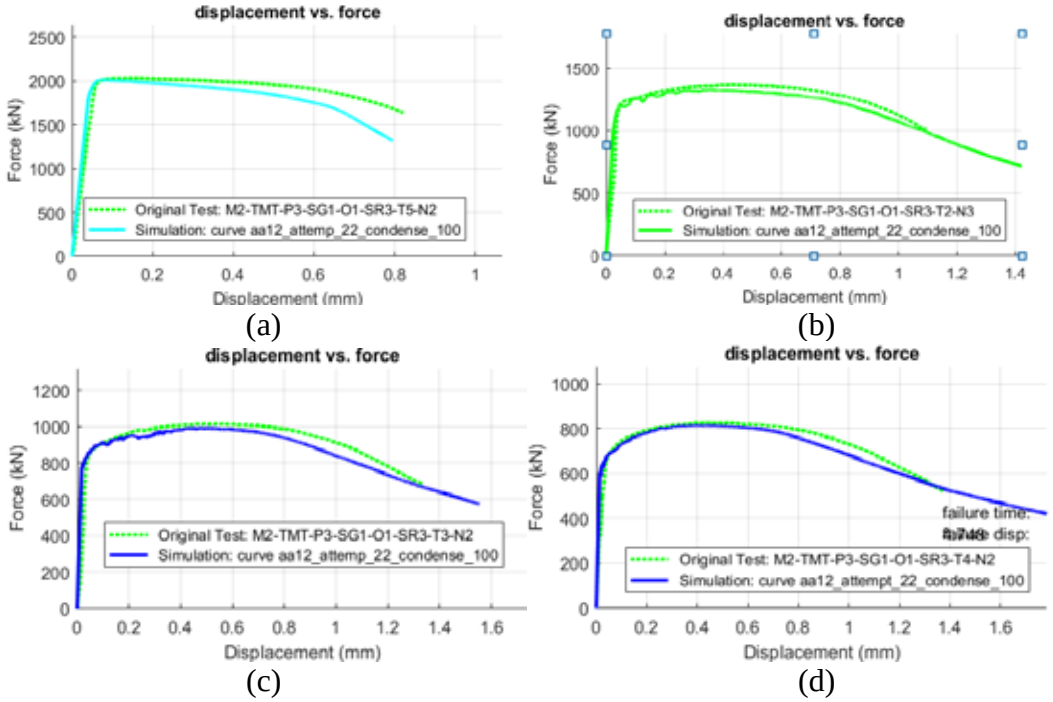

Figure 84. Simulation and test data comparison for Tension Temperature Series: (a) -50 °C, (b) 200 °C, (c) 400 °C, and (d) 600 °C; all tests are done at nominal strain rate = 1 (1/s)

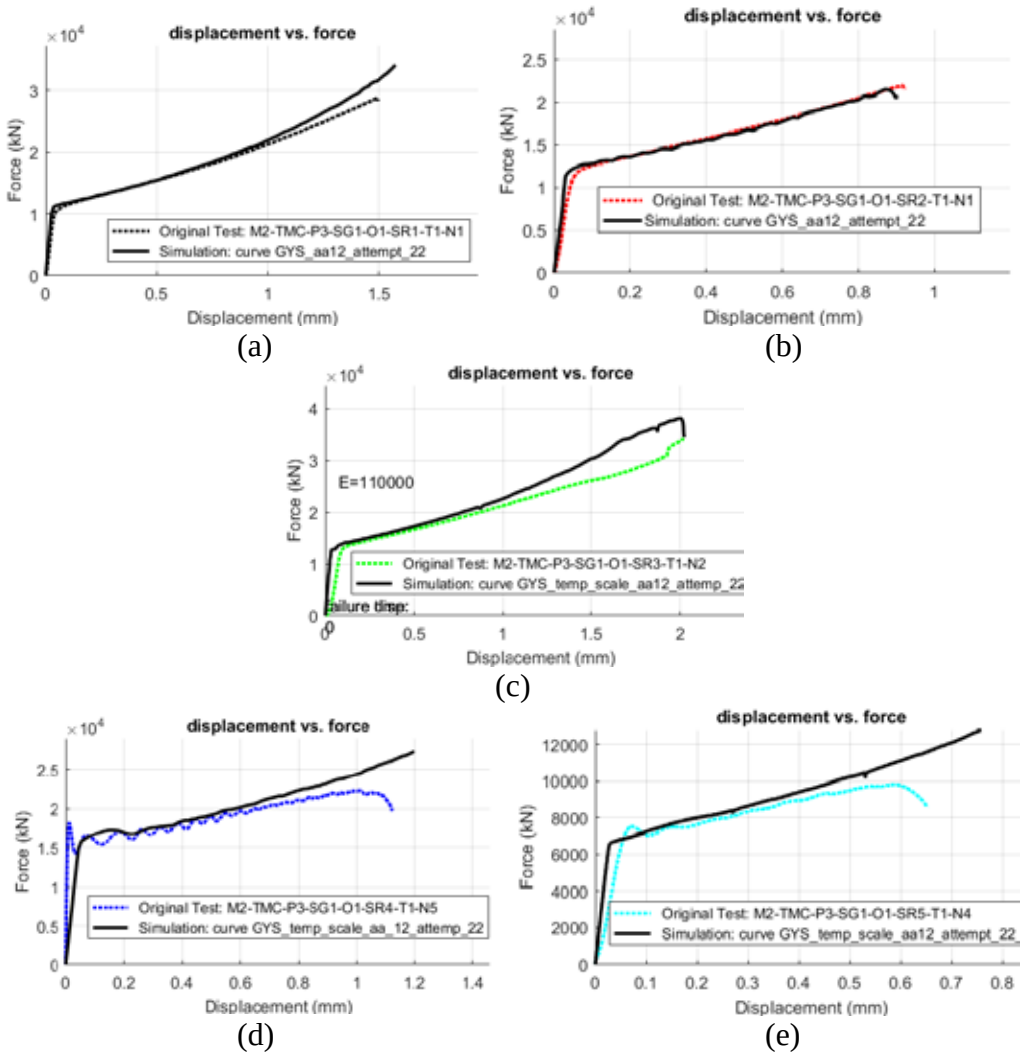

Figure 85. Simulation and test data comparison for compression strain rate series: (a) 1E-4 (1/s) strain rate test, (b) 1E-2 (1/s) strain rate test, (c) 1 (1/s) strain rate test, (d) 500 (1/s) strain rate test, and (e) 1000 (1/s) strain rate test; strain rate labels are nominal; actual strain rate varies for each test; all tests are at room temperature

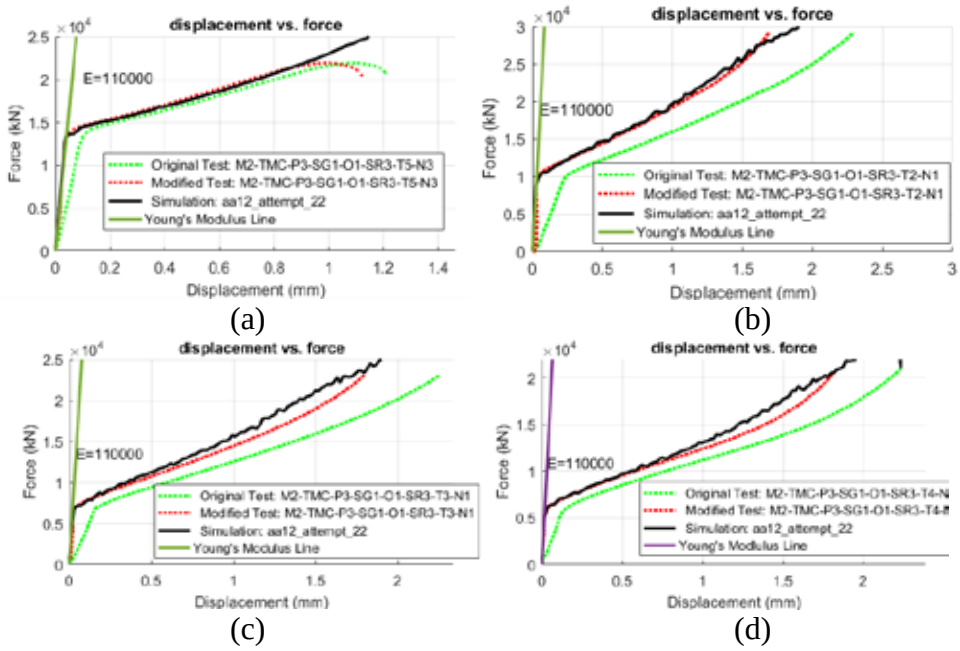

Figure 86. Simulation and test data comparison for Compression Temperature Series: (a) -50°C, (b) 200°C, (c) 400°C, and (d) 600°C; all tests are done at nominal strain rate = 1 (1/s).

5.4 Application Summary

It is demonstrated that the MAT224_GYS is suitable to model the tension-compression asymmetry observed in 0.25-inch Ti-6Al-4V plate. The presented results demonstrate that a single input deck is able to predict all of the material tests that were conducted using different strain rates and temperatures in both tension and compression. MAT224_GYS is able to model the differing strain rate and temperature sensitivities of the titanium.

6. SUMMARY

An isotropic, elasto-plasticity model has been presented that has a yield function with greater capabilities and flexibility than previously existing models. The Generalized Yield Surface (GYS) can incorporate both tension and compression yielding and plasticity asymmetry, and deviations from the von Mises theory shear to tension yield stress ratio. In GYS, the tension, compression, and shear plasticity behaviors are all separately both temperature-dependent and strain-rate-dependent, and the model uses additive decomposition of the strain rate. The strain rate, temperature, strain, and load-dependent hardening parameters c_1, c_2, c_3, and σ_y, are updated individually at every time-step. This means that the yield surface is not limited to self-similar hardening as most previously existing models. This distortional hardening allows the yield surface to both expand and deform.

To allow for distortional hardening, the yield function is written differently than most previously existing plasticity models. In previous models, the yield function is typically written with the

effective stress as a function of the stress tensor, and the yield stress as a function of the plastic multiplier. In GYS, the effective stress is not only a function of the stress tensor, but also a function of the plastic multiplier (i.e., the GYS effective stress is dependent on the hardening parameters c_1, c_2, c_3, and σ_y, which are dependent on the plastic multiplier, λ).

The distortional hardening in GYS allows for the compression and tension plasticity to vary to the extent that, initially, the tension may have a higher yield than the compression, but as the loading evolves, the compression may become greater than the tension yield stress. Such behavior has been observed in tests and, therefore, modeling this type of behavior is important for accurate predictions. The capability of modeling such behavior sets GYS apart from other plasticity models.

The requirement for a convex yield surface to obtain a unique solution puts conditions on the extent to which asymmetry or deviations from the von Mises shear-to-tension yield ratio may be accommodated. The convexity region of the newly developed GYS model has been presented and compared to existing plasticity models. In the implementation, the input data are automatically modified to maintain convexity.

As an example to potential users of MAT224_GYS, a specific Ti-6Al-4V plate was modeled. The mechanical property tests of this plate were conducted at a variety of temperatures and strain rates. In this plate, the asymmetry in tension and compression yielding was pronounced. Good matches between the uni-axial tension and uni-axial compression mechanical property test data and the analysis, using MAT224_GYS, were presented. Including the asymmetry in tension and compression yielding, which cannot be modeled in classical von Mises plasticity, was essential in obtaining good matches. Including the strain-rate-dependent and temperature-dependent plasticity was also essential in the successful simulation of the experiments.

The presented work is the first step of model verification. The next step is to use MAT224_GYS, including failure, for the modeling of ballistic impact tests. In impact analysis, both tension and compression plastic response must be captured accurately to predict the deformation and failure over a range of different impact velocities and projectile shapes. In addition, the shear response is important in many impact problems; therefore, the flexibility to simulate a range of shear to tension yield ratios will also be important for successful predictions. To model failure, element erosion criteria for the example Ti-6Al-4V plate, which includes stress-state, strain rate, and temperature dependency, will be created. A direct comparison, based on the projectile exit velocity and ballistic limits, of ballistic impact test results with the analysis using the final material model will be performed. On successful verification, the GYS will be ready to be used in the intended application of fan blade containment analysis.

7. REFERENCES

Backman, M. E. (1976). “Terminal Ballistics.” Naval Weapons Center, (NWC TP 578).

Backman, M. E. and Goldsmith, W. (1978). The mechanics of penetration of projectiles into targets. *International Journal of Engineering Science, 16*(1), 1–99.

Bai, Y. and Wierzbicki, T. (2008). A new model of metal plasticity and fracture with pressure and Lode dependence. *International Journal of Plasticity, 24*(6), 1071–1096.

Becker, R. (2011). An alternative approach to integrating plasticity relations. *International Journal of Plasticity*, 27(8), 1224–1238.

Belytschko, T., Liu, W. K., Moran, B. (2000). *Nonlinear finite elements for continua and structures*. Somerset, NJ: John Wiley & Sons.

Berstad, T., Hopperstad, O. S., and Langseth, M. (1994). *Elasto-viscoplastic constitutive models in the explicit finite element code LS-DYNA3D*. In 2nd International LS-DYNA3D Conference, St. Francis, Loretto, PA.

Borvik, T., Hopperstad, O., Berstad, T., and Langseth, M. (2002). Perforation of 12 mm thick steel plates by 20 mm diameter projectiles with flat, hemispherical and conical noses, part I: experimental study. *International Journal of Impact Engineering, 27*(1), 19–35.

Bower, F. A. (2010). *Applied Mechanics of Solids*. Boca Raton, FL: CRC Press.

Bridgman P. W. (1952). *Studies in large plastic flow and fracture*. New York, NY: McGraw-Hill.

Buyuk, M., Kan, S., and Loikkanen, M. J. (2009). Explicit finite-element analysis of 2024-T3/T351 Aluminum material under impact loading for airplane engine containment and fragment shielding. *Journal of Aerospace Engineering, 22*(3), 287–295.

Buyuk, M. (2013). *Development of A Tabulated Thermo-Viscoplastic Material Model with Regularized Failure for Dynamic Ductile Failure Prediction of Structures under Impact Loading.* (PhD thesis). The George Washington University.

Carney, K. S., Du Bois, P. A., Buyuk, M., and Kan, S. (2009). A Generalized, three-dimensional definition, description, and derived limits of the triaxial failure of metals. *Journal of Aerospace Engineering, 22*(3), 280–286.

Cazacu, O., Barlat, F. (2001). Generalization of Drucker's yield criterion to orthotropy. *Mathematics and Mechanics of Solids, 6*(6), 613–630.

Cazacu, O., Barlat, F. (2004). A criterion for description of anisotropy and yield differential effects in pressure-insensitive metals. *International Journal of Plasticity, 20*(11), 2027–2045.

Chait, R., (1972). Factors influencing the strength differential of high strength steels. *Metallurgical and Materials Transactions B, 3*(2), 369–375.

Courant, R., Friedrichs, K., and Lewy, H. (1967). On the partial differential equations of mathematical physics. *IBM Journal of Research and Development, 11*(2), 215–234. English translation and republication of the 1928 German original "Mathematische Annalen 100, 32-74 (1928).

Drucker, D.C. (1949). Relation of experiments to mathematical theories of plasticity. *Journal of Applied Mechanics, 16*, 349–357.

Drucker, D. C. (1950). "A definition of stable inelastic material," Report to the Office of Naval Research. (NR-064-424).

Du Bois, P. A. (2012). "Lecture notes for plasticity in LS-DYNA."

Dunne, F., Petrinic, N. (2005). *Introduction to computational plasticity*. Oxford, England, UK: Oxford University Press.

FAA Report. (1999). Large engine uncontained debris analysis. (DOT/FAA/AR-99/11).

FAA Report. (2016). Development of a Titanium Alloy Ti-6Al-4V Material Model Used in LS-DYNA. (DOT/FAA/TC-15/23).

Gao, X., Zhang, T., Hayden, M., Roe, C. (2009). Effects of the stress state on plasticity and ductile failure of an aluminum 5083 alloy. *International Journal of Plasticity*, *25*(12), 2366–2382.

Gao, X., Zhang, G., Zhou J., Graham M. S., Hayden, M., Roe, C. (2010). On stress-state dependent plasticity modelling: significance of the hydrostatic stress, the third invariant of stress deviator and the non-associated flow rule. *International Journal of Plasticity, 27*(2), 217–231.

Hallquist, J. O. (1993). *LS-DYNA Theory Manual*. Troy, MI: Livermore Software Technology Corporation (LSTC).

Hallquist, J.O. (2009). *LS-DYNA Keyword User's Manual, Volumes I and II*. Troy, MI: Livermore Software Technology Corporation (LSTC).

Hammer J.T., "Plastic deformation and ductile fracture of Ti-6Al-4V aluminum under various loading conditions," The Ohio State University, MSc Thesis 2012.

Hencky, H. (1924). Zur Theorie plastischer Deformationen und der hierdurch im Material hervorgerufenen Nachspannungen. *ZAMM Journal of applied mathematics and mechanics: Zeitschrift für angewandte Mathematik und Mechanik*, *4*(4), 323–335.

Hershey, A. V. (1954). The plasticity of an isotropic aggregate of anisotropic face centered cubic crystals. *Journal of Applied Mechanics Trans ASME, 21*, 241–249.

Hill, R. (1950a). On the inhomogeneous deformation of a plastic lamina in a compression test. *The London, Edinburgh, and Dublin Philosophical Magazine and Journal of Science, 41*, 733–744.

Hill, R. (1950b). *The mathematical theory of plasticity*. Oxford, England, UK: Oxford University Press.

Hosford, W. F. (1972). A generalized isotropic yield criterion. *Journal of Applied Mechanics, 39*(2), 607–609.

Hosford, W. F. and Allen, T. J. (1973). Twining and directional slip as a cause for strength differential effect. *Metallurgical Transactions, 4*(5), 1424–1425.

Hosford, W. F. (2005). *Mechanical behavior of materials*. Cambridge, MA: Cambridge University Press.

Huber, M. (1903). Specific work of strain as a measure of material effort. *Towarzystwo Politechniczne, Czas. Techniczne, Lwów*.

Hughes, T. J. R. (1983). Analysis of transient algorithms with particular reference to stability behavior. In Belytschko, T. and Hughes, T. J. R. (Eds.) *Computational methods for transient analysis*. Amsterdam, Netherlands: North-Holland.

Hutchinson, J. W., Jun, S. (1964) Plastic deformation of b.c.c. polycrystals. *Journal of the Mechanics and Physics of Solids, 12*(1), 25–33.

Iyer, S. K., Lissenden, C. J. (2003). Multiaxial constitutive model accounting for the strength-differential in Inconnel 718. *International Journal of Plasticity, 19*(12), 2055–2081.

Johnson, G. R. and Cook, W. H. (1983). *A constitutive model and data for metals subjected to large strains, high strain rates and high temperatures*. In 7th International Symposium on Ballistics, Hague, Netherlands.

Johnson, G. R. and Cook, W. H. (1985). Fracture characteristics of three metals subjected to various strains, strain rates, temperatures and pressures. *Engineering Fracture Mechanics, 21*(1), 31–48.

Karafillis, A. P., Boyce, M. C. (1993). A general anisotropic yield criterion using bounds and a transformation weighting tensor. *Journal of the Mechanics and Physics of Solids, 41*(12), 1859–1886.

Kojic´, M. (2002). Stress integration procedures for inelastic material models within the finite element method. *Applied Mechanics Reviews, 55*(4), 389–414.

Kojic, M., Bathe, K. J. (2005). *Inelastic analysis of solids and structures*. New York, NY: Springer.

Krieg, R. D. and Krieg, D. B. (1977). Accuracies of numerical solution methods for the elastic-perfectly plastic model. *Journal of pressure vessel technology, 99*(4), 510–515.

Kuhn, H., Tucker, A. (1951). *Nonlinear programming.* Proceedings of 2nd Berkeley Symposium. Berkeley: University of California Press. (481–492).

Lode von, W. (1926). Versuche uber den Einfluss der mittleren Hauptspannung auf das Fliessen der Metalle Eisen, Kupfer und Nickell. *Zeitschrift fur Physik, 36*(11–12), 913–939 (In German).

Mendelson, A. (1968). *Plasticity: Theory and Applications*. New York, NY: Springer Publishing.

Mirone, G., Corallo, D. (2010). A local viewpoint for evaluating the influence of stress triaxiality and Lode angle on ductile failure and hardening. *International Journal of Plasticity*, *26*(3), 348–371.

National Transportation Safety Board Report. (1990). Aircraft accident report (NTSB/AAR-90/06).

National Transportation Safety Board Report. (1998). Aircraft accident report (NTSB/AAR-98/01).

Nixon, M. E., Cazacu, O., Lebensohn, R. A. (2010). Anisotropic response of high-purity a-titanium: Experimental characterization and constitutive modeling. International Journal of Plasticity, 26(4), 516–532.

Ortiz, M. and Simo, J.C. (1986). An Analysis of a New Class of Integration Algorithms for Elastoplastic Constitutive Relations. *International Journal for Numerical Methods in Engineering*, *23*(3), 353–366.

"Part 33.94 of Title 14 of the Code of Federal Regulations (14 CFR part 33.94, Blade Containment and Rotor Unbalance Tests)," US Government Printing Office. (2009).

Perzyna, P. (1966). Fundamental problems in viscoplasticity. *Advances in Applied Mechanics, 9,* 243–377.

Raniecki, B., Mro´z, Z. (2008). Yield or martensitic phase transformation conditions and dissipation functions for isotropic, pressure-insensitive alloys exhibiting SD effect. *Acta Metallurgica, 195*(1–4), 81–102.

Rauch, G. C., Leslie, W. C. (1972). The extent and nature of the strength differential effects in steels. *Metallurgical and Materials Transactions B, 3*(2), 377–389.

Rockafellar, R. T. (1972). *Convex Analysis*. Princeton, NJ: Princeton University Press.

Seidt, J. D. (2010). *Plastic deformation and ductile fracture of 2024-t351 aluminum under various loading conditions*. (PhD Thesis). The Ohio State University.

Simo, J. C., Taylor, R. L. (1986). A Return Mapping Algorithm for Plane Stress Elastoplasticity. *International Journal for Numerical Methods in Engineering, 22*(3), 649–670.

Simo, J. C. and Hughes, T. J. R. (1998). *Computational Inelasticity*. New York, NY: Springer-Verlag.

Spitzig, W. A., Sober, R. J., Richmond, O. (1976). The effect of hydrostatic pressure on the deformation behavior of Maraging and HY-80 steels and its implication for plasticity theory. *Metallurgical Transactions, 7*(11), 1703–1710.

Spitzig, R. J., Richmond, O. (1984). The effect of pressure on the flow stress of metals. *Acta Metallurgica, 32*(3), 457–463.

Taylor, G. I. and Quinney, H. (1932). The plastic distortion of metals. *Philosophical Transactions of the Royal Society of London, Series A, 230*, 323–362.

Tresca, H. (1864). On the yield of solids at high pressures. *Comptes Rendus Academie des, Sciences 59*(754). (in French).

Vegter, H., Drent, P., Huetnik, J. (1995). *A planar isotropic yield criterion based on mechanical testing at multi-axial stress states.* Proceedings from NUMIFORM 95 Conference, Ithaca, NY. (pp. 345-350).

von Mises, R. (1913). Mechanik der festen Körper im plastisch deformablen Zustand. *Nachrichten von der Gesellschaft der Wissenschaften zu Göttingen, Mathematisch-Physikalische Klasse, 1*, 582–592.

Wang, L., DuBois, P., Carney, K., Kan, C. D. (2018). *A Temperature and Strain Rate Dependent Material Model with Tension-Compression Asymmetry for 0.25 inch Ti-6Al-4V Plate.* 15th LS-DYNA Users Conference, Dearborn, MI.

Wilkins, M. L. (1964). Calculation of elastic-plastic flow. In Adler, B. et al., (Eds.), *Methods of computational physics, vol. 3* (211–263), New York, NY: Academic Press.

Wilkins, M.L. (1978). Mechanics of penetration and perforation. *International Journal of Engineering Science, 16*(11), 793–807.

Zukas, J.A. (1982). *Impact dynamics*. Hoboken, NJ: John Wiley & Sons.

Zukas, J.A. (1994). Numerical simulation of high rate behavior. In Brebbia, C.A. and Sanchez-Galvez, V., (Eds.), *Shock and Impact on Structures* (1-26). Southampton , UK: Computational Mechanics Publications.

APPENDIX A — SECOND CONVEXITY CONDITION OF THE GYS MODEL

A.1. DERIVATION OF GYS SECOND CONVEXITY CONDITION

The second condition of convexity has been calculated using MATHEMATICA v8 symbolic calculation toolbox. The second condition of convexity is that sum of principal minors of Hessian matrix should be non-negative:

$$M_1 + M_2 + M_3 \geq 0 \tag{A-1}$$

$$M_1 = \frac{\partial^2 f}{\partial \sigma_1^2}\frac{\partial^2 f}{\partial \sigma_2^2} - \left(\frac{\partial^2 f}{\partial \sigma_1 \sigma_2}\right)^2$$

$$M_2 = \frac{\partial^2 f}{\partial \sigma_1^2}\frac{\partial^2 f}{\partial \sigma_3^2} - \left(\frac{\partial^2 f}{\partial \sigma_1 \sigma_3}\right)^2 \tag{A-2}$$

$$M_3 = \frac{\partial^2 f}{\partial \sigma_2^2}\frac{\partial^2 f}{\partial \sigma_3^2} - \left(\frac{\partial^2 f}{\partial \sigma_2 \sigma_3}\right)^2$$

The Generalized Yield Surface (GYS) stress derivatives are as follows for the Hessian matrix:

$$\frac{\partial^2 f}{\partial \sigma_1^2} = \frac{2}{3}\frac{\partial f}{\partial J_2} + \frac{\partial f}{\partial J_3}\frac{2s_1}{3} + \frac{\partial^2 f}{\partial J_2^2}s_1^2 + 2\frac{\partial^2 f}{\partial J_2 J_3}\left(J_3 + \frac{J_2 s_1}{3}\right) + \frac{\partial^2 f}{\partial J_3^2}\left(s_2 s_3 + \frac{J_2}{3}\right)^2 \tag{A-3}$$

$$\frac{\partial^2 f}{\partial \sigma_1^2} = \frac{2}{3}\frac{\partial f}{\partial J_2} + \frac{\partial f}{\partial J_3}\frac{2s_2}{3} + \frac{\partial^2 f}{\partial J_2^2}s_2^2 + 2\frac{\partial^2 f}{\partial J_2 J_3}\left(J_3 + \frac{J_2 s_2}{3}\right) + \frac{\partial^2 f}{\partial J_3^2}\left(s_1 s_3 + \frac{J_2}{3}\right)^2 \tag{A-4}$$

$$\frac{\partial^2 f}{\partial \sigma_1^2} = \frac{2}{3}\frac{\partial f}{\partial J_2} + \frac{\partial f}{\partial J_3}\frac{2s_3}{3} + \frac{\partial^2 f}{\partial J_2^2}s_3^2 + 2\frac{\partial^2 f}{\partial J_2 J_3}\left(J_3 + \frac{J_2 s_3}{3}\right) + \frac{\partial^2 f}{\partial J_3^2}\left(s_1 s_2 + \frac{J_2}{3}\right)^2 \tag{A-5}$$

$$\frac{\partial^2 f}{\partial \sigma_1 \sigma_2} = -\frac{\partial f}{\partial J_2}\frac{1}{3} + \frac{\partial f}{\partial J_3}\frac{2s_3}{3} + \frac{\partial^2 f}{\partial J_2^2}s_1 s_2 + \frac{\partial^2 f}{\partial J_2 J_3}\left(\frac{5J_2 s_3}{3} - s_3^3\right) + \frac{\partial^2 f}{\partial J_3^2}\left(J_3 s_3 + \frac{J_2^2}{9} - \frac{J_2 s_3^2}{3}\right) \tag{A-6}$$

$$\frac{\partial^2 f}{\partial \sigma_1 \sigma_3} = -\frac{\partial f}{\partial J_2}\frac{1}{3} + \frac{\partial f}{\partial J_3}\frac{2s_2}{3} + \frac{\partial^2 f}{\partial J_2^2}s_1 s_3 + \frac{\partial^2 f}{\partial J_2 J_3}\left(\frac{5J_2 s_2}{3} - s_2^3\right) + \frac{\partial^2 f}{\partial J_3^2}\left(J_3 s_2 + \frac{J_2^2}{9} - \frac{J_2 s_2^2}{3}\right) \tag{A-7}$$

$$\frac{\partial^2 f}{\partial \sigma_2 \sigma_3} = -\frac{\partial f}{\partial J_2}\frac{1}{3} + \frac{\partial f}{\partial J_3}\frac{2s_1}{3} + \frac{\partial^2 f}{\partial J_2^2}s_2 s_3 + \frac{\partial^2 f}{\partial J_2 J_3}\left(\frac{5J_2 s_1}{3} - s_1^3\right) + \frac{\partial^2 f}{\partial J_3^2}\left(J_3 s_1 + \frac{J_2^2}{9} - \frac{J_2 s_1^2}{3}\right) \tag{A-8}$$

Helpful relationships for the principal deviatoric stresses s_1, s_2, s_3 in terms of the deviatoric stress invariants J_2 and J_3 are as follows:

$$s_1 + s_2 + s_3 = 0 \tag{A-9}$$

$$s_1 s_2 + s_2 s_3 + s_1 s_3 = -J_2 \tag{A-10}$$

$$s_1^2 + s_2^2 + s_3^2 = 2J_2 \tag{A-11}$$

$$s_1^3 + s_2^3 + s_3^3 = 3J_3 \tag{A-12}$$

$$s_1^4 + s_2^4 + s_3^4 = 2J_2^2 \tag{A-13}$$

$$s_1^5 + s_2^5 + s_3^5 = 5J_3J_2 \tag{A-14}$$

$$s_1^6 + s_2^6 + s_3^6 = 3J_2^2 + 2J_2^3 \tag{A-15}$$

$$s_1^2s_2^2 + s_2^2s_3^2 + s_1^2s_3^2 = J_2^2 \tag{A-16}$$

$$s_1^2s_2 + s_2^2s_1 + s_2^2s_3 + s_3^2s_2 + s_1^2s_3 + s_3^2s_1 = -3J_3 \tag{A-17}$$

$$s_1^2s_2^2(s_1 + s_2) + s_1^2s_3^2(s_1 + s_3) + s_2^2s_3^2(s_2 + s_3) = J_2J_3 \tag{A-18}$$

$$s_1^2s_2^2(s_1^2 + s_2^2) + s_1^2s_3^2(s_1^2 + s_3^2) + s_2^2s_3^2(s_2^2 + s_3^2) = 2J_2^3 - 3J_3^2 \tag{A-19}$$

$$s_1^3(s_2 + s_3) + s_2^3(s_1 + s_3) + s_3^3(s_1 + s_2) = -2J_2^2 \tag{A-20}$$

$$s_1^2(s_2 + s_3) + s_2^2(s_1 + s_3) + s_3^2(s_1 + s_2) = -3J_3 \tag{A-21}$$

Using these equations for the principal deviatoric stresses s_1, s_2, s_3 in terms of the deviatoric stress invariants J_2 and J_3, the following equation is obtained for the sum of minors of Hessian matrix for the GYS model:

$$M_1 + M_2 + M_3 = a^2 + \frac{2}{3}adJ_2^2 + 8aeJ_3 + \frac{4}{3}deJ_2^2J_3 + 12e^2J_3^2 - 3e^2J_3^2 - 2e^2J_2^3 - 4bcJ_3 - 10ceJ_2J_3 - 6cdJ_3^2 - \frac{10}{3}deJ_2^2J_3 + \frac{20}{3}e^2J_2^3 + 4deJ_2^2J_3 - \frac{2}{9}d^2J_2^4 + \frac{8}{3}beJ_2^2 + \frac{2}{3}deJ_2^2J_3 + \frac{2}{3}bdJ_2J_3 + 2cdJ_2^3 - 3cdJ_3^2 + 4deJ_2^2J_3 + \frac{2}{9}d^2J_2^4 - \frac{4}{3}cdJ_2^3 - \frac{4}{3}deJ_2^2J_3 - 2bcJ_3 - 2ceJ_2J_3 + 4deJ_2^2J_3 + \frac{4}{3}adJ_2^2 - 2aeJ_3 + \frac{8}{3}acJ_2 + 8ceJ_2J_3 - \frac{8}{9}adJ_2^2 - \frac{40}{9}beJ_2^2 - \frac{2}{3}acJ_2 - \frac{4}{9}adJ_2^2 + \frac{4}{9}cdJ_2^3 + \frac{2}{9}cdJ_2^3 - \frac{50}{9}e^2J_2^3 + \frac{4}{27}d^2J_2^4 - \frac{20}{3}deJ_2^2J_3 - \frac{8}{3}bdJ_2J_3 - \frac{4}{27}d^2J_2^4 - \frac{8}{3}deJ_2^2J_3 - \frac{4}{9}b^2J_2 - \frac{8}{9}beJ_2^2 - \frac{4}{9}e^2J_2^3 - \frac{8}{9}b^2J_2 + 4ceJ_2J_3 \tag{A-22}$$

Invariant derivatives of the GYS model a, b, c, d, e are given as follows:

$$f = \sqrt{3}c_1J_2^{1/2} + c_2\frac{9J_3}{2J_2} + c_3\frac{27\sqrt{3}J_3^2}{4J_2^{5/2}} - \sigma_y \tag{A-23}$$

$$a = \frac{\partial f}{\partial J_2} = c_1\frac{\sqrt{3}}{2J_2^{1/2}} - c_2\frac{9J_3}{2J_2^2} - c_3\frac{5}{2}\frac{27\sqrt{3}J_3^2}{4J_2^{7/2}} \tag{A-24}$$

$$b = \frac{\partial f}{\partial J_3} = c_2\frac{9}{2J_2} + c_3\frac{27\sqrt{3}J_3}{2J_2^{5/2}} \tag{A-25}$$

$$c = \frac{\partial^2 f}{\partial J_2^2} = -c_1\frac{\sqrt{3}}{4J_2^{3/2}} + c_2\frac{9J_3}{J_2^3} + c_335\frac{27\sqrt{3}J_3^2}{16J_2^{9/2}} \tag{A-26}$$

$$d = \frac{\partial^2 f}{\partial J_3^2} = c_3\frac{27\sqrt{3}}{2J_2^{5/2}} \tag{A-27}$$

$$e = \frac{\partial^2 f}{\partial J_2 J_3} = -c_1 \frac{9}{2J_2^2} - c_3 \frac{5}{2} \frac{27\sqrt{3}J_3}{2J_2^{7/2}} \tag{A-28}$$

$$M_1 + M_2 + M_3 = 0 \tag{A-29}$$

$$M_1 + M_2 + M_3 \geq 0 \; always \; satisfied \tag{A-30}$$

A.2 CONVEXITY CONDITIONS OF THE CAZACU-BARLAT, VON MISES, AND DRUCKER MODELS

The equations describing the Cazacu-Barlat, von Mises, and Drucker models are given as follows:

A.2.1. Cazacu-Barlat Convexity Condition

$$f = J_2^{3/2} - cJ_3 \tag{A-31}$$

$$\frac{\partial f}{\partial J_2} = \frac{3}{2} J_2^{1/2}, \frac{\partial f}{\partial J_3} = -c\,, \frac{\partial^2 f}{\partial J_3^2} = 0, \frac{\partial^2 f}{\partial J_2^2} = \frac{3}{4} J_2^{-1/2}, \frac{\partial^2 f}{\partial J_2 J_3} = 0 \tag{A-32}$$

First Condition:

$$trace(\boldsymbol{H}) = \frac{\partial^2 f}{\partial \sigma_1^2} + \frac{\partial^2 f}{\partial \sigma_2^2} + \frac{\partial^2 f}{\partial \sigma_3^2} \geq 0 \tag{A-33}$$

$$\frac{\partial^2 f}{\partial \sigma_1^2} = \frac{3}{4} J_2^{-1/2} s_1^2 + J_2^{1/2} - c\frac{2s_1}{3} \tag{A-34}$$

$$\frac{\partial^2 f}{\partial \sigma_2^2} = \frac{3}{4} J_2^{-1/2} s_2^2 + J_2^{1/2} - c\frac{2s_2}{3} \tag{A-35}$$

$$\frac{\partial^2 f}{\partial \sigma_3^2} = \frac{3}{4} J_2^{-1/2} s_3^2 + J_2^{1/2} - c\frac{2s_3}{3} \tag{A-36}$$

$$trace(\boldsymbol{H}) = 3J_2^{1/2} + \frac{3}{4} J_2^{-1/2} 2J_2 = \frac{9}{2} J_2^{1/2} \geq 0 \; always \; satisfied \tag{A-37}$$

Second Condition:

$$M_1 + M_2 + M_3 \geq 0 \tag{A-38}$$

$$-\frac{4}{3}c^2 - \sqrt{3}(cos3\theta)c + \frac{9}{2} \geq 0 \; (-1 \leq cos3\theta \leq +1) \tag{A-39}$$

$$-\frac{3\sqrt{3}}{4} \leq c \leq +\frac{3\sqrt{3}}{4} \tag{A-40}$$

A.2.2. von Mises yield function

$$f = \sqrt{3} J_2^{1/2} \tag{A-41}$$

$$\frac{\partial f}{\partial J_2} = \frac{\sqrt{3}}{2} J_2^{-1/2}, \frac{\partial f}{\partial J_3} = \frac{\partial^2 f}{\partial J_3^2} = \frac{\partial^2 f}{\partial J_2 J_3} = 0, \frac{\partial^2 f}{\partial J_2^2} = -\frac{\sqrt{3}}{4} J_2^{-3/2} \quad \text{(A-42)}$$

First Condition:

$$trace(\boldsymbol{H}) = \frac{\partial^2 f}{\partial \sigma_1^2} + \frac{\partial^2 f}{\partial \sigma_2^2} + \frac{\partial^2 f}{\partial \sigma_3^2} \geq 0 \quad \text{(A-43)}$$

$$\frac{\partial^2 f}{\partial \sigma_1^2} = \frac{\sqrt{3}}{3} J_2^{-1/2} - \frac{\sqrt{3}}{4} J_2^{-3/2} s_1^2 \quad \text{(A-44)}$$

$$\frac{\partial^2 f}{\partial \sigma_2^2} = \frac{\sqrt{3}}{3} J_2^{-1/2} - \frac{\sqrt{3}}{4} J_2^{-3/2} s_2^2 \quad \text{(A-45)}$$

$$\frac{\partial^2 f}{\partial \sigma_3^2} = \frac{\sqrt{3}}{3} J_2^{-1/2} - \frac{\sqrt{3}}{4} J_2^{-3/2} s_3^2 \quad \text{(A-46)}$$

$trace(\boldsymbol{H}) = \sqrt{3} J_2^{-1/2} - \frac{\sqrt{3}}{4} J_2^{-3/2} (s_1^2 + s_2^2 + s_3^2) = \sqrt{3} J_2^{-1/2} - \frac{\sqrt{3}}{2} J_2^{-1/2} = \frac{\sqrt{3}}{2} J_2^{-1/2} \geq 0$ $always\ satisfied$ $(s_1^2 + s_2^2 + s_3^2 = 2J_2)$ (A-47)

Second Condition:

$$M_1 + M_2 + M_3 = 0 \quad \text{(A-48)}$$

$$then\ M_1 + M_2 + M_3 \geq 0\ always\ satisfied \quad \text{(A-49)}$$

A.2.3. Drucker yield function

$$f = J_2^3 - cJ_3^2 \quad \text{(A-50)}$$

$$\frac{\partial f}{\partial J_2} = 3J_2^2, \frac{\partial f}{\partial J_3} = -2cJ_3, \frac{\partial^2 f}{\partial J_3^2} = -2c, \frac{\partial^2 f}{\partial J_2 J_3} = 0, \frac{\partial^2 f}{\partial J_2^2} = 6J_2 \quad \text{(A-51)}$$

First Condition:

$trace(\boldsymbol{H}) = \frac{\partial^2 f}{\partial \sigma_1^2} + \frac{\partial^2 f}{\partial \sigma_2^2} + \frac{\partial^2 f}{\partial \sigma_3^2} = 2\frac{\partial f}{\partial J_2} + \frac{\partial^2 f}{\partial J_2^2} 2J_2 + \frac{\partial^2 f}{\partial J_3^2}\left(\left(\frac{\partial J_3}{\partial \sigma_1}\right)^2 + \left(\frac{\partial J_3}{\partial \sigma_2}\right)^2 + \left(\frac{\partial J_3}{\partial \sigma_3}\right)^2\right) = 18J_2^2 - 2c\left(\frac{2J_2^2}{3}\right)$ (A-52)

$$trace(\boldsymbol{H}) = J_2^2\left(18 - \frac{4c}{3}\right) \geq 0 \Rightarrow \frac{27}{2} \geq c\ (J_2^2\ is\ always\ positive) \quad \text{(A-53)}$$

Note that the second condition satisfies the first condition; therefore, the second condition is the convexity condition for the Drucker model.

Second Condition:

$$M_1 + M_2 + M_3 \geq 0 \quad \text{(A-54)}$$

$$45 - 20c + 180c\left(\frac{12}{81}(cos3\theta)^2\right) - \frac{40}{3}c^2\left(\frac{12}{81}(cos3\theta)^2\right) \geq 0$$

$$(0 \leq (cos3\theta)^2 \leq 1) \qquad \text{(A-55)}$$

$$\frac{-27}{8} \leq c \leq \frac{9}{4}$$

APPENDIX B — DERIVATIVE OF GYS YIELD FUNCTION WITH RESPECT TO THE INCREMENT OF THE PLASTIC STRAIN MULTIPLIER

The derivative of the yield function with respect to the increment of the plastic multiplier ($\Delta\lambda$) is an important property in terms of finding a correct root in the solution interval. The following equations prove that derivative is negative. This result shows that the function $f(\Delta\lambda)$ is monotonically decreasing in the solution interval. Therefore, only one positive root exists for the solution of $f(\Delta\lambda) = 0$:

$$f(\sigma_{eff}, \sigma_y) = \sigma_{eff}(\boldsymbol{\sigma}) - \sigma_y \tag{B-1}$$

$$\frac{df}{d(\Delta\lambda)} = f' = \frac{\partial\sigma_{eff}}{\partial\boldsymbol{\sigma}}\frac{\partial\boldsymbol{\sigma}}{\partial(\Delta\lambda)} - \frac{\partial\sigma_y}{\partial(\Delta\lambda)} \tag{B-2}$$

$$\boldsymbol{\sigma} = \boldsymbol{\sigma}^{trial} - 2G\Delta\lambda\frac{\partial f}{\partial\boldsymbol{\sigma}} \tag{B-3}$$

$$\frac{\partial f}{\partial\boldsymbol{\sigma}} = \frac{\partial\sigma_{eff}}{\partial\boldsymbol{\sigma}} \tag{B-4}$$

$$\frac{df}{d(\Delta\lambda)} = f' = -\frac{\partial f}{\partial\boldsymbol{\sigma}} : 2G\frac{\partial f}{\partial\boldsymbol{\sigma}} - \frac{\partial\sigma_y}{\partial(\Delta\lambda)} \; and \; \frac{\partial f}{\partial\boldsymbol{\sigma}} : \frac{\partial f}{\partial\boldsymbol{\sigma}} = \left\|\frac{\partial f}{\partial\boldsymbol{\sigma}}\right\|^2 \tag{B-5}$$

$$\frac{df}{d(\Delta\lambda)} = f' = -\left(2G\left\|\frac{\partial f}{\partial\boldsymbol{\sigma}}\right\|^2 + \frac{\partial\sigma_y}{\partial(\Delta\lambda)}\right) \tag{B-6}$$

Consider that $\frac{\partial\sigma_y}{\partial(\Delta\lambda)}$ term is always positive for the strain-hardening material. Therefore, the derivative of the yield function with respect to the increment of the plastic multiplier is always negative. This validates that the nonlinear scalar function $f(\Delta\lambda)$ is a monotonically decreasing function for the positive values of $\Delta\lambda$.